CONF-9605167--
ORNL/FMP-96/1

U.S. Department of Energy
Fossil Energy
Advanced Research and Technology Development

Proceedings of the Tenth Annual Conference On Fossil Energy Materials

May 14-16, 1996
Knoxville, Tennessee

Fossil Energy AR&TD Materials Program

OAK RIDGE NATIONAL LABORATORY
MANAGED BY
LOCKHEED MARTIN ENERGY RESEARCH CORP.
FOR THE
U.S. DEPARTMENT OF ENERGY
UNDER CONTRACT DE-AC05-96OR22464

Fossil Energy Program

CONF-9605167
ORNL/FMP-96/1

PROCEEDINGS OF THE TENTH ANNUAL CONFERENCE ON FOSSIL ENERGY MATERIALS

May 14-16, 1996
Knoxville, Tennessee

Compiled by
N. C. Cole and R. R. Judkins

Date Published: August 1996

Prepared by the
Department of Energy
Fossil Energy Office of Advanced Research
and
Oak Ridge Operations Office
AA 15 10 10 0

Prepared by the
OAK RIDGE NATIONAL LABORATORY
Oak Ridge, Tennessee 37831-6285
managed by
LOCKHEED MARTIN ENERGY RESEARCH CORP.
for the
U. S. DEPARTMENT OF ENERGY
under Contract DE-AC05-96OR22464

PREFACE

The Tenth Annual Conference on Fossil Energy Materials was held in Knoxville, Tennessee, on May 14-16, 1996. The meeting was sponsored by the U.S. Department of Energy's (DOE) Office of Fossil Energy through the Advanced Research and Technology Development (AR&TD) Materials Program. The objective of the AR&TD Materials Program is to conduct research and development on materials for longer-term fossil energy applications as well as for generic needs of various fossil fuel technologies. The management of the program has been decentralized to the DOE Oak Ridge Operations Office and Oak Ridge National Laboratory (ORNL). The research is performed by staff members at ORNL and by researchers at other national laboratories, universities, and in private industry. The work is divided into the following categories: (1) structural ceramics, (2) new alloys and coatings, (3) functional materials, and (4) technology development and transfer.

This conference is held each year to review the work on all of the projects of the program. The final program for the meeting is given in Appendix A, and a list of attendees is presented in Appendix B.

These proceedings have been published from camera-ready masters supplied by the authors. All of the contributions have been checked for errors but have not been subjected to peer reviews. However, most of the papers have already undergone technical review within the individual organizations before submission to the Program Office.

The successful completion of the conference and publication of the proceedings has required help from several people. The organizers with to thank Judy Fair for her superb coordination work; Connie Tilley for her assistance with preparations for the conference; Gloria Donaldson and Judy for their excellent work at the registration desk; Thelma Bonfoey for her help in the many arrangements; and the numerous staff and support personnel associated with the conference. Finally, we express our sincere appreciation to the authors whose efforts are the very basis of the conference.

TABLE OF CONTENTS

SESSION II - CERAMICS, NEW ALLOYS, AND FUNCTIONAL MATERIALS

SESSION I

CERAMIC COMPOSITES AND FUNCTIONAL MATERIALS

FABRICATION OF FIBER-REINFORCED COMPOSITES BY CHEMICAL VAPOR INFILTRATION

T.M. Besmann,* W.M. Matlin**, D.P. Stinton,*and P. K. Liaw**

*Oak Ridge National Laboratory, Oak Ridge, TN 37831

**Department of Materials Science and Engineering, University of Tennessee
Knoxville, TN 37996-2200

ABSTRACT

Processing equipment for the infiltration of fiber-reinforced composite tubes is being designed that incorporates improvements over the equipment used to infiltrate disks. A computer-controlled machine-man interface is being developed to allow for total control of all processing variables. Additionally, several improvements are being made to the furnace that will reduce the complexity and cost of the process. These improvements include the incorporation of free standing preforms, cast mandrels, and simpler graphite heating elements.

INTRODUCTION

Fiber-reinforced silicon carbide matrix composites are a candidate for a number of high temperature applications due to their high temperature strength, light weight, thermal shock resistance and damage tolerance. However, in the current commercial isothermal, isobaric chemical vapor infiltration process, thick parts are difficult to density. A leading alternative process is forced chemical vapor infiltration (FCVI). In FCVI, a preform is placed in a reactor, where one side is heated and the other side is cooled, resulting in a thermal gradient across the preform. As the reactant gases pass through the preform they undergo a surface reaction, resulting in the formation of a ceramic matrix and an effluent gas. In the case of SiC deposited from chlorosilanes, the effluent gas has a poisoning effect on the reaction rate. This poisoning,

combined with the depletion of the reactant, tends to slow down the deposition rate. However, since the gases are traveling toward the hot side of the preform their temperature increases, resulting in faster deposition rates due to the Arrhenius behavior of the deposition reaction. Control over deposition can thus be maintained by using the increase in temperature to offset reactant depletion and effluent gas buildup.

Work at the Oak Ridge National Laboratory (ORNL) has shown that the time to infiltrate 4.45 cm diameter disks 1.27 cm thick can be reduced from 24 hours to less than 15 hours by utilization of a two-step process [1]. This reduction in processing time is expected to result in lower processing cost, thereby making the process more industrially feasible [2]. Additionally, ORNL researchers have investigated the production of more industrially relevant shapes such as tubes. Initially, 2.54 cm diameter tubes were made using furnaces originally designed for the production of disks [3]. Based on the initial successes of the 2.54-cm inner diameter, 0.64-cm wall thickness tubes, a larger furnace was designed exclusively for the fabrication of tubes (Fig. 1). This furnace is designed to process tubes up to 10 cm in diameter and 30 cm in length. The new furnace, as well, will incorporate a number of improvements based on the experience of processing numerous disks and a few initial tubes.

PROCESS OPTIMIZATION THROUGH THE CONTINUAL CONTROL OF PROCESSING VARIABLES

As demonstrated in the two-step FCVI process, significant time savings can be achieved through the proper control of thermal gradient, reactant concentration, total gas flow, and

pressure. The two-step process does not represent the end of process optimization, but an initial step. In the ideal case, processing conditions would be varied continuously in response to the continually changing pore structure within the preform. A LabView™-based process control system is being designed that will allow for the complete control of reactant and carrier gas flow rates as well as preform hot-side temperature. Each of these variables can be controlled as a function of time, thereby allowing the investigation of more complex process optimization schemes. Figure 2 is a schematic of the FCVI system and controls.

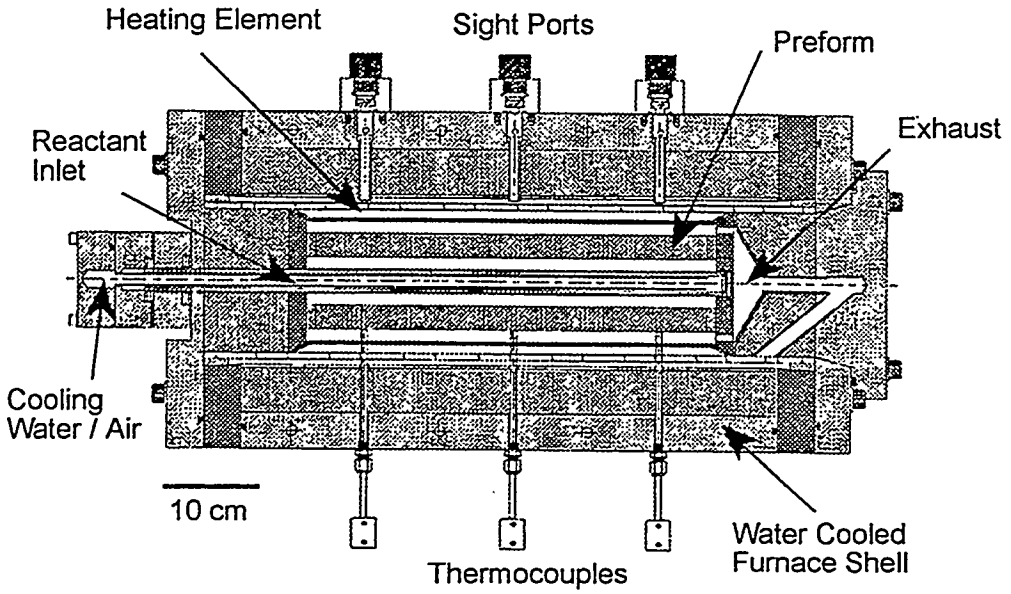

Figure 1. Scale-up furnace for the fabrication of tubular composites.

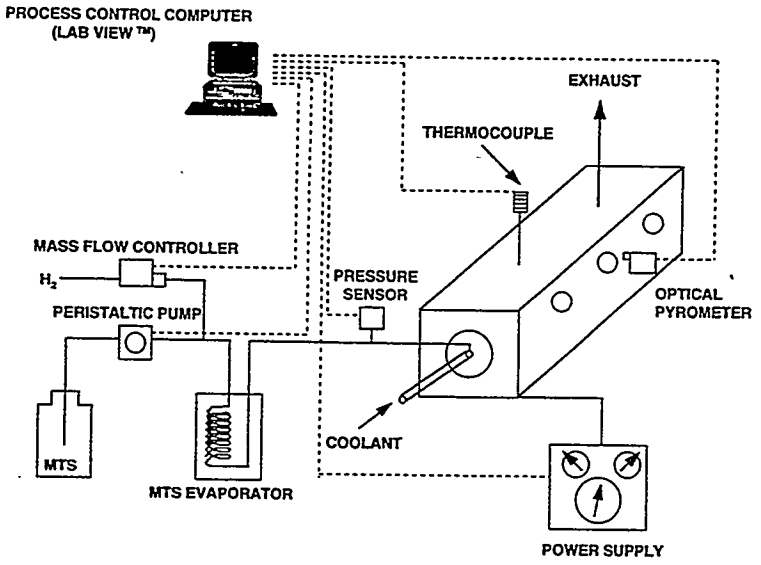

Figure 2. Flow diagram and controls for the scale-up FCVI system for preparing tubular composites.

At the heart of the system is a Power Macintosh 7100/80 containing a four port serial card and a Lab - NB data acquisition card running LabView 3.1.1. Carrier gas flow is controlled through the use of a serial connection between the LabView computer and mass flow controllers. Liquid methyltrichlorosilane (CH_3SiCl_3 or MTS), at room temperature and pressure is pumped from a storage container to a vaporizer using a peristaltic pump. In a manner similar to the control of the carrier gas, LabView is used to send a set point to the peristaltic pump thereby controlling the flow of reactant into the system. As an additional method of control the MTS container is placed on a electronic balance with a serial port. In this way an accurate measurement of reactant flow can be maintained by continually monitoring the reduction in container weight using LabView.

The final area of control is preform temperature. The system has two methods for

controlling preform temperature. The first method is through the use of an Ircon Modline Plus optical pyrometer. Additional monitoring of preform temperature can be accomplished through a thermocouple which can be placed on the cool side of the preform to monitor the thermal gradient..

IMPROVEMENTS IN THE TUBE FURNACE DESIGN

The transition from processing relatively simple shape preforms such as disks to more complicated shapes such as tubes requires alternate design furnace internals. In order to effectively infiltrate composites using FCVI, four criteria must be met; a pressure differential must be established across the preform, a thermal gradient must be established across the preform, reactant and carrier gases must be introduced to the high pressure, cool-side of the preform, and effluent gases must be removed from the low pressure hot side of the preform.

The pressure differential in the disk furnace is achieved by allowing a water-cooled injector to be pressed against the bottom of the preform holder. A graphite foil gasket is placed between the holder and the injector to ensure a relatively gas-tight seal. The holder is held in place by ridges inside the coating chamber. In addition to positioning the preform within the furnace, the coating chamber also serves to protect the heating element, which resides outside the coating chamber, from overcoating by SiC. A preform hot side temperature can be measured and controlled by sighting an optical pyrometer down the inside of the coating chamber and focusing on the top of the preform. Once the correct preform hot-side temperature is established the correct thermal gradient can be fixed by varying the materials and distance between the

preform and the water-cooled injector. The further away from the injector and the lower the thermal conductivity of the spacer material the higher the cool-side temperature. Finally, the reactant gases are directed to the cool-side of the preform by flowing them through the inside of the water-cooled injector.

Since this furnace design served the production of disks so well it was adapted for the production of tubes. However, the first tube infiltration revealed a number of areas which required improvement. In the production of disks the graphite holder became bonded by deposited SiC to the preform during the FCVI process. At completion, the holder must be machined from the part. While this works well in the case of disks where the preform is surrounded by the holder, it does not work as easily with tubes since the mandrel is surrounded by the preform. It is also difficult to form a gas-tight seal between the mandrel and the cooled injector. Without such a seal a pressure differential can not be imposed across the preform. Lack of a tight seal has two negative results. It becomes impossible to achieve high final preform densities and there is a large loss of reactant through deposition on the inner walls of the furnace and through exhaust from the furnace.

As a solution to these difficulties, methods of removing the graphite mandrel were investigated. Initially, the use of more easily machinable mandrel material, such as carbon bonded carbon fiber were investigated. However, it was recognized that the ideal situation would being able to process the preform without the use of a mandrel. With the assistance , of researchers at the 3M Company's Research and Development Center, a process for rigidizing tubular preforms was adapted for the current system. While originally developed as a method to

rigidize thin, hot gas filter preforms, the method works equally well for thicker preforms. In the 3M process, the preform is immersed in a dilute phenolic resin solution. The impregnated tube is then removed from the solution, dried, and cured, resulting in a rigid preform. When fired to FCVI process temperatures, 800°C - 1200°C, the phenolic resin pyrolyzes, leaving a thin carbon layer. It is speculated that this carbon layer bonds the individual fibers together where the fibers contact each other, thereby explaining the limited strength of the after fired tubes.

Without the use of a mandrel, another approach to forming of a gas tight seal is needed. Casting the preform to the cooled injector was attempted since it was simple, inexpensive, and likely effective. In this method a high-alumina castable refractory was used to fix the preform directly to the injector, thereby positioning the preform a specific distance from the injector and creating a gas tight seal. Tailoring the thermal gradient can still be achieved by positioning an insulating sleeve of material between the injector and the preform.

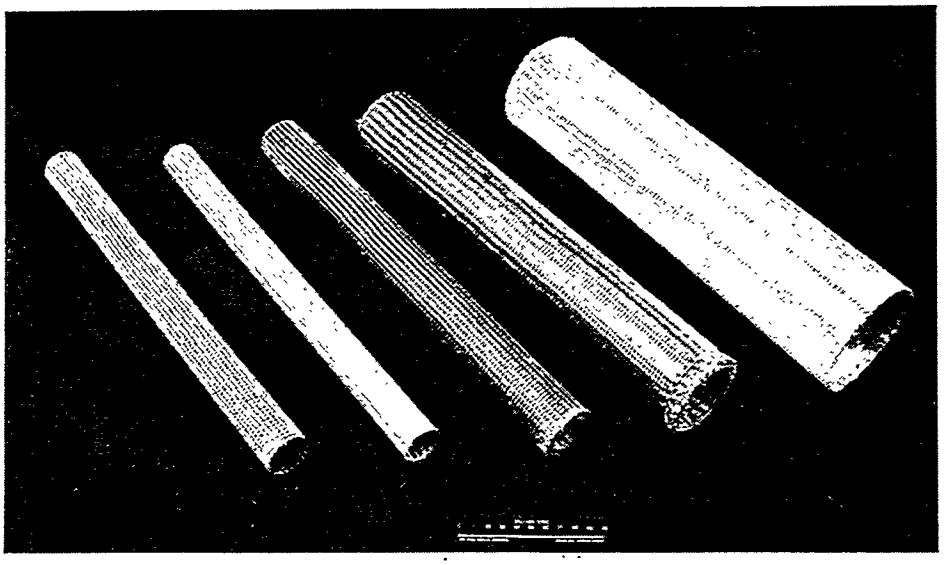

Figure 3. Various Nextel™ fiber tubes rigidized with phenolic resin.

Rather than supplying reactant to the cool-side of the preform by running the gases inside the injector, as is done in the smaller units for preparing disks, penetrations through the cast end caps were used to allow the reactant gases to be routed to the inside of the preform. This method greatly simplifies the injector design and eliminates any welds from being exposed to the highly corrosive environment within the furnace.

Finally, one of the most critical process parameters in FCVI is the thermal gradient, and therefore the cool- and hot-side temperatures. Hot-side temperatures are relatively easily controlled via power to the furnace. Cool-side temperature control is more problematic. Current efforts to improve control of the cool-side temperature in the scale-up tube furnace involve variability in the injector coolant. The injector system has been designed to allow for water, high-temperature oil (silicone), or air cooling. Previous experience in the smaller tube fabrication systems has indicated that maintaining a sufficiently high inner diameter temperature is difficult. It is thus expected that alternate cooling media will allow greater control over the thermal gradient and allow higher inner diameter temperatures to be used.

REFERENCES

[1] W.M. Matlin, D.P. Stinton, and T.M. Besmann, "Fabrication of Fiber-Reinforced Composites by Chemical Vapor Infiltration", Proceedings of the Ninth Annual Conference on Fossil Energy Materials, Oak Ridge National Laboratory Report ORNL/FMP-95/1, pp 157-165, (1995)

[2] Y.G. Roman, D.P. Stinton, "The Preparation and Economics of Silicon Carbide Matrix Composites by Chemical Vapor Infiltration"; in Mat. Res. Soc. Symp. Proc. Vol. 365 Edited by R.A. Lowden, M.K. Ferber, J.R. Hellman, K.K. Chawla, S.G. DiPietro, Materials Research Society, Pittsburg, PA, pp. 343-350 (1994)

[3] D.P. Stinton, T.M. Besmann, W.M. Matlin, T.L. Starr, and W.A. Curtin, "Forced Chemical Vapor Infiltration of Tublar Geometries: Modeling, Design, and Scale-Up"; in Mat. Res. Soc. Symp. Proc. Vol. 365 Edited by R.A. Lowden, M.K. Ferber, J.R. Hellman, K.K. Chawla, S.G. DiPietro, Materials Research Society, Pittsburg, PA, pp. 317-324 (1994)

TRANSPORT PROPERTIES OF CERAMIC COMPOSITES

T.L. Starr and N. Hablutzel

School of Materials Science and Engineering
Georgia Institute of Technology
Atlanta, Georgia 30332-0245

Instrumentation and procedures have been completed for measurement of gas permeability and mass diffusivity of fiber preforms and porous materials. Results are reported for composites reinforced with Nicalon fiber in cloth lay-up and 3-D weave and with Nextel fiber in multi-layer braid. Measured permeability values range from near 100 to less than 0.1 darcies. Mass diffusivity is reported as a structure factor relating the diffusion through the porous material to that in free space. This measure is independent of the diffusing species and depends only the pore structure of the material.

Measurements are compared to predictions of a node-bond model for gas transport. Model parameters adjusted to match measured transport properties relate to physical microstructure features of the different architectures. Combination of this transport model with the CVI process model offers a predictive method to evaluate the densification behavior of various fiber preforms.

INTRODUCTION

The success of chemical vapor infiltration (CVI) for ceramic matrix composites is strongly controlled by the mass transport properties of the preform and of the partially densified composite. These properties include gas permeability and mass diffusivity (effective diffusion coefficient), and depend on the density and microstructure of the composite. While gas permeability is the critical factor for forced flow CVI, mass diffusivity is a controlling property for isothermal CVI and may be important for coating or finishing processes designed to produce oxidation resistance or gas tightness in ceramic composite components. This effort involves experimental measurement of transport properties and model development for prediction of these properties and of densification performance.

MASS TRANSPORT MEASUREMENTS

The apparatus for measurement of gas permeability and mass diffusivity is shown schematically in Figure 1 and photographically in Figure 2. A specimen of preform or porous composite, mounted in an aluminum ring, is held in the specimen chamber with o-ring seals top and bottom. The two sides of a differential pressure (DP) gauge (MKS Instruments) are connected to the volumes above and below the specimen. Helium gas flows through a mass flowmeter (MKS Instruments) into the chamber below the specimen. The apparatus includes two different DP gauges (0-10 and 0-200 torr) and two different flow meters (0-20 and 0-200 sccm) to allow accurate measurements over a wide range of permeabilities. The 4-port valve v7 can be switched to connect together the two ends of the DP gauge to allow checking of the gauge zero point reading.

For permeability measurements, only valves v1-v3 are open. The helium gas flow rate is adjusted using the needle valve v1 and the differential pressure across the specimen is recorded for each flow level. The gas permeability is calculated from a linear fit to the flow vs. pressure data, the specimen dimensions and the viscosity of helium. A typical plot of measured data and the resulting fit is shown in Figure 3. The estimated standard error for these measurements, based on the goodness-of-fit, is often as low as 1-2% of the permeability value.

For mass diffusivity, valves v4-v6 are opened producing flow of a helium-10% methane mixture across the top face of the specimen and of pure helium across the bottom face. Any methane passing through the specimen is measured using the gas chromatography, thermal conductivity-type detector TC. Over a small range near zero differential pressure the concentration of methane through the detector depends on both convection and diffusion, proportional to the expression,

$$U\left(1+\frac{1}{\exp(P_e)-1}\right)$$

where U is the linear velocity of the gas through the specimen which is calculated from the known gas permeability and the pressure difference, P_e is the Peclet number UL/D, L is the

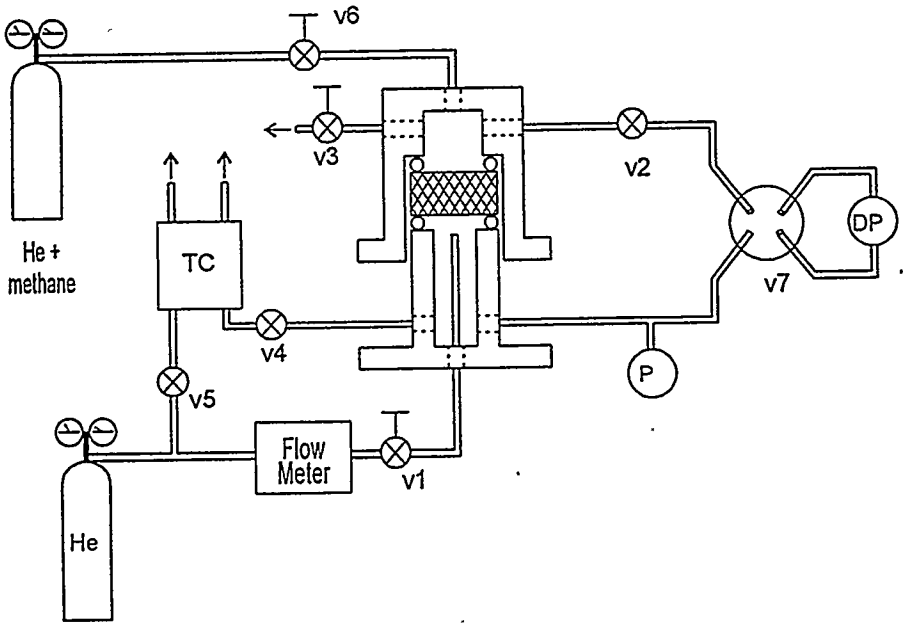

Figure 1. Apparatus for measuring gas permeability and mass diffusivity.

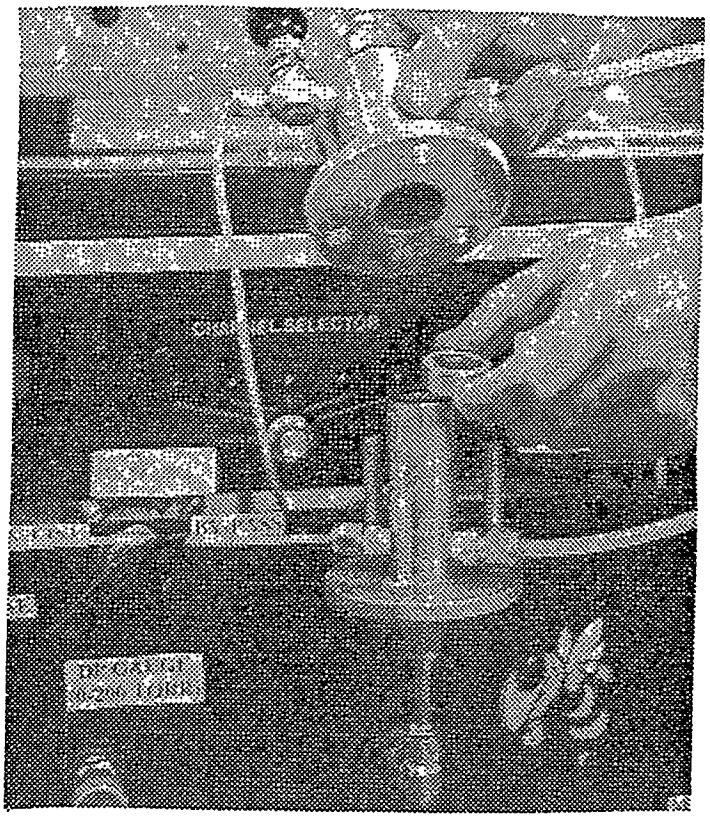

Figure 2. Permeability specimen is mounted in aluminum ring and placed in chamber.

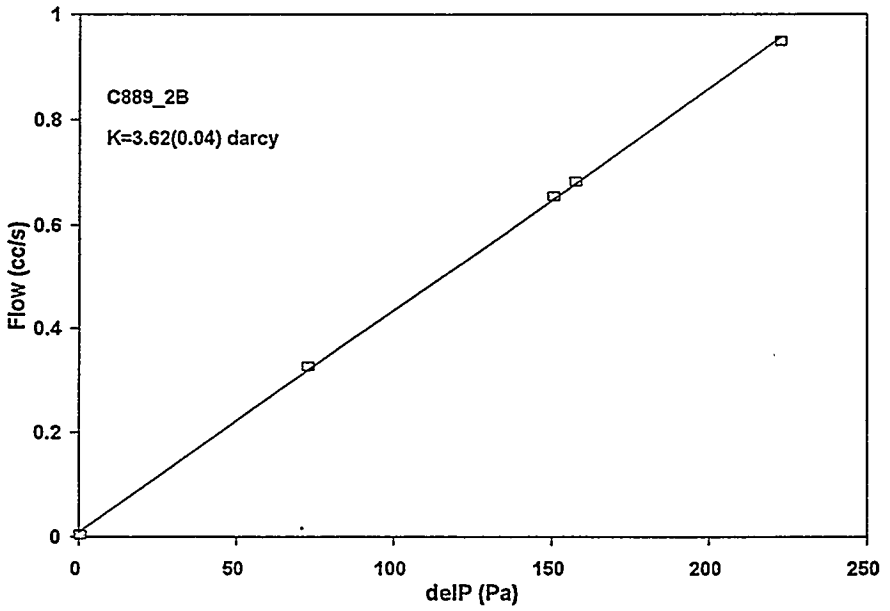

Figure 3. Gas permeability is calculated from linear fit to measured flow versus differential pressure.

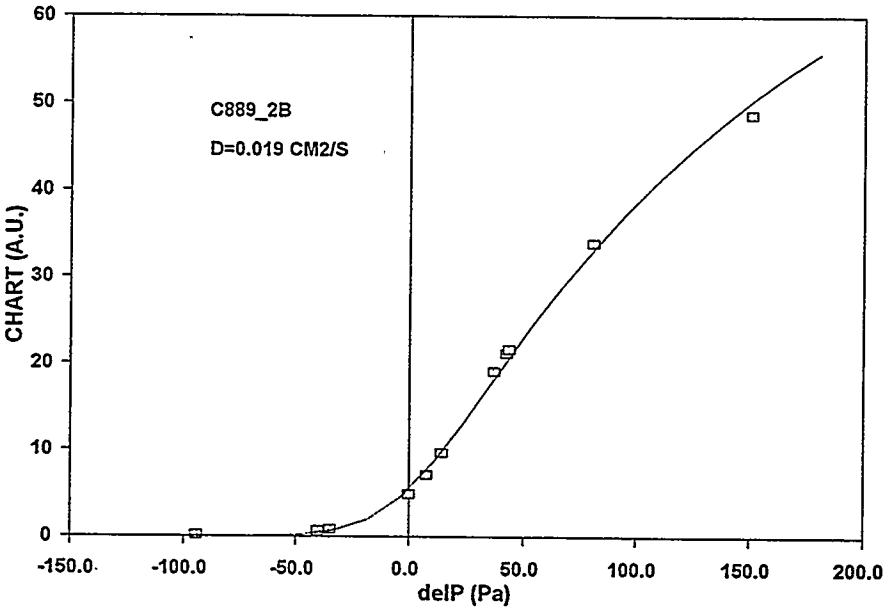

Figure 4. Mass diffusivity is calculated from fit to measured methane concentration versus pressure differential across specimen.

thickness of the specimen and D is the mass diffusivity (cm^2/s). Fitting this curve to the measured data gives the mass diffusivity (Figure 4). This value is converted to a dimensionless diffusion factor by dividing by the handbook value of the free space diffusion coefficient for methane in helium[1], 0.748 cm^2/s. This diffusion factor relates to the amount and tortuosity of the open porosity in the specimen. Recent measurements include Nicalon fiber cloth layup and 3-D weave, and Nextel fiber braid. Values of gas permeability and diffusion factor for these materials are given in Table 1.

Table 1. Measurements of permeability and mass diffusivity.

specimen		density		permeability	diffusion
ID	description	(g/cm^3)	(fraction)	(darcy)	factor
Ni30-1	Nicalon 0/30/60 layup	1.02	0.40	12.0	.047
Ni45-1	Nicalon 0/45 layup	1.02	0.40	9.1	.031
Ni90-1	Nicalon 0/90 layup	1.02	0.40	11.7	.047
Ni90-3	Nicalon 0/90 layup	1.02	0.40	8.2	.044
C885-1	CVI Nic 0/30/60	1.89	0.65	1.86	.0026
C885-2	CVI Nic 0/30/60	1.93	0.67	1.30	.0053
C885-3	CVI Nic 0/30/60	1.89	0.65	1.70	.0026
C889-2	CVI Nic 0/30/60	2.09	0.72	3.54	.024
C227a	CVI Nic 0/30/60	1.96	0.68	2.66	.002
C227c	CVI Nic 0/30/60	2.45	0.85	3.19	nd
C559g	CVI Nic 3-D weave	2.04	0.70	0.50	.0094
C559-1	CVI Nic 3-D weave	2.29	0.79	(0)	(0)
C559-3	CVI Nic 3-D weave	2.23	0.77	(0)	(0)
Nex-1	Nextel braid	0.99	0.37	25.3	.056
Nex-2	Nextel braid	0.89	0.33	19.0	.063

1 darcy = 10^{-8} cm^2 ; nd= not determined; (0) = no flow detected through specimen

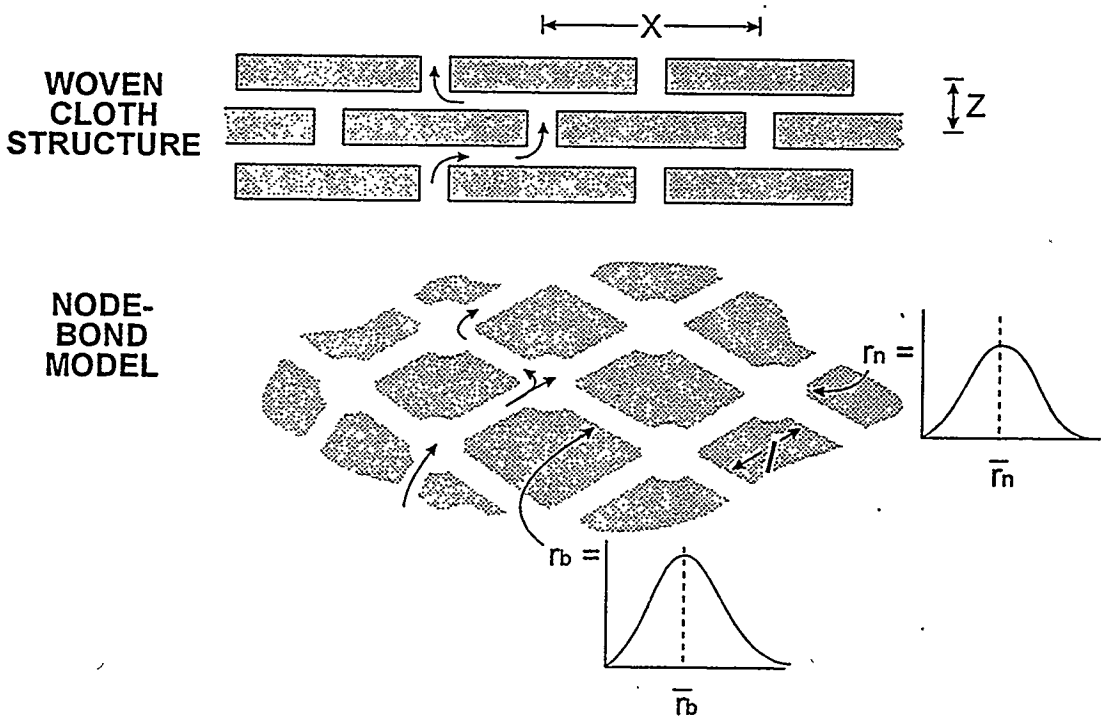

Figure 5. Node-bond model approximates structure of woven fiber preform.

MODELING OF MICROSTRUCTURE AND MASS TRANSPORT

In order to better understand the relationship between transport properties and fiber architecture we have developed a node-bond model[2]. Woven and braided fiber structures are constructed using tows or yarns of 500-5000 individual filaments. While the fine porosity between filaments in the tows constitutes approximately half of the total porosity, it is the coarser porosity between tows that carries the gas flow through the composite. We model this structure as a network of nodes and bonds as shown in Figure 5. The average dimensions of the nodes and bonds, and their variability are determined by the weave structure. These dimensions are used to calculate permeability and diffusivity of the network. During CVI the pores fill in a progressive manner with increasing deposit thickness. When a particular fraction of the bonds are closed - the percolation limit - mass transport through the structure cannot continue and the composite has reached its ultimate density.

By selecting values for the bond and node dimensions, this model fits experimental measurements of gas permeability for cloth layup and 3-D weave preforms and composites

(Figures 6 and 7). The dimensions in the model for the cloth layup preform are consistent with microstructure measurements using high resolution X-ray computed tomography[3]. The 3-D weave becomes impermeable at a lower density than the cloth layup due to its initially lower fiber volume fraction (32%) and to the relatively large size of the "holes" at tow crossings.

DENSIFICATION PERFORMANCE OF PREFORMS

In addition to the transport properties, the model gives the composite density as a function of matrix deposit thickness. For different preforms the deposit thickness needed to reach the percolation limit is a relative measure CVI processing times. For the cloth layup and 3-D weave preforms above the maximum deposit thicknesses are 85 and 120 μm respectively. Thus under similar process conditions the 3-D weave preform will require approximately 50% greater processing time. This result is consistent with the limited experience at ORNL in densification of 3-D weave preforms.

It is desirable to use this model to predict the densification performance of new, untried preforms. Of current interest is a multilayer braid of Nextel fiber used to make free-standing tube preforms[4]. Our approach involves three steps: 1) select model parameters based on examination of the tow and layer spacings in the preform, 2) confirm model parameters by comparison with experimental permeability measurements on the preform, and 3) predict densification performance using these model parameters. This procedure, combining modeling and experimental measurement, may offer a reliable method for quickly testing the densification performance of various preform architectures prior to infiltration experiments.

Initial application of this method to the Nextel braid fiber architecture indicates densification behavior similar to that of the 3-D weave, i.e. longer processing times than for cloth layup preforms. Additional permeability measurements - particularly for the 3-D weave preform - are needed to fully tested this predictive approach.

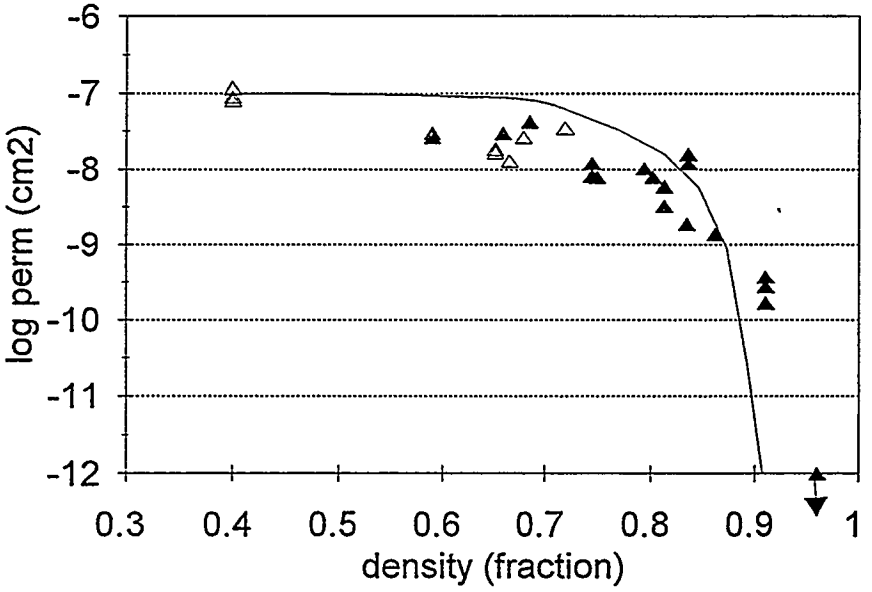

Figure 6. Model shows good agreement with experimental permeability for cloth layup composites. Open triangles are new measurements.

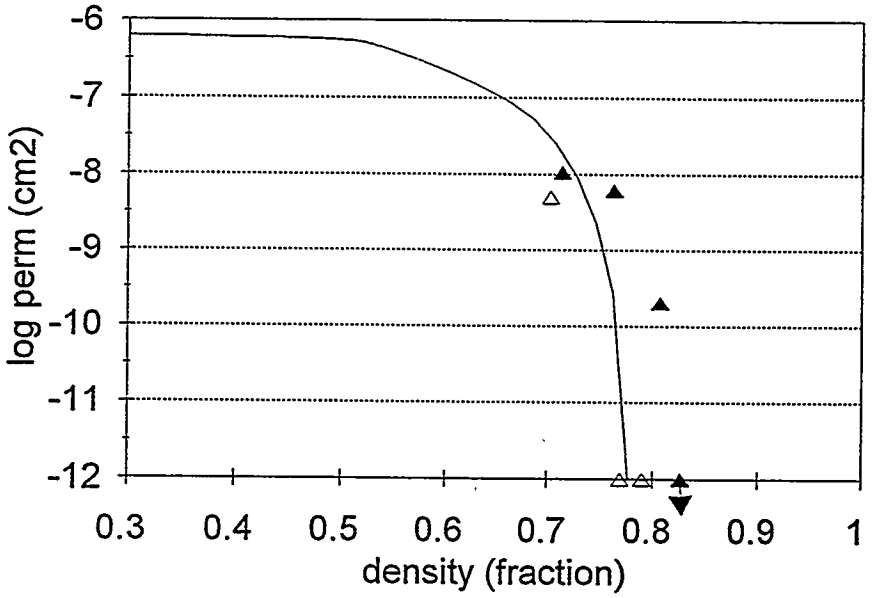

Figure 7. Model shows good agreement with experimental permeability for 3-D weave composites. Open triangles are new measurements.

SUMMARY

Instrumentation and procedures have been completed for measurement of gas permeability and mass diffusivity of fiber preforms and porous materials. Permeability results for composites reinforced with Nicalon fiber in cloth lay-up and 3-D weave architectures are consistent with a node-bond model. Measured permeability values range from near 100 to less than 0.1 darcies. Mass diffusivity is reported as a structure factor relating the diffusion through the porous material to that in free space. These values clearly are correlated closely with the permeability values.

Measured values of gas permeability for the fiber preforms can be used to validate the parameters in the transport property model. In turn, the model can be used to predict the densification behavior of new, untried preforms. Additional measurements are needed to confirm this predictive approach to CVI performance.

REFERENCES

1. Handbook of Chemistry and Physics 68th edition , R. C. Weast, ed., (CRC Press, Boca Raton, Florida) 1988

2. T. L. Starr "Gas transport model for chemical vapor infiltration" J. Mater. Res. 10(9) 2360-2366 (1995).

3. S-B. Lee, S.R. Stock, M.D. Butts, T.L. Starr, T.M. Breunig and J.H. Kinney, " Pore Geometry in Woven Fiber Structures: 0°/90° Plain-weave Cloth Layup Preforms," J. Mat. Res., submitted for publication (1996); S-B. Lee, "Nondestructive Examination of Chemical Vapor Infiltration of 0°/90° SiC/Nicalon Composites," Ph.D. Thesis, Georgia Institute of Technology, December 1993.

4. T.L. Starr, D.Y. Chiang, T.M. Besmann, D.P. Stinton, J.C. McLaughlin and W.M. Matlin, "Rapid Fabrication of Ceramic Composite Tubes using Chemical Vapor Infiltration," Ceramic Transactions, accepted for publication (1996)

JOINING OF SiC CERAMICS AND SiC/SiC COMPOSITES

B. H. Rabin

Idaho National Engineering Laboratory
P.O. Box 1625
Idaho Falls, ID 83415-2218

ABSTRACT

This project has successfully developed a practical and reliable method for fabricating SiC ceramic-ceramic joints. This joining method will permit the use of SiC-based ceramics in a variety of elevated temperature fossil energy applications. The technique is based on a reaction bonding approach that provides joint interlayers compatible with SiC, and excellent joint mechanical properties at temperatures exceeding 1000°C. Recent emphasis has been given to technology transfer activities, and several collaborative research efforts are in progress. Investigations are focusing on applying the joining method to sintered α-SiC and fiber-reinforced SiC/SiC composites for use in applications such as heat exchangers, radiant burners and gas turbine components.

INTRODUCTION

SiC ceramics have considerable potential as elevated temperature structural materials in fossil energy applications. Ceramic-to-ceramic joining methods are needed to allow the fabrication of large or complex shaped parts, and ceramic-to-metal joining methods are needed to allow integration of ceramic components into existing engineering systems. Although considerable efforts have been devoted to understanding the processing, microstructures and properties of SiC-based structural materials, joining remains largely an unresolved issue, particularly with respect to elevated temperature applications. Ideally, joined components should exhibit mechanical properties (including reliability), elevated temperature capabilities and environmental resistance comparable to the base material. Furthermore, the joining method should be practical, cost effective and applicable to different types of SiC ceramics, including SiC fiber-reinforced composites.

This project has successfully developed a reaction processing method for fabricating SiC ceramic-to-ceramic joints [1,2]. The processing method involves tape casting thin sheet SiC+C interlayer precursors, clamping the tape between the SiC parts, and infiltrating the joint with molten Si to form a reaction bonded silicon carbide (RBSC) joint interlayer. This method is attractive since the interlayer material is compatible with SiC, and excellent room and elevated temperature mechanical properties can be achieved.

In addition, as with brazing, external pressure is not required, thus making the process inexpensive and practical compared to alternative joining methods. Details of the joining procedure as well microstructural and mechanical property characterization results have been described previously [1,2]. This paper reports on recent laboratory efforts to improve the joining process, as well as the status of technology transfer efforts.

PROGRESS STATUS

Laboratory Joining Studies

The applicability of the joining method for producing a variety of joint geometries has been demonstrated in previous work [3]. Figure 1 shows examples of several joined structures that were fabricated from sintered α-SiC using the laboratory scale localized induction heating apparatus at INEL. Of particular interest is the ability to fabricate tube-to-tube joints, since long ceramic tube structures are required in applications such as heat exchangers and radiant burners.

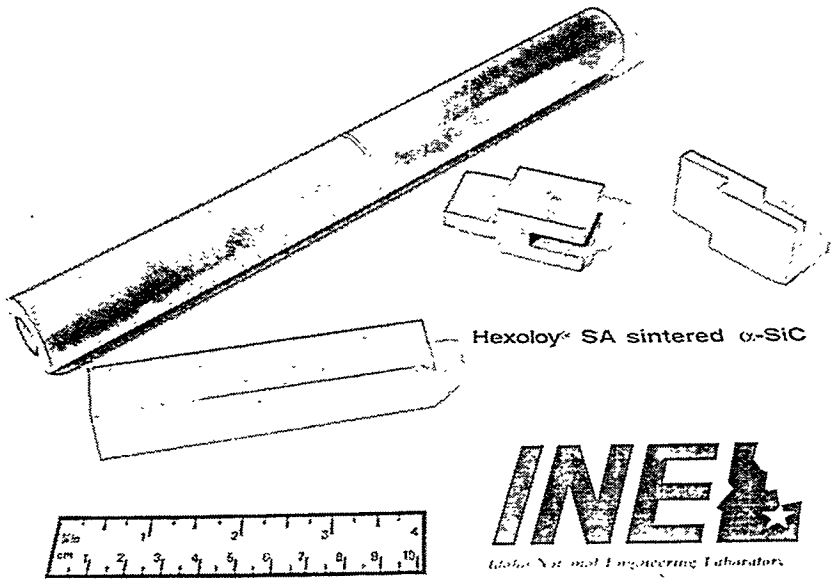

Figure 1. Examples of joined α-SiC structures produced using the reaction processing method developed under this project.

Recently, laboratory experiments have been directed at (1) improving the tape casting formulation to minimize the free Si content of the SiC+Si interlayer joints, and (2) using Si-Mo alloyed melts to produce SiC+$MoSi_2$ joint interlayers containing little or no free Si.

A variety of different tape cast formulations have been prepared wherein the ratio of SiC-to-C powder was varied, as well as the binder content. As in the case of commercial bulk RBSC fabrication [4,5], it is necessary to optimize particle packing so that, after binder burnout, the density of the mixture is close to the calculated theoretical value that results in complete densification, no dimensional change, and minimum free Si content after the Si+C reaction is complete. In general, the processing of defect-free SiC+C tape cast products typically requires higher binder contents than the extrusion of SiC+C mixtures used in commercial RBSC manufacturing. Through careful control of particle sizes, and use of appropriate surfactants and dispersion techniques, suitable tapes can be produced. Currently, the new tape cast formulations being investigated are considered proprietary.

Si-Mo alloys containing 3 wt.% and 6 wt.% Mo were prepared by arc melting. The ingots were crushed in 1-3 mm pellets and used to infiltrate the standard SiC+C tape cast precursor. The presence of $MoSi_2$ in the joints was confirmed using x-ray diffraction (XRD) and energy dispersive spectrometry (EDS), demonstrating that $MoSi_2$ can be formed in joints, as has previously been demonstrated in bulk RBSC ceramics [6,7]. However, the volume fraction of $MoSi_2$ obtained in the joints was well below that required to eliminate all free Si from the interlayer. This is a direct result of the excess quantity of free Si present in these joints. It is expected that this problem will be eliminated through optimization of the tape casting process to minimize the Si content in joints produced without Si-Mo melts.

Technology Transfer Activities

Table 1 lists the ongoing active industrial collaborations and the associated applications being explored for the use of the SiC joining technology developed in this research program.

industrial partner	material	potential applications	project status
DuPont Lanxide Composites, Inc.	CVI SiC/SiC	gas turbine components, heat exchangers, radiant burners	initial specimens joined and tested, detailed studies in progress
Allied-Signal Aerospace	α-SiC	ceramic air heater for HITAF	Phase I completed, Phase II approved for scale-up demonstration
Stone & Webster	α-SiC	ethylene cracking, steam reforming	equipment modifications in progress,
Amercom, Inc.	SiC/SiC	gas turbine components, heat exchangers, radiant burners	investigating applicability to the material
Textron Specialty Materials, Inc.	NBSC	gas turbine components, heat exchangers, radiant burners	investigating applicability to the material
Dow Corning	SiC/SiCN	gas turbine components, chemical pump	investigating applicability to the material

Table 1. Active Industrial Collaborations and Potential Uses for SiC Joining Technology

Cooperative work with DuPont Lanxide Composites, Inc. is in progress to apply the joining technique top CVI SiC/SiC composites. Preliminary shear lap joints were fabricated from both coated and uncoated specimens, and room temperature mechanical testing was carried out. In some joints failure initiated within the excess free Si adjacent of the joint, and crack propagation occurred through the composite material. Failure did not occur at the interface, indicating excellent bond strength was achieved. Joint strengths were ~35 MPa, approximately half the value expected for the composite material. Work is in progress to determine if the joining process significantly degrades composite properties, and additional mechanical testing and failure analysis are in progress. A presentation describing these results was recently given at the 26th Annual Conference on Composites and Structures held in Cocoa Beach, FL, January 14-17, 1996.

Phase II activities have been defined in collaboration with Allied Signal Aerospace Corp., a subcontractor to Foster Wheeler Development Corp., involved in the development of the Ceramic Air Heater for the DOE High Temperature Advanced Furnace. The Phase II work, funded under the High Performance Power Systems Program through DOE-PETC, is expected to being in the near future. This work will involve fabrication and elevated temperature high pressure testing of α-SiC tube-to-tube

joints, and demonstration of the ability to fabricate a subscale tube-manifold assembly in cooperation with Carborundum.

Work has recently been initiated in cooperation with Stone & Webster Engineering Corporation to investigate fabrication of long α-SiC tube assemblies for use in ethylene cracking applications. Preliminary testing of joints in simulated cracking environments will be conducted in collaboration with ORNL. Subsequently, actual tubular assemblies will be fabricated for pilot testing by Stone & Webster.

SUMMARY

Reaction processing methods have been developed for fabricating SiC-to-SiC joints for potential use at elevated temperatures. Laboratory studies are focusing on optimizing the tape casting process to produce joints containing a minimum of free Si, and on producing SiC+$MoSi_2$ interlayers using alloyed Si-Mo melts. Technology transfer activities are continuing.

REFERENCES

1. B. H. Rabin and G. A. Moore, "Microstructure and Properties of SiC-to-SiC Joints Produced by Reaction Bonding," Silicon-Based Structural Ceramics, B. Sheldon (ed.), The American Ceramic Society, Westerville, OH, 1993.

2. B. H. Rabin and G. A. Moore, "Reaction Processing and Properties of SiC-to-SiC Joints," Mat. Res. Soc. Symp. Proc., Vol. 314, 1993, pp. 197-203.

3. B. H. Rabin "Joining of SiC Ceramics and SiC/SiC Composites," ORNL/FMP-95/1, Oak Ridge National Laboratory, August 1995, pp. 41-44.

4. P. Popper, "The Preparation of Dense Self-Bonded Silicon Carbide," Special Ceramics, Heywood, London, p. 209, 1960.

5. C. W. Forrest, P. Kennedy and J. V. Shennan, "The Fabrication and Properties of Self-Bonded Silicon Carbide Bodies," Special Ceramics 5, P. Popper (ed.), British Ceramic Research Association, Stoke-on-Trent, p. 99, 1972.

6. R. P. Messner and Y-M. Chiang, "Processing of Reaction-Bonded Silicon Carbide Without Residual Silicon Phase," *Ceram. Eng. Sci. Proc.*, 9(7-8), pp. 1052-1060, 1988.

7. R. P. Messner and Y-M. Chiang, " Liquid-Phase Reaction-Bonding of Silicon Carbide Using Alloyed Silicon-Molybdenum Melts," *J. Amer. Ceram. Soc.*, 73(5), pp. 1193-1200, 1990.

DEVELOPMENT OF NONDESTRUCTIVE EVALUATION METHODS FOR STRUCTURAL CERAMICS

W. A. Ellingson, R. D. Koehl, H. P. Engel,†
J. A. Wilson and J. B. Stuckey

Energy Technology Division
Argonne National Laboratory
Argonne, IL 60439

†Heaviside Science, Inc.
Melbourne, FL 32934

ABSTRACT

Nondestructive evaluation (NDE) methods using three-dimensional microfocus X-ray computed tomographic imaging (3DXCT) were employed to map axial and radial density variations in hot-gas filters and heat exchanger tubes. 3D XCT analysis was conducted on (a) two 38-mm-OD, 6.5-mm wall, SiC/SiC heat exchanger tubes infiltrated by CVI; (b) eight 10 cm diam. oxide/oxide heat exchanger tubes; and (c) one 26-cm-long Nextel fiber/SiC matrix hot-gas filter. The results show that radial and axial density uniformity as well as porosity, can be assessed by 3D XCT. NDE methods are also under development to assess thermal barrier coatings which are under development as methods to protect gas-turbine first-stage hot section metallic substrates. Further, because both shop and field joining of CFCC materials will be necessary, work is now beginning on development of NDE methods for joining.

INTRODUCTION

Nondestructive evaluation (NDE) technology is being developed to advance the reliable application of ceramic materials to fossil energy systems for improved efficiency and better environmental control. Advanced materials systems under development for fossil energy applications include continuous fiber ceramic matrix composites for hot-gas filters and heat-exchangers and thermal barrier coatings for high gas-firing temperature turbines.

DISCUSSION OF CURRENT ACTIVITIES

Hot Gas Filters and Heat Exchangers

(a) Hot Gas Filters

For hot-gas filter and heat exchanger studies, high spatial resolution 3DXCT methods have been explored.(1-3)

One 38 mm O.D. nextel fiber/SiC matrix hot-gas filter supplied by 3M, was examined at 25 mm intervals along the 26 cm length with data acquired using the ANL 3DCT scanner(2) . The CT images were reconstructed in a 687 x 687 matrix, using 1053 projections with a pixel size of 85 μm x 85 μm, and six rows were averaged or a slice thickness of .51 mm. At each 25 mm section 14 slices were reconstructed. Image reconstructions were done using a newly installed 133 MHz dual pentium computer which has allowed faster reconstruction times. The 32-bit reconstruction files are rescaled to 8-bit scaled data for input to a 3D image display software, IDL, from Research Systems, Inc. This runs on Windows 95 in a separate 150 MHz pentium. However, a software package was written which speeds the input to the IDL software so that density related information can be determined.

Using these methods, hot gas filters have been analyzed for axial density variations as shown in Fig. 1. These data were obtained by using an in-house written software package which allows the average grayscale for each CT slice to be computed. A typical individual CT cross-section is shown in Fig. 2.

Once the 3D data sets (image and histograms) are obtained, the grayscale threshold can be set to allow any particular part of the filter tube viewed in 3D. This could allow quantification of 3D density variations by looking at before and after operation data. Examples are shown in Fig. 3. Figure 3 shows: a) the image of the outer mesh of the 3M hot gas filter; b) the internal wall (refer to Fig. 2a; white inner ring).

By such analysis, volumetric analysis of trapped material in hot gas filters may be accomplished.

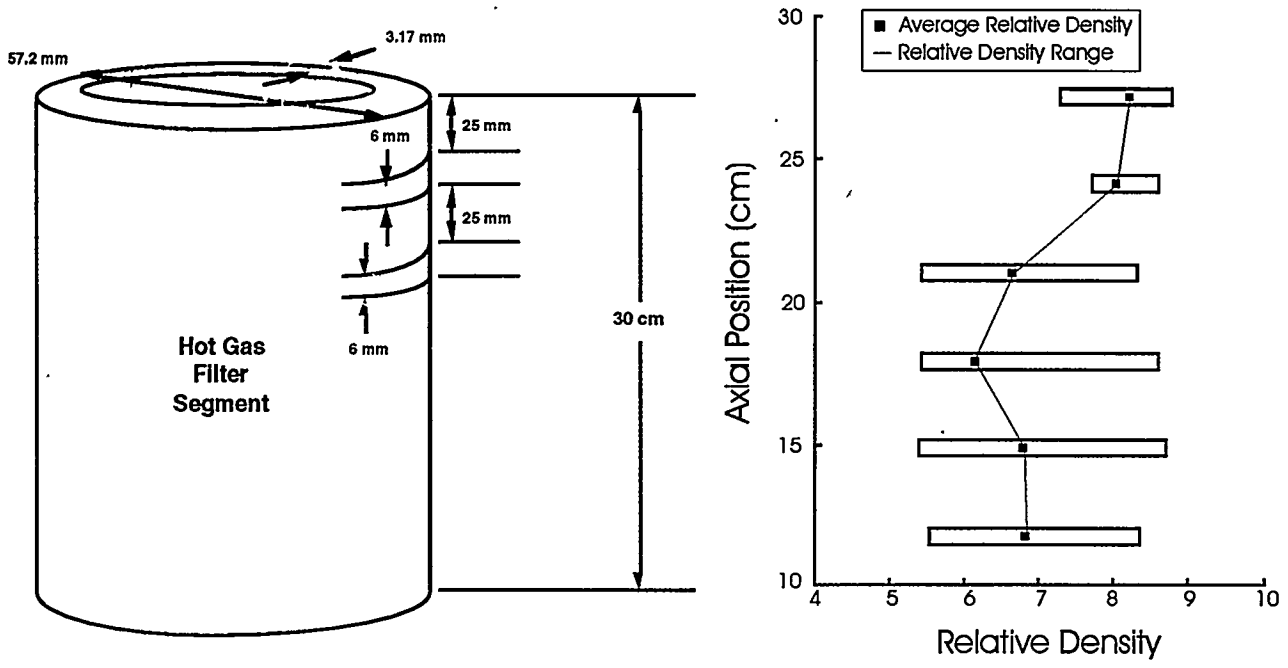

(a) (b)

Fig. 1. Axial density variations for 3M hot-gas filter. (a) Schematic showing data locations. (b) Axial density profile

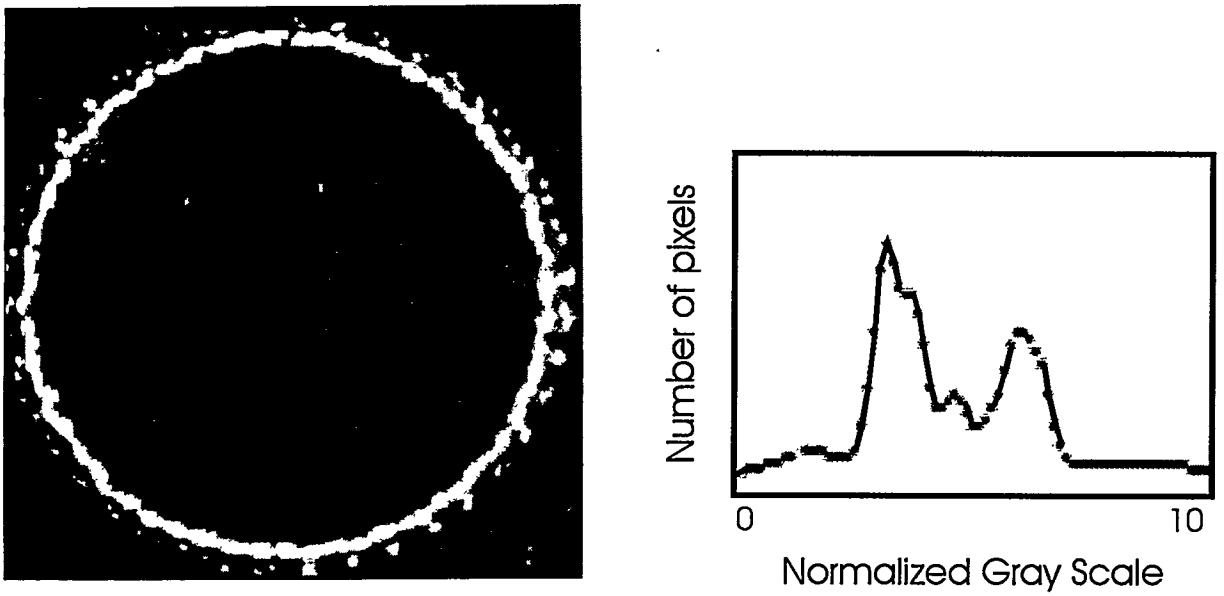

(a) (b)

Fig. 2. Typical X-ray CT cross section through the 3M hot-gas filter and corresponding gray-scale histogram. Note the high-density inner fabric. (a) CT image. (b) Histogram.

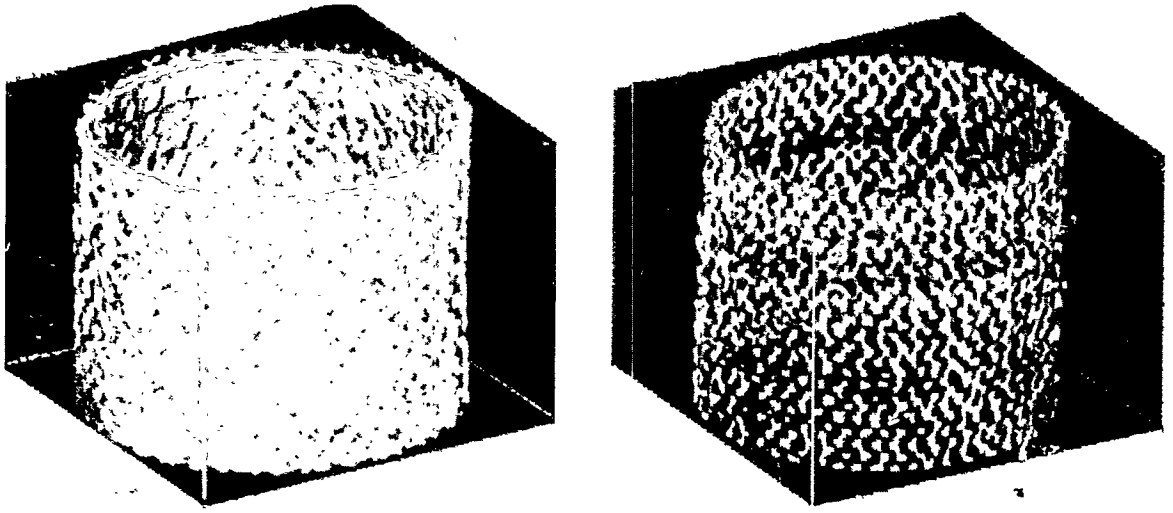

(a) (b)

Fig. 3. Volumetric 3D X-ray CT analysis of 3M hot gas filter. a) Verification of detection of outer mesh. b) Inner surface.

b) Heat Exchangers

For the heat exchanger studies, 3DXCT methods were again explored. Two sets of specimens were available: set 1 consisted of eight 10 cm diam. by 10 cm long specimen provided by Oak Ridge National Laboratory (ORNL). These heat exchanger tubes were provided to ORNL by Babcock & Wilcox and had been exposed to conditions used in the E. I. DuPont hazardous waste incinerator. The specimens for NDE had been cut from 1.5 m long tubes. These specimens are identified in Table 1. Note that specimen AR is an as-received (unexposed) specimen. Set two (see Table 2) consisted of 2 CVI SiC/SiC specimens provided by Virginia Polytechnic Institute (VPI) with considerably different fiber architecture. Tube I appears to be a 3D weave. Tube II appears to be a 2D layup with 45° rotations between plys.

While the NDE work conducted so far consisted of analysis using X-ray CT data acquisition, future work will evaluate air-coupled ultrasonic methods and thermal imaging.

Throughwall Density Variations Including Delamination Detection

3DXCT data were acquired at various locations along the axial length of each of the 10 cm long sections from Set 1. At various azimuthal locations at any axial position, through-wall "line plots" were taken to establish the extent of throughwall density variations.

Table 1. Ceramic Heat Exchanger Tubes Used in NDE Study

Tube ID	Diam (in)	Wall Thickness (mm)	Exposure Position	Visual Observations	Materials	Manu-facturer	Exposure Period
1	4	3.2	Right side Front row	Helically wound fibers	Nextel 610 fibers zirconia matrix	B&W	8 weeks
3	"	6.35	Center of Center row	Hoop wound fibers on surfaces, helically wound internal fibers, thermocouples on tube	Almax fibers zirconia matrix	B&W	27 weeks
4	"	"	Center of Rear row	Hoop wound fibers on surfaces, helically wound internal fibers, some unbonded layers visible	PRD166 fibers zirconia matrix	B&W	27 weeks
5	"	"	Left side Rear row	Hoop wound fibers on surfaces, helically wound internal fibers, some unbonded layers visible	PRD166 fibers zirconia matrix	B&W	27 weeks
6	"	"	Right side Center row	No evidence of fibers	SiC particles alumina matrix	DLC	27 weeks
7	"	"	Right side Rear row	Appears to be helically wound fibers, ~3/8" repeat	Type B mixed oxides	DLC	8 weeks
9	"	"	Left side Center row	Appears to be helically wound fibers, ~3/8" repeat	Type B mixed oxides	DLC	8 weeks
AR	"	"	Unexposed	Hoop wound fibers, some unbonded layers	PRD166 fibers zirconia matrix	B&W	None

DLC = DuPont Lanxide Composites

B&W = Babcock & Wilcox

This includes detection of delaminations. A delamination, clearly visible by inspection, was detectable. 3DXCT analysis, see Fig. 4, shows (see position b) that the visible crack is clearly detected whereas "c" position show only a slight density variation.

Table 2. CVI SiC/SiC Heat Exchanger Tubes for NDE

Tube ID (ANL)	Diam (mm)	Wall Thickness (mm)	Length (cm)	Remarks
I	38	6.35	18.9	Appears to be a 3D braided fiber architech
II	38	6.35	20.3	Appears to be 2D layup 45° interlayer rotation

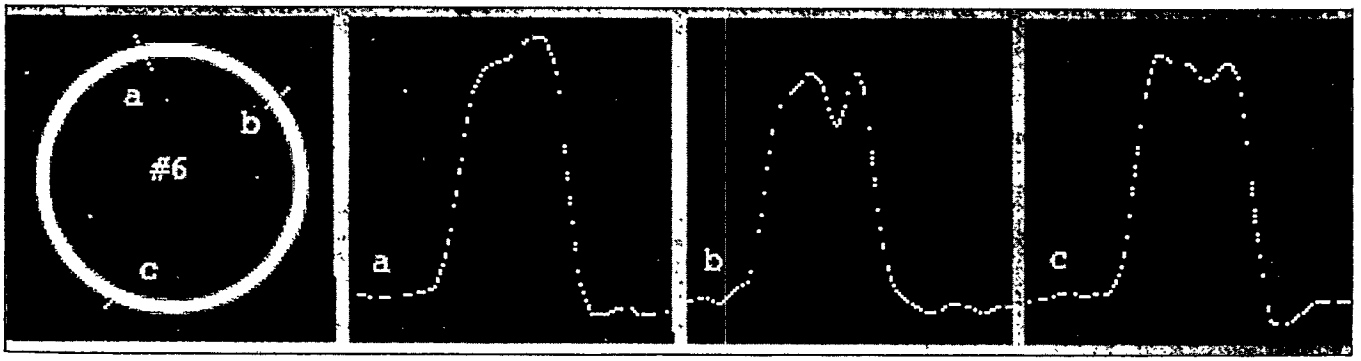

Fig. 4. X-ray CT analysis of heat exchanger tube 6, showing throughwall density profiles at 3 azimuthal positions. Note the delamination detection at location "b".

We conducted similar analysis of the as-received PRD66 hoopwound fiber specimen and again detected delaminations in the wall.

A software package was also developed which allows study of the density variation at any location through the wall using CT axial cross-sections. An example is shown in Fig. 5 for tube 1. Note that at each radial position a 360° density map is determined. The density variations are very small for this particular example.

Axial Density Variations

To establish axial density variations along the tubes, the new software package was used which allows total average density for any CT cross section as a function of axial

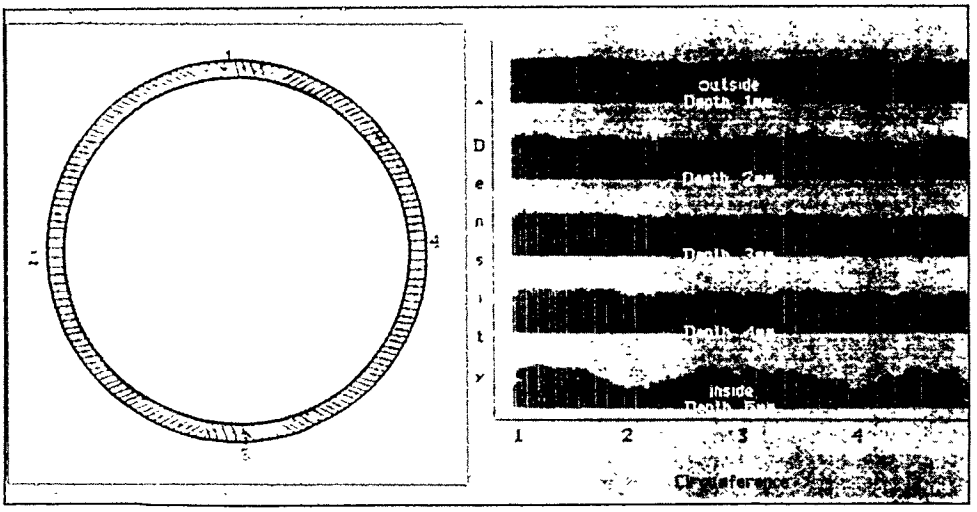

(a) (b)

Fig. 5. X-ray CT sectional image of tube 1 and corresponding 360° density profiles at any position through the wall thickness. a) X-ray CT cross-sectional image. b) five 360° density plots at 0.95, 1.90, 2.85, 3.80 and 4.75 mm from the outer wall.

position to be obtained. Thus density as a function of axial position can be plotted for any CT data set obtained. The axial density analysis is shown in Fig. 6 for the two CFCC specimens of Set 2. The density range for the 3D braid is 1.98 to 2.29 g/cc with a mean of 2.15 g/cc while the 2D laminate is 1.87 to 2.50 with a mean of 2.35 g/cc.

Argonne has a new CT facility which will allow 2-2.5 m long tubes to be studied by CT. In addition, a new air coupled ultrasonic system is now being studied for detection sensitivity for CFCC materials part of the CFCC program. This NDE method will also be examined for applicability to hot-gas filter and heat exchanger tubes.

Thermal Barrier Coatings

Thermal barrier coatings (TBCs) are a key materials element to allow upgrading of turbine gas-firing temperatures and subsequent hot-stage sections for evolutionary turbine materials such as superalloys. The mechanical integrity of these TBC's depends on careful control of the microstructure as well as the bond coat which is used to join the TBC to the alloy substrate.

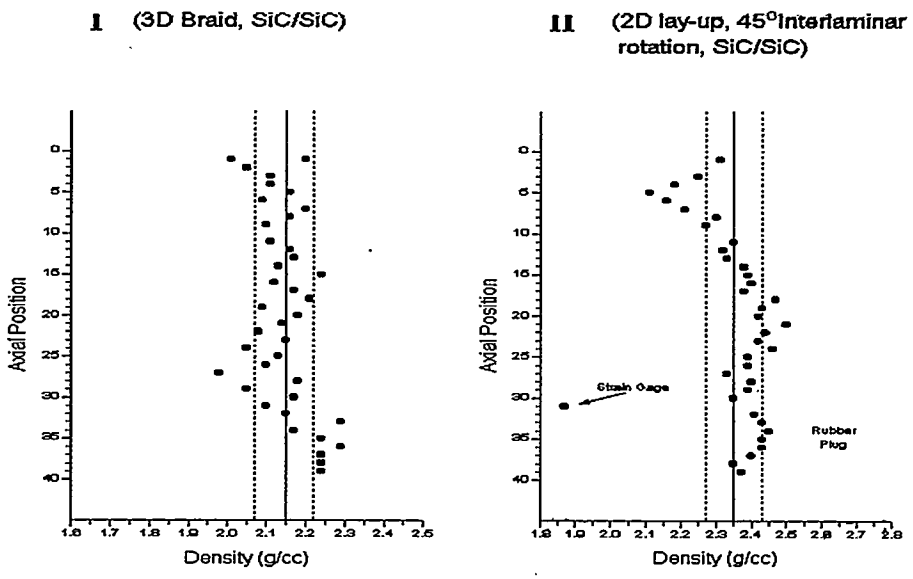

Fig. 6. Axial density profiles for two CVI SiC/SiC CFCC heat exchanger tubes. (a) 3D weave. (b) 2D laminate.

For fossil energy applications, e.g., coal-gas-fired turbines, high temperatures and long-term exposures increases the likelihood of spallation of the TBC and subsequent turbine blade failure. Key development issues for TBCs include: a) reliability of bond coat interface, b) thermal expansion characteristics of the TBC and c) thermal conductivity across the TBC thickness.

For the thermal barrier coating studies, this NDE work initially concentrates on two methods: a) a non-contact, non-invasive method called Time-Resolved-Infrared-Radiometry (TRIR).[4,5] and b) elastic optical scatter.[6] In the TRIR method (see Fig. 7), a thermal excitation source and a high sensitivity, high frame rate infrared camera are located on one side of the thermal barrier coating. The thermal excitation source can be a high energy flash lamp (we have a 1.6 Kj lamp) or a scanning laser. The thermal pulse applies a heat source which penetrates the TBC and reflects off the bond-coat (may reflect off bond coat-substrate interface depending on wave-length of excitation). The reflected thermal "pulse" is then time-dependent recovered by the infrared camera and the individual full-field thermal frames are

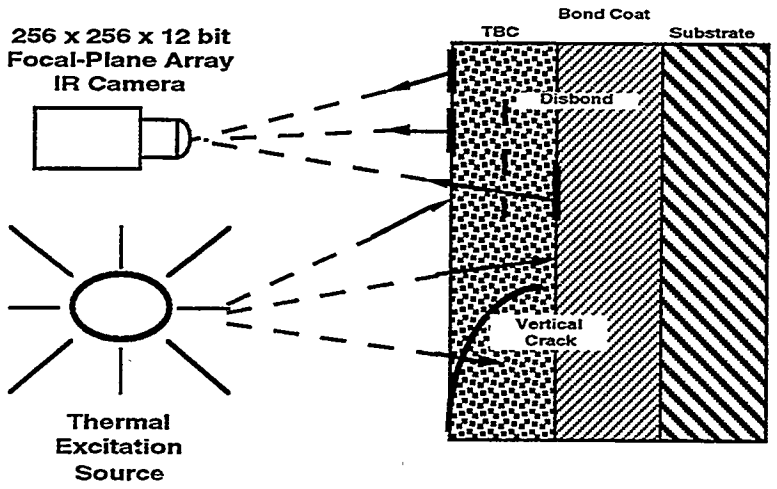

Fig. 7. Schematic diagram of one-sided time-resolved-infrared radiometry method. Note: Schematic shows two defect types: a) disbond, b) vertical crack.

stored in a digital computer. For a disbond of the coating, the temperature rise detected by the camera is much higher as the input heat pulse is not absorbed in the substrate.

Joining

Ceramic-to-ceramic joining methods are usually necessary both for shop fabrication of complex shaped parts and for field repair. There are several potential joint architectures as shown in Fig. 8. These include lap joints, socket flange, straight socket and conical joints.[7]

Rabin et al.[8,9] of Idaho National Engineering Laboratory (INEL), have been developing joining methods as part of this program. They have been primarily focusing on tape casting sheets of SiC + C precursor, clamping the tape between the parts to be bonded, and then infiltrating with molten Si to form a reaction bonded silicon carbide (RBSC) joint interlayer.

Regardless of the method used for joining, NDE methods are necessary to establish the completeness and quality of the joint. The development of NDE methods to study joint quality is the focus of this part of the NDE work.

For the SiC/SiC NDE joining studies, efforts are concentrating on CFCC materials and this work is being conducted in cooperation with the CFCC program. Cooperative efforts have been established with DuPont Lanxide Composites (DLC) as well as Dow-Corning and with INEL.

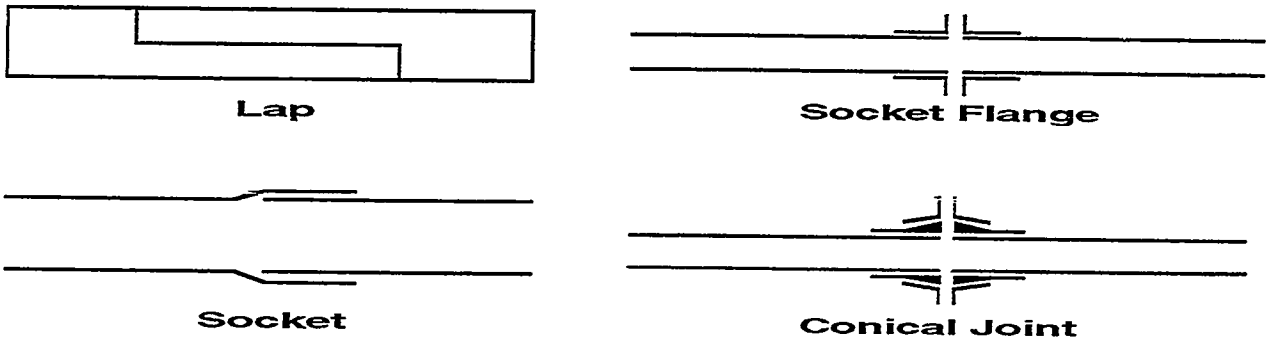

Fig. 8. Schematic diagrams of several possible CFCC joint configurations.

Lap-joint specimens have been received from DLC as noted in Table 3 below.

Table 3. Lap joint CVI CFCC SiC/SiC specimens for NDE

Specimen Number	Specimen Length	Specimen Thickness	Comments
4U-1B-1	41 mm	3 mm	Lap joint at midpoint length Lap joint = 15 mm long
3C-1B-1	43 mm	3 mm	Center lap joint Lap joint ≈ 14 mm long
3C-2A-1	42 mm	3 mm	Center lap joint unknown Lap joint length: estimate 13-14 mm
2A-C	42 mm	3 mm	Center lap joint unknown Lap joint length:estimate 13-14 mm
3U-2A-5	42 mm	3 mm	Center lap joint Lap joint ≈13 mm long

Metallic Si flashing on the specimens was removed by a diamond grit grinding wheel. Several NDE studies will be conducted on these and subsequently mechanical property data will be obtained. NDE studies will include, thermal infrared studies, air-coupled through-transmission ultrasonic studies, pulsed multi-frequency eddy-current and microfocus through-transmission X-ray imaging. As field repairs will be part of joining, NDE methods are being developed which have field application potential.

REFERENCES

1. W. A. Ellingson, M. W. Vannier and D. P. Stinton, "Application of X-ray Computed Tomography to Ceramic/Ceramic Composites," in Chara. of Adv. Mat., E. Henneke, ed., Plenum Press, N.Y., 1991, pp. 9-25.

2. E. A. Sivers, P. A. Holloway and W. A. Ellingson, "Obtaining High-Resolution Images of Ceramics from 3D X-ray Microtomography by Region-of-Interest Reconstruction in Cer. Eng. on Sci., Proc. Vol. 14, No. 17-18, 1993, pp. 463-472.

3. E. A. Sivers, "Use of Multiple CT Scans to Accommodate Large Objects and Stretch Dynamic Range of Detectability in Nuc. Inst. and Methods in Phy. Res. B., Vol. 99, 1995, pp. 761-764.

4. J. C. Murphy, J. W. Maclachlin-Spicer, R. Osiander, W. D. Kevas and L. C. Aamudt, "Quantitative NondestructiveEvaluation of Coatings by Thermal Wave Imaging" in Rev. of Prog. in Quan. Non. Dest. Eval., Vol. 13, 1994, pp. 417-425, eds. D. O. Thompson and D. E. Chimenti, Plenum Press, N.Y., No. 7.

5. J. C. Murphy, L. C. Aamodt and J. W. M. Spicer, "Principles of Photothermal Detection in Solids," in Prog. in Photothermal and Photoacoustic Science and Technology, Vol. 1: Principles and Perspectives of Photothermal and Photoacoustic Phenomena, A. Mandelis, ed., 1992, pp. 41-94, Elsevier, North Holland.

6. J. S. Steckenrider and W. A. Ellingson, "Application of Laser Scattering to the Detection of Surface and Subsurface Defects in Si_3N_4 Ceramics," Cer. Eng. and Sci. Proc., Vol. 15, No. 4, 1994, pp. 382-389.

7. Private communication, B. F. Goodrich-Supertemp, January 1996.

8. B. H. Rabin, "Joining of SiC Ceramics and SiC/SiC Composites," in Proc. of the Ninth Annual Conf. on Fossil Energy Materials, Oak Ridge National Laboratory Report, ORNL/FMP-95/1, 1995, pp. 41-44.

9. B. H. Rabin and G. A. Moore, "Joining of SiC Ceramics and SiC/SiC Composites," in Proc. of Seventh Annual Conf. on Fossil Energy Materials, Oak Ridge National Laboratory Report ORNL/FMP-93/1, 1993, pp. 33-42.

EFFECTS OF FLAWS ON FRACTURE BEHAVIOR OF STRUCTURAL CERAMICS

J.P. Singh, D. Singh, and M. Sutaria

Energy Technology Division
Argonne National Laboratory
Argonne, Illinois 60439

ABSTRACT

We evaluated the effects of fiber coating thickness, fiber orientation, and elevated temperature on flaw morphology and mechanical properties of Nicalon-fiber–reinforced SiC matrix composites with fiber cloth lay-up sequences of 0°/45, 0°/20°/60°, and 0°/40°/60° and fiber coating thicknesses of 0.2 and 0.4 μm. For the three fiber cloth lay-up sequences (0°/45°, 0°/20°/60°, and 0°/40°/60°), mechanical property (first matrix cracking stress, ultimate stress, and work of fracture) initially increase with coating thickness and reach peak values at a coating thickness of 0.2 μm. A further increase in coating thickness does not result in further improvements in mechanical properties; this is related to the role of coatings in protecting fibers from damage during composite processing. Measured values of strength and work-of-fracture of the above composites at elevated temperatures increased with temperature up to 1200°C, but decreased at higher temperatures. This decrease is correlated to in-situ fiber strength and fiber/matrix interface degradation.

Correlations between model prediction and measured room-temperature ultimate strength of composites with 0°/45° and 0°/40°/60° lay-up sequences were established by using in-situ fiber strength characteristics.

The failure modes and degradation mechanisms in hot-gas filters and ceramic composite joints are being characterized by the mechanical and fractographic evaluation techniques established thus far. Correlation of these results with those of nondestructive evaluation can provide critical information for improved quality control.

INTRODUCTION

Continuous fiber–reinforced ceramic matrix composites (CFCCs) are being pursued as materials for structural applications in various industries, including automotive, aerospace,

and utilities, chiefly because of their combination of high strength and toughness at both room and elevated temperatures.[1,2] It has now become clear that the mechanical response of CFCCs, for a fixed fiber content, is largely controlled by intrinsic composite parameters, including strengths of the reinforcing fibers and matrix,[3,4] fiber/matrix interface characteristics,[5,6] and fiber architecture. Therefore, effort is continuing on the evaluation of the effects of fiber cloth lay-up sequence, fiber/matrix interface, and high-temperature environments on flaw generation and resulting mechanical properties of reinforcing fibers and composites.

SPECIMEN FOR FRACTURE STUDIES

To evaluate the effects of fiber cloth lay-up sequence and elevated-temperature service environments on flaw generation and resulting mechanical properties, Nicalon-fiber-reinforced SiC matrix composites fabricated by chemical vapor infiltration (CVI) with various cloth lay-up sequences and fiber coating thicknesses were obtained from Ceramic Composites, Inc. (MD). To date, composites with fiber lay-up sequences of 0°/45°, 0°/20°/60°, and 0°/40°/60° and with carbon coating thicknesses of 0-0.4 μm have been evaluated. Fiber content in the final composite was ≈40 vol.%. These composites were received in plate form and used to machine rectangular bars (≈3 x 4 x 40 mm). The tensile edges of the test bars were bevelled to eliminate stress concentrations and thus avoid edge failures. Density was measured by the Archimedes principle. Approximately five specimens were tested per condition.

ROOM- AND ELEVATED TEMPERATURE MECHANICAL PROPERTY EVALUATIONS AND CORRELATIONS WITH FIBER ARCHITECTURE

Flexure testing in a four–point–bend mode was used to evaluate mechanical properties of the composites at room and elevated temperatures. This method was chosen because of its relatively low cost and ease of use. For room–temperature tests, flexural bars (2.9 x 4.2 x 25.4 mm) were tested with loading and support spans of 9.5 and 19.0 mm, respectively. All tests were conducted at a crosshead speed of 1.27 mm/min at ambient conditions on a universal testing machine.

High-temperature flexure tests were conducted at 1000, 1200, and 1300°C. The composite bars (2.9 x 4.2 x 28.0 mm) were similar to those tested at room temperature, except for an additional SiC surface coating (≈100 μm thick) to prevent oxidizing the exposed carbon

coating on the fiber surfaces. SiC fixtures with loading and support spans of 12.7 and 25.4 mm, respectively, were used, and crosshead speed was 1 mm/min. All specimens were loaded perpendicular to the mat layers. At least three specimens were tested under each set of conditions.

The first matrix cracking stress, or onset of permanent damage to the composites, was determined from the load at which first deviation from the linear variation in the load–vs.–displacement plots was observed. Nominal ultimate stress was determined from the peak load value. Composite work-of-fracture (WOF) was estimated from the total area under the load-specimen displacement plots normalized on the basis of unit cross-sectional area of the fractured composites. True specimen displacement was obtained by subtracting system displacement from total displacement (system displacement was determined by measuring system compliance with a stiff alumina piece).

ANALYTICAL BACKGROUND

Mechanical response of continuous fiber-reinforced ceramic matrix composites with increasing stress levels is dependent on in-situ fiber strength and its distribution. Based on the weakest-link-principle (i.e., failure occurs at the most severe flaw), strength distribution of fibers can be represented by the Weibull distribution function as follows:

$$F(\sigma) = 1 - \exp\left[-\frac{L}{L_o}\left(\frac{\sigma}{\sigma_o}\right)^m\right], \tag{1}$$

where $F(\sigma)$ is the cumulative failure probability at an applied stress σ, σ_o is the scale parameter signifying a characteristic fiber strength at a fiber gauge length, L_o, and m is referred to as the Weibull modulus that characterizes flaw distribution in the material. Thus, by using the Weibull distribution function as given by Eq. 1, it is possible to estimate Weibull scale parameter at some standard gauge length, L, with the following expression:

$$\sigma = \sigma_o\left(\frac{L_o}{L}\right)^{\frac{1}{m}}, \tag{2}$$

The in-situ fiber strength distribution parameters, σ_c and m, can be evaluated by measuring mirror sizes on fractured fibers. Figure 1 shows typical flaw morphology and

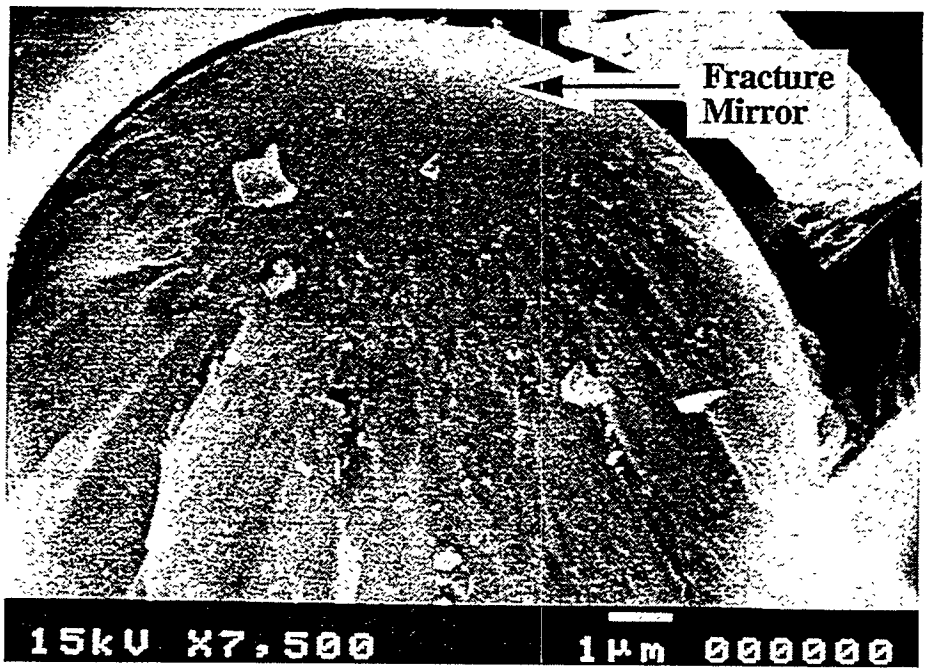

Fig. 1. Fracture surface morphology of SiC (Nicalon) fiber.

associated fracture features such as mirrors (smooth regions) and hackles (regions of multiple fracture planes) on a Nicalon fiber in a composite tested at room temperature. For brittle materials such as glasses and ceramics, it is possible to correlate sizes of fracture features to fracture stress with empirical relationships. For example, fracture stress, σ_f, of the fibers can be obtained from mirror-size measurements with the following relationship:[7]

$$\sigma_f = \frac{3.5K_f}{\sqrt{r_m}}, \tag{3}$$

where r_m is the mirror radius and K_f is the fracture toughness of the fiber. This semiempirical relationship is applicable for mirror sizes much smaller than the fiber diameter.

Based on the fiber fragmentation theory,[8] the resulting value of scale parameter, σ_c, from fracture mirror evaluations is at a gauge length, L_c, that is controlled by fiber/matrix interfacial shear strength and fiber strength. An average value for the gauge length for in-situ fractured fibers can be written as

$$L_c = r\frac{\sigma_c}{\tau}, \tag{4}$$

where r is the fiber radius and τ is the fiber/matrix interfacial shear strength.

The fiber/matrix interfacial shear strength can be determined from average fiber pullout length measurement, h, as[4,8]

$$\tau = \frac{\lambda(m)\, r\sigma_c}{4h}, \tag{5}$$

where $\lambda(m)$ is a nondimensional function and is dependent on fiber fracture statistics.

In-situ fiber strength distribution parameters (σ_c and m) can be correlated to the ultimate strength, σ_{UTS}, of the composite as follows:[8]

$$\sigma_{UTS} = f_l \sigma_c \left[\frac{2}{m+2}\right]^{1/m+1}\left[\frac{m+1}{m+2}\right], \tag{6}$$

where f_l is the fiber volume fraction parallel to the loading direction.

RESULTS AND DISCUSSION

As shown in Table 1, mechanical properties of composites are dependent on both fiber coating thickness and fiber cloth lay-up sequence. For sequences of 0°/45° and 0°/20°/60°, mechanical properties (first matrix cracking stress, ultimate stress, and work of fracture) initially increase with coating thickness and reach peak values at a coating thickness of 0.2 μm. Further increases in coating thickness do not result in further improvements in mechanical properties; this is believed to be related to the role of coating in protecting fibers from damage during processing and in service.[9] These results indicate an optimal coating thickness of 0.2 μm for fibers in the composites. Similar results have been obtained for CVI SiC/SiC composites obtained from Oak Ridge National Laboratory.[9]

Table 1. Room-temperature mechanical property data for SiC/SiC CFCC with various fibercloth lay-up sequences

Fiber Architecture	Coating Thickness (μm)	Composite Density (g/cm^3)	First Matrix Cracking Stress (MPa)	Ultimate Stress (MPa)	Work-of-Fracture (kJ/m^2)
0°/45°	0.0	-	-	105 ± 28	0.16
	0.2	-	95.0	321 ± 131	17.8 ± 6
	0.4	2.25	86 ± 23	153 ± 41	9.8 ± 2
0°/20°/60°	0.0	2.43	-	93 ± 12	0.25 ± 0.6
	0.2	2.31	223 ± 15	319 ± 41	12.7 ± 2.3
	0.4	2.40	115 ± 25	287 ± 48	15.7 ± 4
0°/40°/60°	0.4	2.46	116 ± 28	312 ± 28	14.4 ± 4

For a given fiber coating thickness, mechanical properties of composites with 0°/20°/60° and 0°/40°/60° fiber lay-up sequences were similar in magnitude, whereas composites with a fiber sequence of 0°/45° had relatively lower values. The decrease in mechanical properties for composites with the 0°/45° sequence is believed to have two causes: first, composites with a fiber lay-up sequence of 0°/45° had a lower density (2.25 g/cm^3) than composites with other fiber lay-up sequences (Table 1); the second cause could be related to the smaller fiber fraction in the loading direction for 0°/45° composites relative to that of composites with other fiber lay-up sequences. This will be discussed in more detail in the following sections.

Figure 2 shows typical load-displacement behavior obtained from flexure tests conducted on SiC(f)/SiC composites with the 0°/40°/60° fiber lay-up sequence, at both room and elevated temperatures. Similar variations in load displacement were observed for the 0°/45° composites, and gradual failure was observed in all tests. However, the area under the curve increased somewhat in tests at elevated temperatures. It is recognized here that because of the generation of matrix crack(s) and the shift in the neutral axis, use of the simple beam theory to assess ultimate stresses gives a semiquantitative estimate of ultimate strength. However, the purpose of estimating these values is to compare the relative load-bearing properties of the composites under specific fiber orientations and test conditions.

Figure 3 shows the variation of ultimate strength for the three sets of composites (0.4 μm coating thickness) as a function of temperature. At 1000°C, strength of the 0°/40°/60° composites was similar to its room-temperature value. No 0°/45 specimens were available for tests at 1000°C. Beyond 1000°C, the ultimate strengths of both sets of composites increased dramatically over their room-temperature values, probably because of matrix-softening effects at elevated temperatures. Such behavior is well documented in monolithic ceramics and CFCCs.[10] In general, at elevated temperatures, the 0°/40°/60° composites had higher strengths than those of the 0°/45° composites. However, at 1300°C, strengths of both sets of composites dropped to ≈270 MPa. This decrease above 1200°C is believed due to degradation in strength of the reinforcing fibers.[11-13] For the 0°/20°/60° composites, strength remained relatively unchanged up to 1300°C, except for a slight decrease at 1200°C.

Observed WOF variation with test temperature of two sets of composites (0°/45° and 0°/40°/60°) was similar (see Fig. 4). With increasing test temperature, WOF increased to a maximum at 1200°C because of matrix-softening effects, but dropped rapidly above 1300°C. This drop is related to physical changes in the in-situ Nicalon fibers in composites tested at elevated temperatures; formation of silica at the fiber surface is a distinct possibility at elevated temperatures and can lead to degradation of fiber/matrix interfacial properties. This oxidation can minimize the effective fiber pullout during fracture of the composites, thus accounting for low WOF values.[14]

However, for 0°/20°/60° composites, the WOF remained relatively unchanged up to 1300°C, except for a slight decrease at 1200°C. This behavior is consistent with the observed strength behavior. The difference in mechanical behavior of 0°/20°/60° composites from that of 0°/40°/60° and 0°/45° composites is probably due to specimen-related variations.

To establish the large difference in room-temperature strengths of 0°/40°/60° and 0°/45° composites, we measured their in-situ fiber strengths and correlated them to the composite strengths. In-situ fiber strength measurements by fractography were made on the two sets of composites samples fractured at room temperature. In most fibers, fractures originated at surface flaws, as shown in Fig. 1. Using mirror size measurements and a value of 1 MPa$\sqrt{m}$ as the Nicalon fiber fracture toughness,[4] we estimated fiber strengths from Eq. 3; these values were then used to construct linearized Weibull plots with Eq. 1.

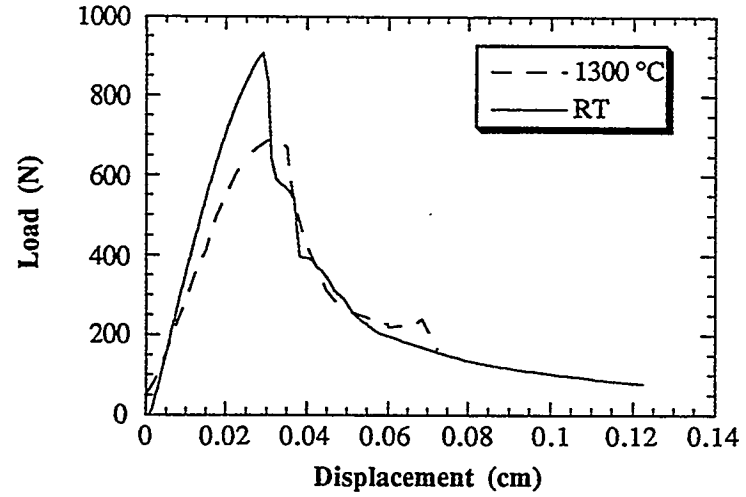

Fig. 2. Typical Load Displacement Observed for 0°/40°/60° Composites Tested at Room Temperature and 1300°C.

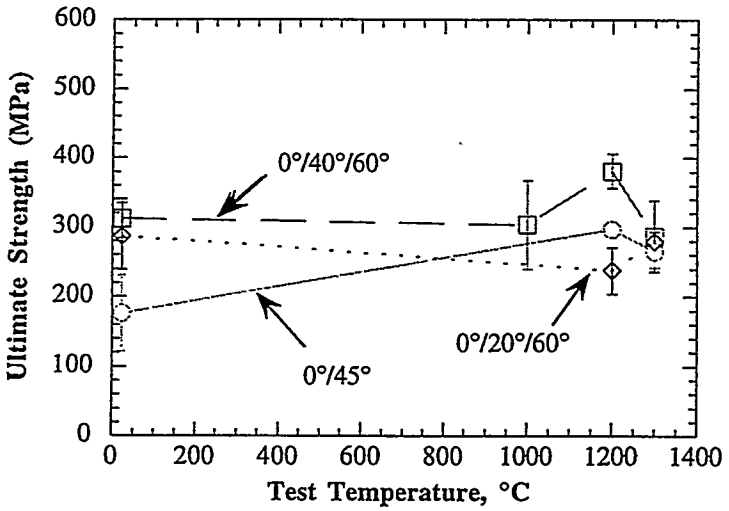

Fig. 3. Variation of ultimate strength with test temperature for SiC(f)/SiC composites with different fiber lay-up sequences.

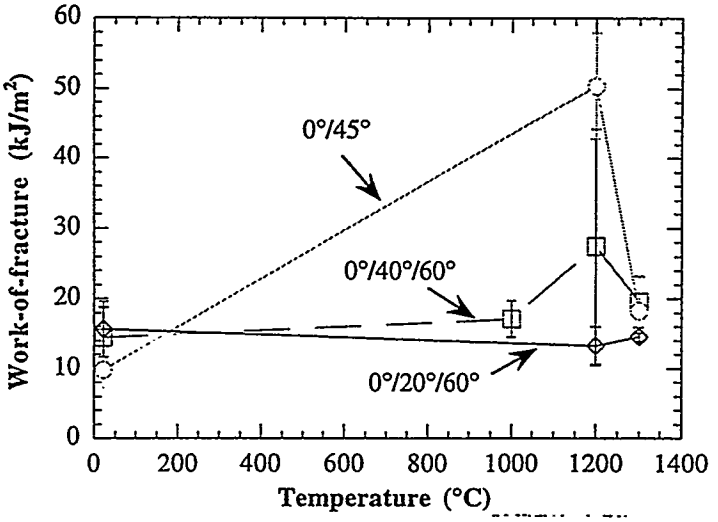

Fig. 4. Variation of work-of-fracture with test temperature for SiC(f)/SiC composites with different fiber lay-up sequences.

The linearized Weibull plots (not shown) of in-situ fibers in 0°/40°/60° and 0°/45° composites tested at room temperature were used to estimate the scale perameter and Weibull modulus. These values for the 0°/40°/60° composites were 2.42 GPa and 4.9, respectively, while those for the 0°/45° composites were 2.38 GPa and 4.9, respectively. Associated average fiber pullout lengths were 160 μm for the 0°/45° and 200 μm for the 0°/40°/60° composites.

For comparison purposes, the scale parameters for fractured fibers in the 0°/40°/60° and 0°/45° composites tested at room temperature were evaluated at a standard gauge length of 1 mm. This was done by first estimating the gauge length, L_c, for the fractured fibers in the composites tested with the two fiber lay-up sequences, based on the average fiber pullout lengths and the scale parameters (Eq. 4). Fiber radius was assumed to be 8 μm, and λ was taken as 2.1 for fibers tested in both 0°/40°/60° and 0°/45° composites.[8] The corresponding values for the gauge lengths of fractured fibers were estimated as 381 and 305 μm for the 0°/40°/60° and 0°/45° composites, respectively. Subsequently, these fiber gauge lengths were used in conjunction with Eq. 2 to estimate scale parameters for the in-situ fibers at a gauge length of 1 mm. The resulting scale parameters at a gauge length of 1 mm for in-situ fractured fibers in the 0°/40°/60° and 0°/45° composites tested at room temperature were 2 and 1.87 GPa, respectively. These values were then used to plot Weibull distribution curves (Fig. 5). Similarity in the Weibull strength distribution plots suggests that there are no differences in in-situ fiber strength characteristics for the two sets of composites.

Equation 6 was used to determine the ultimate strengths of the 0°/40°/60° and 0°/45° composites tested at room temperature. As a first approximation, the fraction of fibers along the loading direction (i.e., 0°) are accounted for in the calculations. Therefore, values of f_l for the 0°/40°/60° and 0°/45° composites are 0.07 and 0.1, respectively. Based on these values and the Weibull parameters, predicted ultimate strengths for the 0°/40°/60° and 0°/45° composites are 117 and 165 MPa. The predicted strength for the 0°/45° composites agrees well with the observed room-temperature strength of ≈153 MPa, while for the 0°/40°/60° composites, there is a large discrepancy. It is possible that in the 0°/40°/60° composites, fibers in the lay-ups oriented at 40° and 30° (in 60° oriented mats) may be contributing to the mechanical response of the composite. If the contribution of these fibers is included in the model, the predicted strength for the 0°/40°/60° is ≈334 MPa; this is in accordance with the observed strength of ≈312 MPa. Thus, from this work it seems that fibers oriented off-axis by more than 40° do not contribute significantly to the ultimate strength of the composites. However, if they are

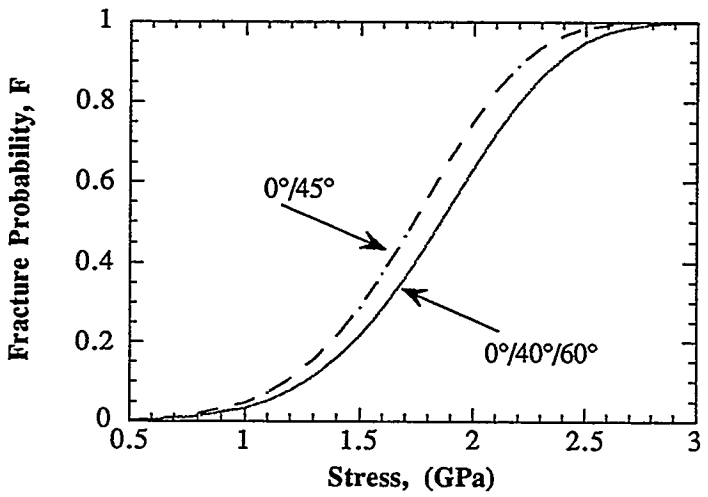

Fig. 5. Weibull strength distribution of in-situ Nicalon fibers in 0°/40°/60° and 0°/45° composites at gauge length of 1 mm.

oriented <40° from the loading direction, they do influence composite strength. Realistically, the contribution of the off-axis fibers to composite strength is expected to change gradually with the off-axis angle and needs to be further quantified. In addition to the fiber fraction available to sustain the applied loads, there may also be a change in the failure mechanism as the fiber lay-up sequence changes in the composites.

ENGINEERING APPLICATIONS

These techniques are currently being used to provide insight into the effects of in-situ fiber strength, fiber coating, and fiber architecture on mechanical performance of engineering composites in service environments. We have begun to investigate engineering components and processes being developed for commercial applications. Specifically, damage evaluation of composite hot-gas filters exposed to service environments and composite joints has been conducted.

Composite Hot-Gas Filters

O-ring compression tests on samples machined from composite hot-gas filters in as-fabricated condition showed an ultimate strength of 19.7 ± 2 MPa. The corresponding value for the ultimate strength of a filter exposed in the Tidd demonstration plant for ≈1100 h was 7.7 ± 1 MPa. This represents a strength loss of 60% during filter exposure. Based on observations in other studies,[9,11] we believe that the reduced ultimate strength is related to the degradation of in-situ fiber strength. Therefore, we evaluated the in-situ strength of reinforcing fibers in as-fabricated and exposed filters by using the fractographic technique

discussed above. Figure 6 shows the distribution of in-situ fiber strengths in composite filters in both as-fabricated and exposed conditions. The average fiber strength in as-fabricated filters is ≈1.7 GPa, while that in exposed composite filter is ≈0.8 GPa. Thus, fiber strength reduction during exposure is ≈60%, in agreement with the strength degradation of the filters themselves. This confirms that filter strength degradation is related to fiber damage.

Composite Joining

An evaluation of in-situ fiber strength in an as-fabricated composite (SiC/SiC) and in a lap joint made of the same composite showed significant fiber strength degradation in the joint section. This is consistent with the observed strength degradation of composite joints. These results validate the use of in-situ fiber strength evaluation for damage evaluation that leads to process optimization of engineering composite components.

ACKNOWLEDGMENTS

The work was supported by the U.S. Department of Energy, Office of Fossil Energy, Advanced Research and Technology Materials Program [DOE/FE AA 15 10 10 0, Work Breakdown Structure Element ANL-1], under Contract W-31-109-Eng-38. The authors thank

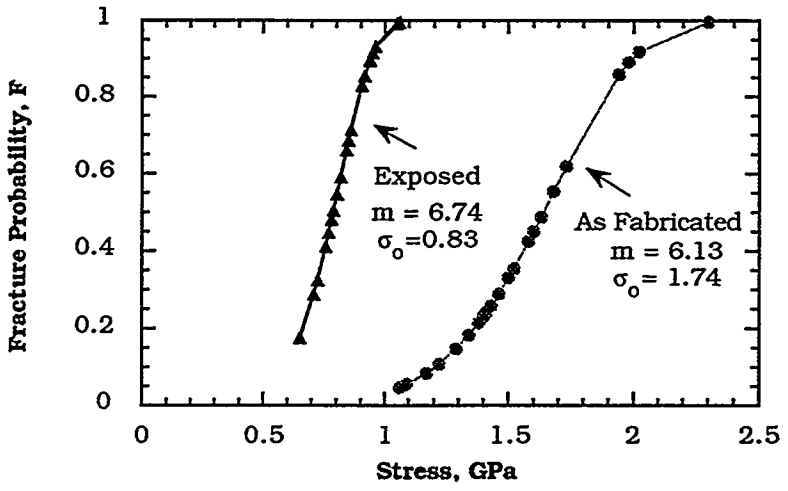

Fig. 6. Weibull strength distribution of in-situ fibers in composite hot gas filters before and after exposure in Tidd demonstration plant.

D. J. Pysher, B. L. Weaver, and R. G. Smith of the 3M Company for providing filter specimens, and James K. Weddell from DuPont Lanxide for providing the composite joint specimen.

REFERENCES

1. A. G. Evans and D. B. Marshall, "The Mechanical Behavior of Ceramic Matrix Composites," Overview No. 85, Acta Metall., 37 [10] 2567–2583 (1989).

2. E. Y. Luh and A. G. Evans, "High–Temperature Mechanical Properties of a Ceramic Matrix Composite," J. Am. Ceram. Soc., **70** [7] 466–69 (1987).

3. T. Mah, M. G. Mendiratta, A. P. Katz, R. Ruh, and K. S. Mazdiyasni, "Room–Temperature Mechanical Behavior of Fiber–Reinforced Ceramic–Matrix Composites," J. Am. Ceram. Soc., **68** [1] C–27–C–30 (1985).

4. M. D. Thouless, O. Sbaizero, L. S. Sigl, and A. G. Evans, "Effect of Interface Mechanical Properties on Pullout in a SiC–Fiber–Reinforced Lithium Aluminate Silicate Glass Ceramic," J. Am. Ceram. Soc., **72** [4] 525–32 (1989).

5. H. C. Cao, E. Bishcoff, O. Sbaizero, M. Ruhle, A. G. Evans, D. B. Marshall, and J. J. Brennan, "Effect of Interfaces on the Properties of Fiber–Reinforced Ceramics," J. Am. Ceram. Soc., **73** [6] 1691–99 (1990).

6. R. N. Singh, "Fiber–Matrix Interfacial Characteristics in a Fiber–Reinforced Ceramic–Matrix Composite," J. Am. Ceram. Soc., **72** [9] 1764–67 (1989).

7. R. W. Rice, Treatise on Materials Science and Technology, Vol. II, pp. 199, Academic Press, New York, 1978.

8. W. A. Curtin, "Theory of Mechanical Properties of Ceramic–Matrix Composites," J. Am. Ceram. Soc., **74** [11] 2837–45 (1991).

9. J. P. Singh, D. Singh, and R. A. Lowden, "Effect of Fiber Coating on Mechanical Properties of Nicalon Fibers and Nicalon-Fiber/SiC Matrix Composites," Ceram. Eng. Sci. and Proc., **15** [4] 456–464 (1994).

10. D. P. Stinton, R. A. Lowden, and R. H. Krabill, "Mechanical Property Characterization of Fiber-Reinforced SiC Matrix Composites," in Proc. 4th Annual Conf. on Fossil Energy Materials, Fossil Energy AR&TD Materials Program, ORNL/FMP-90/1, 3-13 (1990).

11. D. Singh, J. P. Singh, and M. Wheeler, "Mechanical Behavior of SiC(f)/SiC Composites and Correlation to In-Situ Fiber Strength at Room and Elevated Temperatures," to appear in Journal of the American Ceramic Society.

12. T. J. Clark, R. M. Arons, and J. B. Stamatoff, "Thermal Degradation of Nicalon SiC Fibers," Ceram. Eng. Sci. Proc., **6** [7-8] 576-588 (1985).

13. D. J. Pysher, K. C. Goretta, R. S. Hodder, and R. E. Tressler, "Strengths of Ceramic Fibers at Elevated Temperatures," J. Am. Ceram. Soc., **72** [2] 284–88 (1989).

14. R. A. Lowden and D. P. Stinton, "Interface Modification in Nicalon/SiC Composites," Ceram. Eng. Sci. Proc., **9** [7-8] 705-722 (1988).

STRENGTH AND CORROSION BEHAVIOR OF SiC - BASED CERAMICS IN HOT COAL COMBUSTION ENVIRONMENTS

Kristin Breder and Randy J. Parten
High Temperature Materials Laboratory
Oak Ridge National Laboratory
Oak Ridge, TN 37831 - 6069

ABSTRACT

As part of an effort to evaluate the use of advanced ceramics in a new generation of coal-fired power plants, four SiC-based ceramics have been exposed to corrosive coal slag in a laboratory furnace and two pilot scale combustors. Initial results indicate that the laboratory experiments are valuable additions to more expensive pilot plant experiments. The results show increased corrosive attack with increased temperature, and that only slight changes in temperature may significantly alter the degree of strength degradation due to corrosive attack. The present results are part of a larger experimental matrix evaluating the behavior of ceramics in the coal combustion environment.

INTRODUCTION

A new generation of coal fired power plants with increased efficiency, fewer emissions and lower costs are currently being developed.[1,2] Large improvements in efficiencies will require a change to gas turbines (Brayton Cycle) instead of exclusive reliance on steam turbines (Rankine Cycle). Extremely high temperature working fluid is required to boost the efficiency, and the result is that the power plant sub-systems will be exposed to much more corrosive environments than in the present systems. The uses of ceramic heat exchangers are being investigated for those new power plants because of the potential for producing a clean, hot working fluid for the gas turbine.

The leading candidate materials for ceramic heat exchangers are silicon carbide-based materials in the form of sintered SiC, siliconized SiC, or a composite containing SiC. The thermal conductivity of this group of ceramics is good, and the retention of mechanical properties, as well as the thermal shock resistance, is presumed to be adequate for the application. However, relatively little is known about the behavior of these ceramics in the corrosive coal combustion environment, and in order to achieve the desired lifetimes of up to 20 000 h this needs to be determined. Some early studies indicated severe corrosion problems in a coal/oil burning rig,[3-6] and basic coal chemistries were found to be more corrosive than acidic chemistries. More recently modern SiC and a new SiC-particulate reinforced Al_2O_3 composite have been tested in a coal ash environment.[7-11]

EXPERIMENTAL PROCEDURE

The coal ash exposure experiments were carried out using ceramic tubes. NT230 siliconized silicon carbide (SiSiC) from Saint Gobain Norton Industrial Ceramics contained free silicon metal (8 vol%) and some residual porosity. Lanxide DIMOX SiC_p reinforced Al_2O_3 from DuPont Lanxide Composites Inc. was manufactured by the Lanxide Direct Oxidation process (DIMOX) and contained 48 vol% SiC_p, 38 vol% Al_2O_3 and 13 vol% Al-alloy, and some residual porosity. Two sintered SiC were tested; β-SiC from Coors Ceramics Co., and Hexoloy sintered α-SiC from Carborundum Co. The SiSiC and sintered SiC ceramics were tested as machined while the Lanxide DIMOX was reoxidized by the manufacturer after machining.

The tubes were nominally 50 mm (2") OD and 38 mm (1.5") ID and were cut into 150 mm (6") long sections for exposure. A thorough description of the materials have been given previously.[7]

The slags for the exposure experiments were gathered from the taps of three cyclone-fired utility boilers. Two types of Illinois #6 bituminous coals were used. One was from coal burned at the Central Illinois Public Service Coffeen Plant (labeled Coffeen) and was produced from a low sulfur producing mine. The low sulfur (in the form of low FeS_2 content) leads to high viscosity of the slag, so therefore 1.5% limestone was added at the power plant to reduce the viscosity. The second Illinois #6 coal was from the Illinois Power Company Baldwin Plant (labeled Baldwin) and was a mixture of Illinois #6 and Illinois #5 coals, resulting in a typical slag with less Ca and more Fe than the batch from

the Coffeen plant. The third slag came from coal burned at the Northern States Power Riverside Plant, and was produced from the Rochelle mine, Wyoming (labeled Rochelle). Approximately 3% petroleum coke was added at the power plant.

Each slag was analyzed at the University of North Dakota Energy and Environmental Research Center (UNDEERC)[12] and was split from the main barrel according to ASTM D 2013 "Standard Method of Preparing Coal Samples for Analysis." The chemical compositions of the three coal ashes are given in Table 1.

Table 1. Chemical composition of the coal ashes.

Oxide, wt%	Coffeen	Baldwin	Rochelle
SiO_2	52.5	53.4	47.0
Al_2O_3	16.3	18.6	18.6
Fe_2O_3	13.5	17.6	5.3
TiO_2	0.7	0.7	1.4
P_2O_5	0.2	0.0	0.6
CaO	13.1	7.1	19.7
MgO	1.2	0.9	5.7
Na_2O	0.8	0.0	0.9
K_2O	1.6	1.7	0.4
SO_3	0.1	0.0	0.4

The test temperatures were 1090°C to produce a condition of sintered ash, 1260°C for a viscous molten ash, and 1430°C for a fluid molten ash. The tube-sections were placed in a box furnace; an initial layer of coal slag was added; and the furnace was brought up to temperature in 2 h. In order to replenish the coal slag 75 ml was added to each tube length every 48 h through the top of the furnace. Total exposure time was 500 h after which the furnace was slowly cooled to room temperature. After inspection each tube was cut into 14 C-ring specimens for strength testing. The C-rings were placed in a mechanical test system containing a box furnace, re-heated to the exposure temperature and loaded in compression to failure at a fast loading rate (45 N/s). The strength was evaluated using the appropriate formula for C-rings in compression.[13] Three tubes were cut into C-rings

and tested in the as-received condition in order to provide base-line strength data at each test temperature. The strength data were analyzed using Weibull statistics[14,15] and fractography was performed.

One 300 mm long tube section of each material were exposed in a pilot scale combustor in order to tie the laboratory experiments to systems testing. The combustor was a 220 kW (750 000 Btu/h) pilot scale combustor at UNDEERC burning the same type of Illinois #6 coal from the Baldwin plant as described above.[16] The tube was placed in the coal stream in a section at a temperature between 1340°C and 1370°C and the total run was 100 h. One tube of the SiC_p reinforced Al_2O_3 material was placed in the radiant section at the Combustion and Environmental Research Facility (CERF) at (PETC) at a temperature between 1050°C and 1250°C. The CERF is a 150 kW (500 000 Btu/h) pilot scale combustor, and the tube was exposed in the combustor for 1000 h while miscellaneous eastern bituminous coals were burned for other experimental applications.[17] Both these tubes were sectioned into C-rings and strength tested at 1260°C as described above.

Exposure in the Laboratory Furnace

Following are descriptions of the tubes after 500 h exposure in the laboratory furnace. The visual appearance did not vary much between the materials, but varied between the coal slags and temperatures. Of a test matrix of 9 conditions for each material two are remaining at the present time.

At 1090°C the Baldwin slag was lightly sintered together but did not stick to the surface of the tubes except in certain small spots. The surface of the SiC_p reinforced Al_2O_3 was discolored gray-brown from its original gray color, but did not show any obvious surface damage. The surfaces of the other three ceramics remained essentially unchanged with the exception of a few spots of sintered slag stuck on to them.

At 1090°C the Coffeen slag was also lightly sintered together, and a layer was loosely sintered onto the tubes. When the slag was peeled off, there was no obvious surface damage, but some brown discoloration from this darker slag was observed. The viscosity for the two coal slags was similar at 1430°C, but the temperature where the slag starts to solidify was somewhat higher for the Baldwin than the Coffeen slag, and this may explain the difference in appearance at this temperature. Details pertaining to the different viscosities will be included with detailed microprobe work later in the project.

The Rochelle slag was also just loosely sintered on to the tubes after exposure to 1090°C. The slag was yellow-brown in color, but had not caused any discoloration of the tubes.

At 1260°C the Baldwin slag was fused onto the tubes. The slag was brown and had a shiny glazed appearance on the side of the tubes, and was black with large bubbles on the top surface where the slag had been applied.

At 1260°C the Coffeen slag was also well fused onto the tubes, but the appearance was less glazed and the color was uniformly matte brown. There were small bubbles in the slag, but fewer large bubbles at the surface.

At 1430°C the Baldwin slag was very well fused onto the tubes in a thinner layer than for 1260°C. The color was generally matte brown.

At 1430°C the Coffeen slag was very well fused onto the tubes in a thin brown layer. Few bubbles had developed, and it was obvious that the slag had been very fluid at that temperature.

Exposure in Coal Combustors

The tubes which had been exposed in the UNDEERC combustor at a temperature between 1340°C and 1370°C (Baldwin slag), had a highly glazed, even brown slag layer fused onto them. There was some slag build-up on one side, containing areas with large bubbles under the surface. Some material loss was observed on one side of the tubes, this was more pronounced for the SiC_p reinforced Al_2O_3 ceramic than for any of the other specimens. Each of the C-rings were measured and the dimensions will be compared to the as-received dimensions. The appearance of the slag on these tubes was very similar to the appearance of the slag on the tube from the laboratory furnace, (Baldwin slag at 1260°C) indicating a similar temperature level. However, the wall recession was in some cases more severe, indicating that the combustor environment, in which there is rapidly moving combustion gases passing over the tube, would be more severe than the furnace environment.

The slag on the SiC_p reinforced Al_2O_3 tube exposed at PETC at a temperature between 1050°C and 1250°C, was less sintered, which confirmed that the exposure temperature had been under the temperature for creating molten slag. The slag was discolored, was lightly sintered together, and was well attached to the tube. There did not seem to be a serious wall recession for this tube.

Strength Testing

Figure 1 shows the average strengths for the as received C-rings as well as the average strength measured after exposure at the UNDEERC and PETC pilot scale combustors. Testing of C-rings from the tubes exposed in the laboratory furnace is ongoing, and will not be discussed here. C-rings from the tubes exposed in both the pilot scale combustors were strength tested at 1260°C. From the ranges of temperatures given, this was in the high-end for the tube exposed at PETC and in the low end for the tubes exposed at UNDEERC; however, the temperature was chosen as a common denominator, and for ease of comparisons to the as-received data.

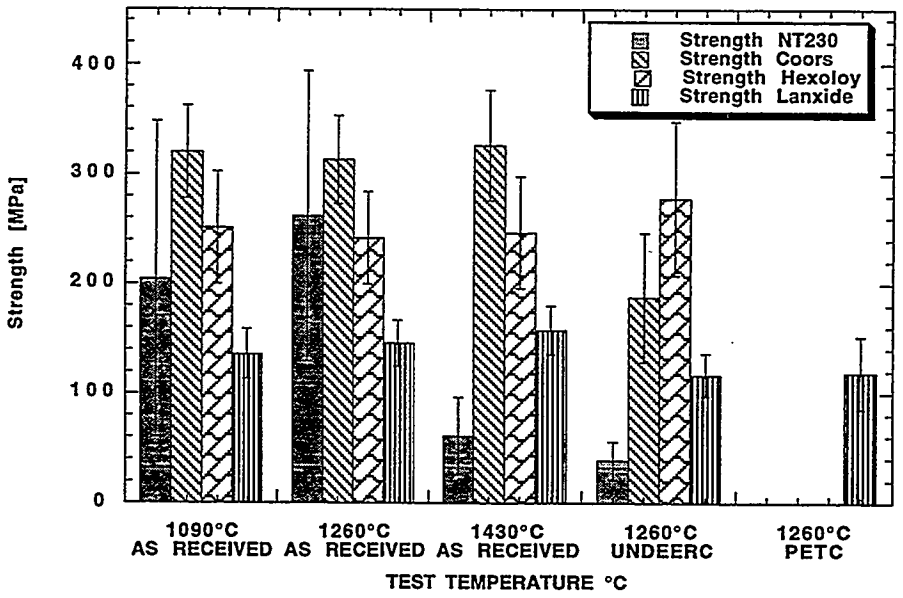

Figure 1. Comparison of strength of C-rings before and after exposure in pilot scale combustor.

Statistical analysis of the strength results for the NT230 SiSiC material showed that there was a significant drop in strength for the specimens tested at 1430°C. This is to be expected as the melting point for Si is 1410°C. The residual strength of the NT230 after the 100 h exposure in the UNDEERC combustor was significantly reduced compared to

the as-received strength measured at 1260°C. The exposed specimens showed some reduction in wall thickness, and the preliminary fractography indicated that fracture generally was initiated from corrosion pits generated during the exposure. The overall variability in the strengths measured for this material was large (high standard deviation and low Weibull modulus), similar to what was observed previously in flexure testing of this material.[7]

The strength of the Coors β-SiC material remained the same over the entire temperature range, but a significant reduction in strength was observed after exposure in the UNDEERC combustor. The preliminary fractography for these specimens indicated a predominance of failure from surface pits or pores, probably related to the exposure. Detailed Scanning Electron Microscopy (SEM) work is needed to determine the extent of these pits.

The strength of the Hexoloy α-SiC was unaffected by the temperature or the exposure at UNDEERC. The exposed specimens failed mostly from pores, but in contrast to the β-SiC the pores in these specimens were mostly in the volume near the surface, and as such unaffected by the exposure. The as-received specimens failed from similar types for pores throughout, consistent with the constant stress level.

The strength of the Lanxide SiC_p reinforced Al_2O_3 ceramic remained unaffected by the elevated temperatures, however, these were all lower than the room temperature strength for this material. After exposure in the two pilot scale combustors there was a slight but significant reduction in strength for this material. However, the strengths of the specimens from the two combustor runs were not significantly different, in spite of the fact that there was an order of magnitude difference in the exposure times for these tubes. This result indicates that the exposure temperature plays a very important role, and that significant differences in life-times may occur for only moderate changes in material exposure temperature. Further, the results indicate that it is important to investigate the influence of the coal chemistries. Also, microprobe studies of the reaction layers will give important additional information on the difference observed for the different slags.

SUMMARY

Four SiC-based ceramics were exposed to three different coal slags in a laboratory furnace. The materials were also exposed in a 100 h pilot scale combustor using one of the same coals. Comparison of the strengths of SiC - based ceramics in the as-received condition to the strength after exposure to coal slag in a pilot-scale combustor indicates that the slag will act as a strong corrodent and reduce the strength of some of the ceramics. There are, however, clear indications that the time for significant strength reduction to occur may vary considerably with only slight variations in temperature. Further work on the corrosion mechanisms, surface damage and strength degradation will be performed in order to determine the boundary conditions for a possible successful implementation of this type of ceramics in the proposed application.

ACKNOWLEDGMENTS

Research sponsored by the U.S. Department of Energy, Office of Fossil Energy, Pittsburgh Energy Technology Center, Advanced Combustion Technology Program, DOE/FE AA 20 10 00 0, under contract DE-AC05-96OR22464 with Lockheed Martin Energy Research Corp.

REFERENCES

1. J. M. Klara, "HIPPS: Beyond State-of-the-art. Part 1," *Power Eng.* **12** 37-39 (1993).

2. J. M. Klara, "HIPPS can Compete with Conventional PC Systems, Part 2," *Power Eng.* **1** 33-36 (1994).

3. M. K. Ferber, and V. J. Tennery, "Evaluation of Tubular Ceramic Heat Exchanger Materials in Basic Coal Ash from Coal-Oil-Mixture Combustion," *Ceram. Bull.* **63** [7] 898 (1984).

4. M. K. Ferber, and V. J. Tennery, "Evaluation of Tubular Ceramic Heat Exchanger Materials in Acidic Coal Ash from Coal-Oil-Mixture Combustion," *Ceram. Bull.* **62** [2] 236 (1983).

5. M. K. Ferber, J. Ogle, V. J. Tennery, and T. Henson, "Characterization of Corrosion Mechanisms Occurring in a Sintered SiC Exposed to Basic Coal Slags," *J. Am Ceram. Soc.* **68** [4] 191 (1985).

6. P. F. Becher, "Strength Degradation in SiC and Si_3N_4 Ceramics by Exposure to Coal Slags at High Temperatures," *J. Mater. Sci.* **19** 2805 (1984).

7. K. Breder and V. J. Tennery, "Materials Support for HITAF, Final Report for Phase I," ORNL/TM-12815, Oak Ridge Nat. Laboratory, Oak Ridge, TN, 1995.

8. T. M. Strobel, J. P. Hurley, K. Breder, and J. E. Holowczak, "Coal Slag Corrosion and Strength Degradation of Silicon Carbide/Alumina Composites," *Cer. Eng. Sci. Proc.*, **15** [4] 579-86 (1984).

9. T. M. Strobel, J. P. Hurley, K. Breder, and J. E. Holowczak, "Coal Slag Corrosion and Strength Degradation of Siliconized Silicon Carbide," *Cer. Eng. Sci. Proc.*, **16** [5] 911-18 (1985).

10. K. Breder, V. J. Tennery, T. M. Strobel, J. P. Hurley, and J. E. Holowczak, "Strength Measurements of Monolithic SiC and Al_2O_3/SiC Composites After Exposure to Coal Slag," *J. Am. Cer. Soc.* **78** [10] 2837-40 (1995).

11. P. F. LaRue, "An Evaluation of the Strength of a $SiC_{(p)}$ / Al_2O_3 Ceramic Matrix Composite Exposed to Coal Slag at Elevated Temperature," M.S. Thesis, University of Tennessee, Knoxville, 1995.

12. J. P. Hurley, "Support Services for Ceramic Fiber-Ceramic Matrix Composites" ORNL/Sub/94-SS112/01, Oak Ridge National Laboratory, Oak Ridge, TN 1995.

13. O. M. Jadaan, D. L. Shelleman, J. C. Conway, Jr. J. J. Mecholsky, Jr., and R. E. Tressler, "Prediction of the Strength of Ceramic Tubular Components: Part1 - Analysis," *Journal of Testing and Evaluation*, **19** [3] 181-91 (1991).

14. W. Weibull, "A Statistical Theory for the Strength of Materials," Ingeniörsvetenskapsakademien, Handligar, No. 151 (1939).

15. S. Duffy and E. Baker, Manual for Spread Sheet Macro for Estimation of Weibull Parameters Based on the Maximum Likelihood Method, Civil Eng. Dep., Cleveland State University, Cleveland Ohio, 1995.

16. T. M. Strobel, J. P. Hurley and J. R. Gunderson, "Pilot-Scale Testing of Silicon-Based Ceramics," to be published in *Cer. Eng. Sci Proc.* **17** [4-5] 1996.

17. K. Natesan, M. Freeman, and M. Mathur, "Corrosion Performance of Materials for Advanced Combustion Systems," pp. 71-83 in Proceedings of the Ninth Annual Conference on Fossil Energy Materials, N. C. Cole and R. R. Judkins, Eds. U. S. Department of Energy, Oak Ridge, 1995.

CORROSION AND ITS EFFECT ON MECHANICAL PROPERTIES OF MATERIALS FOR ADVANCED COMBUSTION SYSTEMS*

K. Natesan
Argonne National Laboratory
Argonne, IL 60439
and
M. Freeman and M. Mathur
Pittsburgh Energy Technology Center
Pittsburgh, PA 15236

ABSTRACT

Conceptual designs of advanced combustion systems that utilize coal as a feedstock require high-temperature furnaces and heat transfer surfaces that can operate at temperatures much higher than those prevalent in current coal-fired power plants. The combination of elevated temperatures and hostile combustion environments necessitates development and application of advanced ceramic materials in these designs. The objectives of the present program are to evaluate (a) the chemistry of gaseous and condensed products that arise during combustion of coal; (b) the corrosion behavior of candidate materials in air, slag, and salt environments for application in the combustion environments; and (c) the residual mechanical properties of the materials after corrosion. The program emphasizes temperatures in the range of 1000-1400°C for ceramic materials and 600-1000°C for metallic alloys. Coal/ash chemistries developed on the basis of thermodynamic/kinetic calculations, together with slags from actual combustors, are used in the program. The materials being evaluated include monolithic silicon carbide from several sources: silicon nitride, silicon carbide in alumina composites, silicon carbide fibers in a silicon carbide-matrix composite, and some advanced nickel-base alloys. The paper presents results from an ongoing program on corrosion performance of candidate ceramic materials exposed to air, salt, and slag environments and their fect on flexural strength and energy absorbed during fracture of these materials.

INTRODUCTION

Coal is a complex and relatively dirty fuel that contains varying amounts of sulfur and a substantial fraction of noncombustible mineral constituents, commonly called ash. Conceptual designs of high-performance power systems (HIPPS) that utilize coal as a feedstock require high-temperature furnaces and heat transfer surfaces capable of operating at higher temperatures than those used in current coal-fired power plants. The combination of elevated temperatures and hostile combustion environments necessitates the use of ceramic materials at least in the first few passes of the heat exchangers in these designs.

The HIPPS concept would employ a combined cycle that uses a gas turbine driven by a working fluid (air) that is separately heated in a high-temperature advanced furnace, in addition to conventional steam turbines.[1] The ultimate goal is to produce electricity from coal with an overall thermal efficiency of 47% or higher (compared with ≈35% for current systems) and to reduce CO_2 emissions by 25 to 30%. The pulverized-coal high-temperature advanced furnace (HITAF) in the HIPPS concept will heat air to an intermediate temperature of ≈1000°C and burn supplemental clean fuel to boost the temperature of air to the

*Work supported by the U.S. Department of Energy, Office of Fossil Energy, Advanced Research and Technology Development Materials Program, Work Breakdown Structure Element ANL–4, under Contract W–31–109–Eng–38.

turbine inlet temperature of ≥1300°C. Use of supplemental fuel can be reduced as the HITAF technology evolves to permit air to be heated to higher temperatures in the furnace. HITAF represents a major departure from conventional pulverized-coal-fired boilers in which only steam is raised to a maximum of 530-620°C. The purpose of the HITAF is to heat the clean working fluid – air – to the required turbine inlet temperatures. At the elevated temperatures of the HITAF, transfer of heat from the combustion gases to the working fluid will be dominated by radiative heat transfer, and the design of the heat transfer surface will be critical for success of the system. Several concepts are under development for the design of the heat transfer surfaces in the HITAF system.[2]

For any of the concepts to be viable for a commercial-scale HIPPS, the heat transfer surfaces will be exposed to much higher temperatures than are prevalent in conventional coal-fired steam-turbine systems. For temperatures of 1000-1300°C, conventional metallic materials do not possess adequate strength properties and/or corrosion resistance for long-term service. In addition, an important difference between the conventional boiler system and the HIPPS is seen in the chemical and physical characteristics of the ash layers that can deposit on the heat transfer surfaces. These deposits are likely to be dominated by alkali sulfates and coal slags in HIPPS, rather than by pyrosulfates or alkali-iron-trisulfates (which are prevalent in conventional pulverized coal-fired boilers), and by the increased mobility of corrosion-accelerating agents in the deposit layers due to the much higher temperature of the heat transfer surfaces in HIPPS. A major challenge is to develop methods to combat severe deposition, erosion, and corrosion (DEC) of heat transfer surfaces exposed to higher-than-normal temperatures. These methods could include fuel selection, cleaning of aggressive contaminants from coal, fine grinding of coal, use of additives, and selection of advanced corrosion-resistant ceramic materials, coatings, and advanced alloys for vulnerable heat transfer sections.

The objectives of the present program are to evaluate (a) the chemistry of gaseous and condensed products that arise in combustion of coal and (b) candidate materials for application in the combustion environments. Chemistry calculations determine the types and amounts of combustion products over the wide temperature range of 700-1700°C and at 1 atm pressure. The experimental program on heat exchanger materials will develop mechanistic information on the roles of material composition, ash constituents, combustion deposits, chlorine, alkali sulfates, and sulfur sorbents in the corrosion process. The program emphasizes corrosion evaluation of materials in air, salt, and coal/ash environments at temperatures between 1000 and 1400°C, as well as measurement of residual fracture properties of the materials after corrosion. Coal/ash chemistries synthesized on the basis of thermodynamic/kinetic calculations, together with slags from actual combustors, are used in the program.

Thermodynamic calculations were used to evaluate the chemistries of gaseous and condensed phases that occur during combustion of coals.[2,3] Based on the results of these calculations, the general behavior of the solution phase under oxidizing conditions can be described as follows. A liquid solution phase, consisting mostly of silicates of aluminum, calcium, sodium, magnesium, and iron, is present at 1730°C. The mole fraction of Na_2SO_4 phase in the liquid is <0.01 above 1280°C. Na_2SO_4 concentration rises rapidly as the temperature decreases and becomes a major component of the solution at 980°C. The mole fraction of Na_2SO_4 may increase to 0.9 or more at 980°C. These compositional changes can have implications for the

corrosive behavior of the liquid condensates. In the temperature range of interest in HIPPS, the predominant deposits are either mullite or Ca-rich aluminosilicates. The silicate liquid may be even more corrosive and have worse fouling tendencies than sulfates because of (a) high-temperature conditions, (b) adhesive behavior of the silicates, and (c) solubility of ceramic materials, which are probably higher in silicate melts than in sulfate melts.

EXPERIMENTAL PROCEDURE

Laboratory Experiments. The materials selected for the laboratory experimental program include advanced metallic alloys, monolithic ceramic materials, and ceramic-matrix ceramic composites; they are listed in Table 1, together with their manufacturers. Hexoloy SA is a sintered form of alpha silicon carbide with >98% of theoretical density. It has a very fine grain structure (8 μm) for excellent wear resistance, contains no free silicon, and has been reported to be chemically resistant in both oxidizing and reducing environments. SiC (p) in Al_2O_3 material was fabricated by Du Pont-Lanxide by a direct metal oxidation process and has an Al_2O_3 matrix containing dispersed SiC particulates. The material also exhibited some free Al in the matrix. Siliconized SiC material (identified as NT 230) made by Norton/TRW. SiC Fiber/SiC Matrix material is made by Du Pont with a chemical vapor infiltration process. It is recommended for service requiring high strength, high-temperature properties, and light weight. The material exhibits creep deformation at temperatures >1200°C, contrary to the behavior of Hexoloy SA and NT 230, in which creep was virtually absent. The material consisting of SiC in an Si matrix is made by INEX, Inc., and has been used in tubes for natural-gas-fired heat exchangers. The material containing SiC fibers in Si carbide was also fabricated by Oak Ridge National Laboratory.

Coupon specimens measuring 2 cm x 2 cm x 2-3 mm were prepared from several of the above–listed materials for salt- and slag-exposure experiments. Dimensions and initial weights of the specimens were measured prior to exposure. Salt tests were conducted at 1000 and 1200°C for 168 h in the presence of Na_2SO_4 or a mixture of Na_2SO_4 and NaCl. Tests in the presence of three different slags were conducted at 1200°C for a test time of 200 h. Table 2 lists the compositions of slags and the coals that were combusted to obtain these slags. Analysis shows that the slag obtained from Illinois #6 coal was richer in Fe_2O_3 and leaner in CaO and MgO, while the reverse is seen for slag from the Rochelle coal. Slags #43 and XX typify the slags derived from coals in the eastern U.S. while slag #47 is typical of that from western coals.

Table 1. Ceramic materials selected for corrosion tests

Material	Manufacturer
Hexoloy SA	Carborundum
SiC (p) in alumina	Du Pont/Lanxide
Siliconized SiC (NT 230)	Norton/TRW
Silicon nitride (NT 154)	Norton/TRW
SiC in Si matrix	INEX, Inc.
SiC fibers in SiC matrix	Du Pont
SiC fibers in SiC matrix	ORNL

Table 2. Compositions of slags for laboratory study

Compound	Slag 43/ Illinois #6	Slag 47/ Rochelle	Slag XX/ Illinois #6
SiO_2	52.9	47.1	53.3
Al_2O_3	16.6	18.8	18.6
Fe_2O_3	12.9	5.2	17.6
CaO	13.0	19.6	7.2
MgO	1.3	5.8	1.0
Na_2O	0.8	0.9	0
K_2O	1.6	0.3	1.7
SO_3	0.1	0.3	0

In addition, the effect of air oxidation, salt exposure, and exposures to slag from Illinois #6 and Rochelle coals on the flexural strength of four of the candidate materials were evaluated by preexposure to the specific environment and postexposure four-point testing of the specimens in vacuum. For these specimens, the temperature was maintained at 1200°C for both the preexposure and mechanical test. The flexural test involved bending a specimen of rectangular cross section until fracture. The specimen dimensions were 1.0 x 0.188 x 0.064 and the salt/slag exposed surface was maintained under tension during the test. The data on the load that caused fracture and the area under the load-displacement curves were used to calculate the flexural strength of the material and the energy absorbed to complete the fracture.

Combustor Experiments. High-temperature materials were tested by exposing samples of several ceramic materials in the CERF at the Pittsburgh Energy Technology Center.[3] The CERF is a state-of-the-art, 0.5 million Btu/h pilot-scale combustion facility designed to achieve similarity with full-scale utility and industrial boilers. It is designed to closely duplicate typical full-scale specifications for solid fuel fineness or liquid fuel atomization quality, burner relative mass flow (fuel and air) and velocities, furnace temperature distributions, radiant furnace residence time, and convective section gas velocity. Material exposures in CERF are being conducted in a piggyback mode, whereby normal CERF testing would proceed in terms of evaluating combustion of various coals and coal blends. With this approach, comparative assessments of many materials at different locations could be made economically before pursuing dedicated-materials CERF tests that would require continuous operation of the facility for 1000 h or more. To minimize thermal stresses during exposure, samples were placed in the CERF prior to the start of each test and removed after the CERF was cooled to room temperature. Coupon samples of several of the ceramic materials were mounted on a water-cooled, high-temperature materials testing probe that uses welded clips and pins to hold the samples. Ceramic specimens were exposed during several 100-h runs in which Pittsburgh coal and a blend of Alaskan/Russian coal were burned. The compositions of the coals used in CERF runs were similar to those that generated slags for the laboratory test program.[3]

EXPERIMENTAL RESULTS

Oxidation in Air

Oxidation of ceramic materials such as monolithic and composite SiC, Si_3N_4, and SiC-dispersed Al_2O_3 involves reaction of carbide and nitride phases to Si-rich oxides. Oxidation rate is generally influenced

by porosity of the material and exposure temperature. Figure 1 shows the weight changes for several of the materials exposed to air at 1200°C. It is evident that most of the SiC and Si_3N_4 materials oxidize at a low rate at 1200°C. The two exceptions are SiC(p) in Al_2O_3 and SiC(f)/SiC made by ORNL. In the former, the increase in weight in the early stage of exposure is due to oxidation of free Al in the surface region of the sample. After ≈100 h exposure, the oxidation rate slows but is still higher than that of other materials, indicating oxidation of free Al in the interior of the material, but dictated by the diffusion of oxygen. The increased rate of oxidation for the latter material can be attributed only to lack of formation of glass phase at the grain boundaries, in contrast with the Du Pont made material which has additives that lead to glassy phase formation. Oxidation can occur via either the passive mode in which a solid SiO_2 phase forms and can offer protection against further oxidation, or via active oxidation in which the SiO phase forms and can volatilize, resulting in accelerated oxidation of the material. Figure 2 shows the regions of active and passive oxidation as functions of temperature and pO_2.[4] Experiments conducted with these materials at temperatures of 1000-1400°C in a dry air environment showed that the materials undergo passive oxidation.

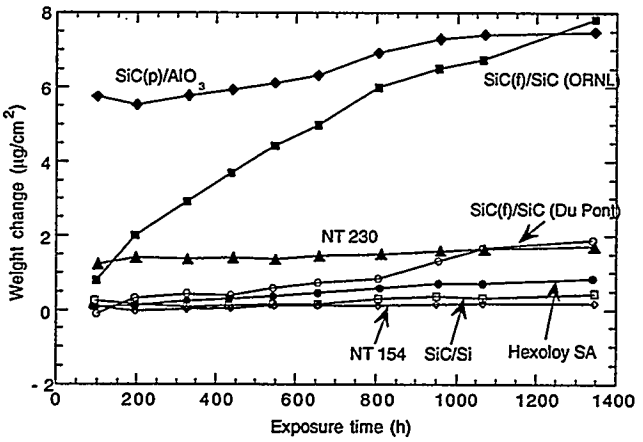

Fig. 1. Oxidation behavior of several ceramic materials in dry air at 1200°C

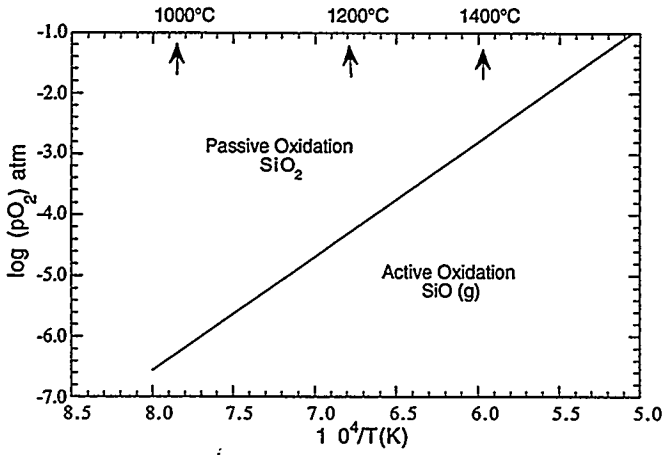

Fig. 2. Regions of active and passive oxidation of SiC in dry air

Exposure to Salt Environment

Salt-induced degradation of these materials involves reactions between the ceramic materials and alkali sulfates such as Na_2SO_4 and K_2SO_4 and alkali chlorides such as NaCl and KCl. In the combustion gas environment, the concentrations of oxygen and of sulfur as SO_2 and SO_3 determine the sodium oxide activity via the reaction $Na_2SO_4 = Na_2O + SO_3$. Subsequently, the silica phase that forms on the ceramic materials can react with Na_2O to form compounds such as $Na_2O{\cdot}XSiO_2$, where X can be 0.5, 1, 2, or 4. This mode of degradation of ceramic materials requires that Na_2O activity be sufficiently high and is usually possible in gas turbine systems where slag constituents are virtually absent. In such instances, the liquid phase can dissolve the protective SiO_2 scale and also result in penetration of the liquid reaction products into the substrate ceramic material, thereby mechanically weakening the material. To examine the effect of salt deposit, specimens were exposed for 168 h at 1200°C to a gas stream of 1 vol.%SO_2-air was passed over Na_2SO_4 salt maintained at temperatures between 700 and 1400°C. The materials selected for these tests were Hexoloy SA, SiC(p)/Al_2O_3, NT 230, and NT 154. Figure 3 shows the specimen weight change after 168 h at different salt temperatures. Na_2SO_4 has a melting temperature of 884°C, and the samples exposed to solid salt at 700-900°C did not exhibit significant corrosion. The weight increase of the SiC(p)/Al_2O_3 is primarily due to oxidation of free Al in the material. Even at a salt temperature of 1000°C, the vapor pressure of Na_2SO_4 is low enough to prevent significant corrosion of the exposed materials. At salt temperatures of 1200°C and higher, corrosion of the SiC-based materials was evident, while the SiC(p)/Al_2O_3 was resistant to salt-induced corrosion. In the absence of Al_2O_3, the monolithic and composite SiC and Si_3N_4 materials oxidize to form SiO_2, which reacts with Na_2SO_4 to form compounds of compositions $Na_2O{\cdot}XSiO_2$ and melting temperatures of 875-1110°C; these compounds lead to enhanced corrosion. The presence of Al_2O_3 in the Du Pont/Lanxide material leads to formation of mullite ($Na_2O{\cdot}Al_2O_3{\cdot}2SiO_2$) with a melting temperature of 1526°C resulting in low corrosion, if any, at temperatures of 1200 and 1400°C in the present investigation. In coal-fired combustion systems, the presence of slag constituents determine the thermodynamic activity of various deposit constituents, and alkali-sulfate-induced corrosion is generally not dominant.

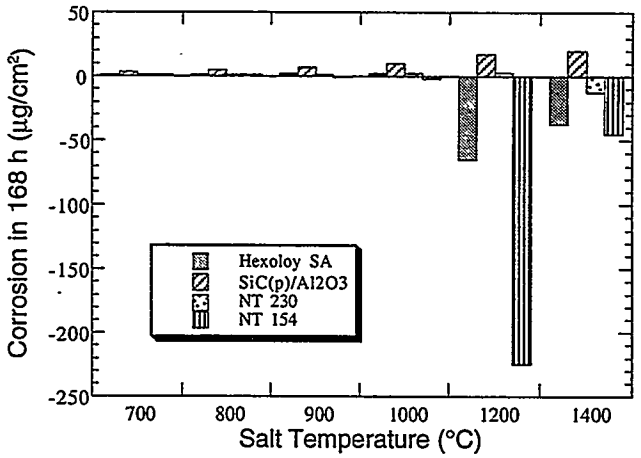

Fig. 3. Effect of sodium sulfate salt condensate on corrosion behavior of several ceramic materials at 1200°C

Corrosion in Slag Environments

In laboratory slag tests, the materials behaved differently than in salt tests. The specimen showed significant surface cracking but the slag itself did not seem to penetrate the sample, as evidenced by energy-dispersive X-ray (EDX) analysis of specimen cross sections. Because Na_2O activity in the slag is relatively low, the deposit did not melt, but significant bubbling of the slag was noted, probably due to formation of SiO vapor in a reducing condition established locally by entrapped carbon in slag. All three slags exhibited similar appearance after testing and also all three specimens exposed to different slags appeared similar, indicating that coal slag chemistry has little influence in these short exposures. In the CERF exposure conducted with Pittsburgh coal, the specimen exhibited a thin layer of deposit after ≈100 h of testing. X-ray diffraction analysis of the deposit indicated predominantly mullite ($3Al_2O_3 \cdot 2SiO_2$), with some ordered albite [$(Na,Ca)Al(Si,Al)_3O_8$] and traces of hematite. No significant degradation of the sample was observed in scanning electron microscopy (SEM) and EDX analysis. In the CERF exposure conducted with Alaskan/Russian coal, the dominant phases were anorthite ($CaO \cdot Al_2O_3 \cdot 2SiO_2$), calcium aluminum silicate ($CaO \cdot Al_2O_3 \cdot SiO_2$), and ordered sodium anorthite $(Ca,Na)(Al,Si)_2Si_2O_8$. These Ca-rich silicates also have melting temperatures >1400°C, and reactions between the coal ash deposit and the ceramics occur predominantly in the solid state. The experimental results also indicate that Na_2O activities in the deposits (with combustion of coals containing Fe_2O_3 and CaO) are sufficiently low to form liquid sodium silicates of various types in coal-fired systems. This may qualitatively indicate that the material may be susceptible to cracking at elevated temperatures by particle impingement.

Baseline Mechanical Properties

Four-point bend tests were conducted on Hexoloy SA, NT 230, SiC in Si matrix, and SiC(f) in SiC matrix materials at 1000, 1200, and 1400°C. The load to cause fracture measured in the test is used to calculate the flexural strength for the materials using the expression

$$\sigma = \frac{3(L_1 - L_2)P}{2t^2 w},$$

where σ is flexural strength in MPa, L_1 and L_2 are distance between support points and load points, respectively, P is load, and t and w are thickness and width of the specimen, respectively. The test technique produces a nonuniform stress distribution with the maximum tensile stress in the outer skin of the specimen. Figure 4 shows the flexural strength of the materials as a function of temperature. The results show that Hexoloy SA maintains fairly high strength (in the range of 350-400 MPa) at up to 1400°C. Flexural strength of NT 230 is somewhat higher than that of Hexoloy SA up to 1200°C and seems to drop to ≈300 MPa at 1400°C and ≈180 MPa at 1450°C. The material SiC in Si matrix had a relatively lower strength of 100-120 MPa up to 1200°C and dropped to ≈70 MPa at 1300°C. The material SiC(f) in SiC matrix exhibited strength values comparable to those of Hexoloy SA at temperatures up to 1200°C but the values dropped at temperatures above 1200°C and comparable to those observed for NT 230. The load-displacement curves from these baseline tests were also used to calculate the area under the curves, which is indicative of the absorbed energy during fracture. The absorbed energy values can differntiate between the monolithic and composite

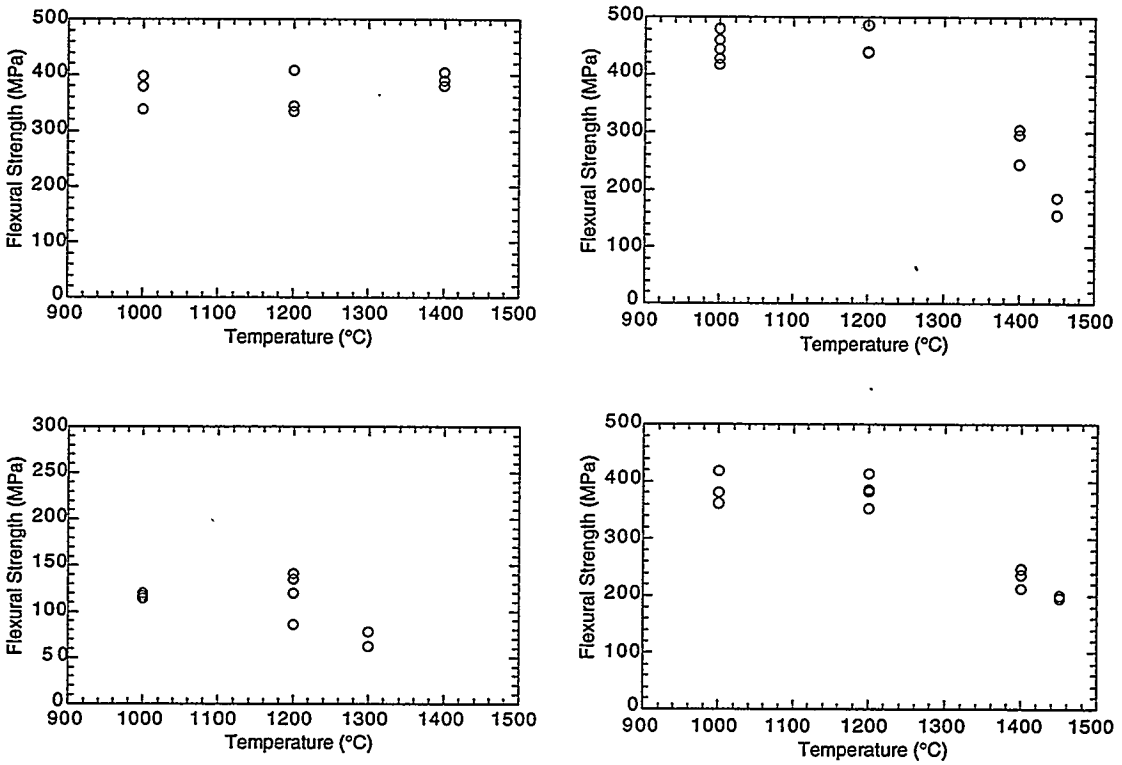

Fig. 4. Flexural strength data as a function of temperature for Hexoloy SA (top left), NT 230 (top right), SiC in Si matrix (bottom left), and SiC(f) in SiC matrix (bottom right) at 1200°C

materials because monolithic materials (such as Hexoloy SA) rarely exhibit creep prior to fracture while composites, such as SiC(f)/SiC, generally exhibit significant creep deformation prior to fracture. The fracture energy values for the materials will be presented in the next section, along with data obtained for the materials after exposure to corrosive environments.

Effect of Corrosion on Mechanical Properties

To examine the role of exposure environment several specimens of the four cermic materials such as Hexoloy SA, NT 230, SiC in Si matrix, and SiC(f) in SiC matrix were preexposed for 200 h at 1200°C to dry air, Na_2SO_4 salt, 75wt.% Na_2SO_4-25 wt.% NaCl mixture, and three different coal slags, identified as 43, 47, and XX. After exposure, the specimens were mechanical tested in vauum at 1200°C. In these tests, the specimen surfaces exposed to the salt and slag environments were on the support side of the fixture, ensuring a tensile mode of loading for the surfaces exposed to corrosive environments.

Figure 5 shows the flexural strength for the four materials under baseline condition and after exposure to different environments. It is evident that exposures of 200 h in different environments had very little influence on the strength of Hexoloy SA material. Analysis of fracture surfaces of exposed specimens showed formation of thin layers of silica in air exposure, and virtually no salt or slag penetration of the

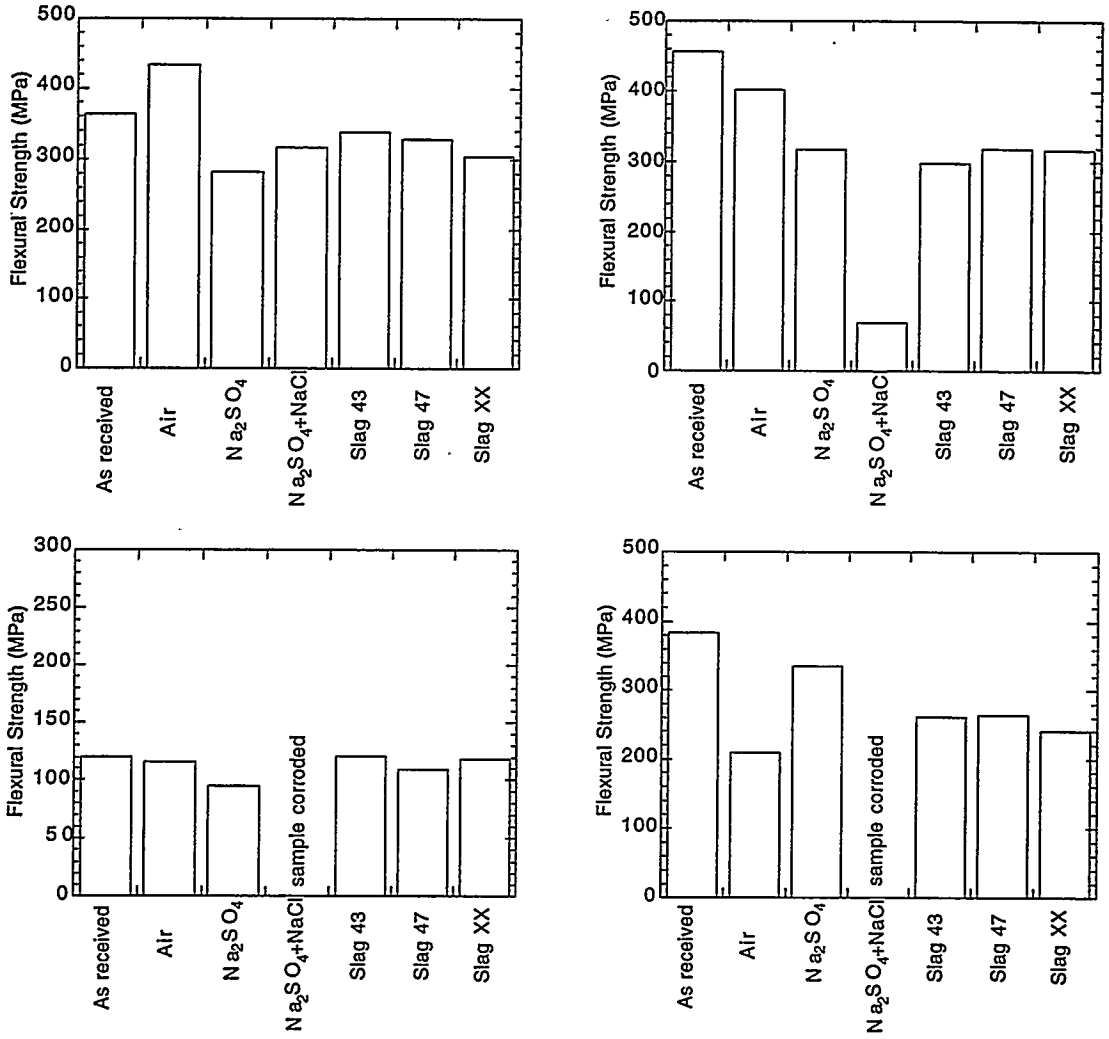

Fig. 5. Effect of exposure 200 h exposure at 1200°C on flexural strength for Hexoloy SA (top left), NT 230 (top right), SiC in Si matrix (bottom left), and SiC(f) in SiC matrix (bottom right)

specimens. Because of the high density of this material, influence of corrosive attack on this material may require longer exposure times or higher temperatures. The NT 230 exhibited fairly good strength after air exposure but had a significant loss in strength after exposure to salt that contained NaCl. On the other hand, the presence of slags at 1200°C had very little effect on the strength of the NT 230. The SiC in Si matrix was fairly porous and the sample became fully corroded in the presence of the salt containing NaCl but did not exhibit significant loss in strength in the presence of other deposits. The composite SiC(f) in SiC matrix also was subjected to accelerated corrosion in the presence of salt containing NaCl but behaved fairly well in other environments.

Figure 6 shows the absorbed energy per unit area for the four materials after 200 h exposure at 1200°C to different environments. The absorbed energy values for Hexoloy SA are 0.15-0.20 J/cm^2 after exposure in air and slag environments. The low value, which is an average of three tests conducted at

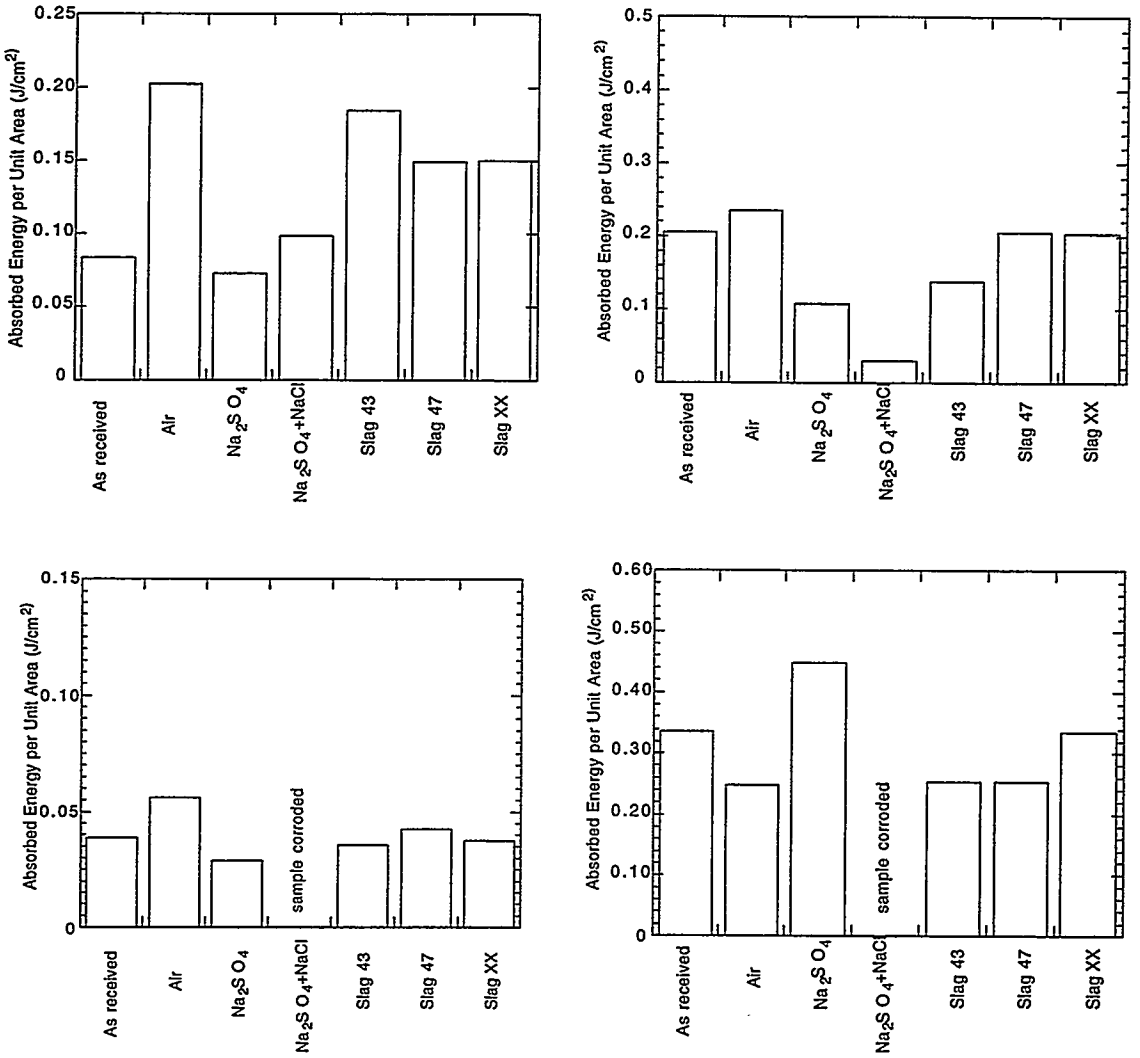

Fig. 6. Effect of exposure 200 h exposure at 1200°C on absorbed energy per unit area for Hexoloy SA (top left), NT 230 (top right), SiC in Si matrix (bottom left), and SiC(f) in SiC matrix (bottom right)

1200°C, for the as-received material cannot be explained at present. The lower values for the salt-exposed specimens may indicate some intergranular prenetration of salt, which was not obvious from SEM analysis of specimen cross sections. Absorbed energy values for the as-received, air-exposed, and slag-exposed specimens of NT 230 were comparable, indicating that these environments are benign from the corrosion standpoint after 200 h of exposure at 1200°C. The slat-exposed specimens showed lower absorbed energy values similar to those of Hexoloy SA. Specimens of SiC in Si matrix had inherently a low value for energy to fracture and were not significantly affected after exposure in air and slag environments. The presence of sulfate salt seems to lower the fracture energy. The composite material SiC(f) in SiC matrix had the highest value (0.25-0.40 J/cm^2) for fracture energy among the four materials testsed. The results also indicate that the salt environments have degrading effects on the strength properties of these materials but the presence of slag

(simulating either Eastern or Western U.S. coals) had a minimal effect at 1200°C in 200 h exposures.

SUMMARY

Several ceramic materials have been examined to evaluate performance after exxposure to dry air, salt environments that contained Na_2SO_4 or 75 wt.% Na_2SO_4-25 wt.% NaCl mixture, and to three different coal slags that simulate slags obtained fro combustion of coals from Eastern and Western U.S. The results showed that the materials exposed to an air environment undergo passive oxidation of SiC to SiO_2. Exposure of these materials to salt environments can lead to catastrophic corrosion, especially if the condensed salt is high in sodium activity, which can lead to low-melting corrosion products. On the other hand, exposure of the materials to slags obtained from typical coal ash had very little effect on the corrosion performance of the materials, especially at 1200°C under which the reactions do not involve formation of liquid corrosion products. Four-point bend tests conducted on several of the materials after exposure to dry air, salt, and slag environments indicated that sodium salts (both sulfates and chlorides) have the most degrading effect on properties, while exposure to air and slag environments had minimal effect on properties at 1200°C.

ACKNOWLEDGMENTS

The authors thank the ceramics manufacturers for supplying specimen materials. D. L. Rink assisted in the corrosion and four-point bend tests and microstructural analysis of exposed specimens.

REFERENCES

1. L. A. Ruth, "Combustion 2000," PETC Review, Issue 4, p. 4, Fall 1991.

2. K. Natesan, M. Yanez-Herrero, and C. Fornasieri, "Corrosion Performance of Materials for Advanced Combustion Systems," Argonne National Laboratory Report ANL/FE-93/1, Dec. 1993.

3. K. Natesan, M. Freeman, and M. Mathur, "Corrosion Performance of Materials for Advanced Combustion Systems," Proc. 9th Annual Conf. on Fossil Energy Materials, CONF-9505204, ORNL/FMP-95/1, 1995.

4. S. C. Singhal, "Thermodynamic Analysis of the High-Temperature Stability of Silicon Nitride and Silicon Carbide," Cermamurgia Intl., 2(3) (1976) 123-130.

INTERACTION OF LOW-EXPANSION NZP CERAMICS WITH Na_2SO_4 AT 1000°C

W. Y. Lee, K. M. Cooley, D. P. Stinton, and D. L. Joslin

Oak Ridge National Laboratory
P. O. Box 2008
Oak Ridge, TN 37831-6063

ABSTRACT

The interaction between several low-expansion NZP materials and Na_2SO_4 at 1000°C in pure O_2 was studied. $Ba_{1.25}Zr_4P_{5.5}Si_{0.5}O_{24}$ experienced extensive cracking and delamination upon reaction with Na_2SO_4. On the other hand, $Ca_{0.5}Sr_{0.5}Zr_4P_6O_{24}$ remained intact in terms of visual appearance, and had no significant weight loss or gain. However, the ion exchange between Na^+ ions and Ca^{+2} ions was observed to be sufficiently rapid to allow the penetration of the Na^+ ions into the test specimens in 100h. The segregation of Ca to the specimen surface was observed due to the ion exchange. $Ca_{0.6}Mg_{0.4}Zr_4P_6O_{24}$ was also tested, but its stability could not properly be assessed because the as-received specimens contained a significant amount of $MgZr_4P_6O_{24}$ as an impurity phase.

INTRODUCTION

A new class of ceramic materials with low and tailorable thermal expansion characteristics has been developed for potential use in a variety of high temperature applications [1-3]. They are commonly referred to as NZP and named after the parent composition ($NaZr_2P_3O_{12}$) which was discovered to exhibit high cationic conductivity and low-expansion characteristics. Although the thermal expansion behavior of most NZP materials is generally anisotropic, some NZP compositions such as $Ba_{1+x}Zr_4P_{6-2x}Si_{2x}O_{24}$ (where $0 < x < 1$), $Ca_{1-x}Sr_xZr_4P_6O_{24}$, and $Ca_{1-x}Mg_xZr_4P_6O_{24}$ can be tailored to obtain isotropic expansion characteristics [2-4]. The Young's modulus of these NZP materials is reported to be rather low for a ceramic (~70 GPa) [3]. Another interesting property of these materials is their low thermal conductivity (~1 W/mK for slip-cast materials [3]) which is essentially as low as that of air plasma sprayed yttria stabilized zirconia coatings currently used as thermal barrier coatings in advanced gas turbines.

In addition to their potential use as bulk materials, the NZP ceramics could also be considered for thermal barrier and corrosion resistant coating applications. For example, Si-based materials such as Si_3N_4 and SiC are known to be susceptible to major strength reduction

in certain corrosive environments containing condensible deposits such as Na_2SO and Na_2CO_3 [5,6]. Thus, the need for developing a coating system which protects the surface of the Si-based materials from the corrosive environments has been recognized [7,8]. Unfortunately, progress in developing such a coating system has been limited because of many challenging thermochemical and thermomechanical requirements. From a thermomechanical point of view, the use of the NZP materials as protective coatings for Si-based ceramics may be advantageous because of the low thermal expansion and compliance of the NZP materials relative to most Si-based materials. However, the thermochemical stability of these complex material systems has not been explored except for the recent work of Li et al. [9]. They prepared a thin $Ca_{0.6}Mg_{0.4}Zr_4P_6O_{24}$ coating on Si_3N_4 and SiC substrates using a sol-gel method. The coated substrates were exposed to several environments containing Na_2CO_3 at 1000°C for 50h, and yet no major change in the flexural strength of the Si_3N_4 substrates was observed. This suggested that the coating was effective in protecting the Si_3N_4 substrates from the corrosive environments. In order to further assess the potential of NZP materials for use as corrosion-resistant coatings, the present study is aimed at examining the intrinsic stability of several NZP bulk forms in a Na_2SO_4-containing atmosphere.

EXPERIMENTAL

Three slip-cast NZP materials were evaluated: $Ba_{1.25}Zr_4P_{5.5}Si_{0.5}O_{24}$ (BS25, x=0.25, LoTEC, Salt Lake City, UT), $Ca_{0.6}Mg_{0.4}Zr_4P_6O_{24}$ (CM40, x=0.4, Golden Technologies, Golden, CO), and $Ca_{0.5}Sr_{0.5}Zr_4P_6O_{24}$ (CS50, x=0.5, LoTEC). These particular compositions were chosen because they possess high strength while exhibiting low thermal expansion anisotropy and hysterisis [2,3]. Two specimens (1 cm x 0.4 cm x 0.3 cm) were tested for each material. The specimens were typically loaded with about 5 to 10 mg/cm^2 of Na_2SO_4 using a procedure described elsewhere [8]. Prior to applying the layer of Na_2SO_4, the specimens were cleaned with distilled water, methanol, and acetone. The Na_2SO_4 loaded specimens were placed on an Al_2O_3 holder and exposed for 100h to a flowing oxygen environment (200 cm^3/min) at 101 kPa in a quartz tube heated to 1000°C using an electric resistance furnace. It is noted that Na_2SO_4 has a relatively low rate of evaporation at these temperature and pressure conditions (~ 0.016 Mg/cm^2/h) [10]. Thus, the premature loss of Na_2SO_4 due to evaporation was not expected to occur for the test duration used in this study. Each NZP composition was

tested in separate batches to avoid any sample cross-contamination. A Scintag V x-ray diffractometer (XRD) and a JEOL Superprobe 733 electron microprobe analyzer (EMPA) were used for characterization. Both as-received and reacted specimens were mounted in epoxy and polished using kerosene as a lubricant to examine the formation of any reaction products and resulting surface microstructures. One of the two specimens exposed to the reaction treatment was washed in warm water using an ultrasonic bath to remove any water-soluble or weakly bonded phase(s) from the reacted surface.

RESULTS

Table I shows that BS25 lost significant weight after reacting with Na_2SO_4 for 100h. In reference to the initial weight before Na_2SO_4 loading, Sample # BS25-1 lost 33.7 mg (or 27.2 mg/cm^2) after the reaction and washing steps. It was visually evident that both unwashed and washed BS25 specimens were structurally disintegrated. Severe surface recession due to cracking and delamination were observed particularly along the corners and edges of the specimens' top surface. The formation of $NaZr_2P_3O_{12}$ was detected by XRD as a minor phase in both unwashed and washed specimens. In addition, the BS25 diffraction peaks were observed to be somewhat randomly shifted by small amounts as a result of the reaction step.

Table I

Weight (g) of low-expansion ceramic specimens (dimensions; 1 cm x 0.4 cm x 0.3 cm) measured after Na_2SO_4 loading, reaction, and washing in warm water. Net weight change (Δm) = Final weight after washing - Initial sample weight. CM40 specimens could not be washed because they were fractured into pieces after reaction.

Sample	Initial	Na_2SO_4	Reacted	Washed	Δm
BS25-1	0.3745	0.3859	0.3644	0.3414	-0.0337
BS25-2	0.3519	0.3652	0.3087	-	-
CM40-1	0.3875	0.3945	0.3725	-	-
CM40-2	0.3774	0.3879	-	-	-
CS50-1	0.3151	0.3203	0.3162	0.3145	-0.0006
CS50-2	0.3225	0.3308	0.3242	-	-

CM40 specimens also significantly cracked, and were actually fractured into several pieces after reacting with Na_2SO_4. However, it appeared from the XRD analysis that the as-received CM40 specimens contained a significant amount of $MgZr_4P_6O_{24}$ as an impurity phase. The XRD pattern of the reacted specimens indicated the formation of $NaZr_2P_3O_{12}$ and/or $CaZr_4P_6O_{24}$ along with an unknown phase(s). Note that $NaZr_2P_3O_{12}$ and $CaZr_4P_6O_{24}$ are difficult to distinguish by XRD because of their similar lattice parameters.

Unlike the BS25 and CM40 samples, the weight of the CS50 specimens decreased only slightly after the reaction and washing steps (0.5 mg/cm^2 for Sample# CS50-1 in Table I). No significant recession due to cracking and delamination was visually detected. However, as shown in Figure 1, an EMPA analysis of the polished cross-section of the reacted specimen (Sample # CS50-1) shows that the ion exchange between Na^+ ions from Na_2SO_4 and Ca^{+2} ions from CS50 was fairly extensive during the 100h reaction period. The presence of Na was observed throughout the entire cross-section of the reacted sample. In contrast, as-received CS50 samples did not contain any Na detectable to the EMPA technique. The segregation of Ca toward the surface was observed as shown in Figure 1. It appeared that the Ca-enriched surface layer was weak since it was somewhat damaged by polishing as evidenced by some delamination in this region. There was no apparent change in the Ca-enriched surface layer after washing. The presence of sulfur was not detected by the EMPA technique in the reacted and washed samples. In comparing the XRD patterns of the as-received, corroded, and washed samples, the appearance of some new, unindexable diffraction peaks was observed after the reaction step. The new peaks did not disappear after the specimen was washed.

DISCUSSION

The experimental observations suggested that the BS25 specimens became structurally as well as chemically unstable when reacted with Na_2SO_4 at 1000°C for 100h in O_2. The formation of the $NaZr_2P_3O_{12}$ phase was observed as a reaction product from the BS25 samples. The $NaZr_2P_3O_{12}$ phase is known to exhibit highly anisotropic thermal expansion behavior, and consequently microcracks extensively. Also, the formation of $NaZr_2P_3O_{12}$ can induce undesired volume changes since the unit-cell volume of $NaZr_2P_3O_{12}$ (1527.83 $Å^3$) is smaller

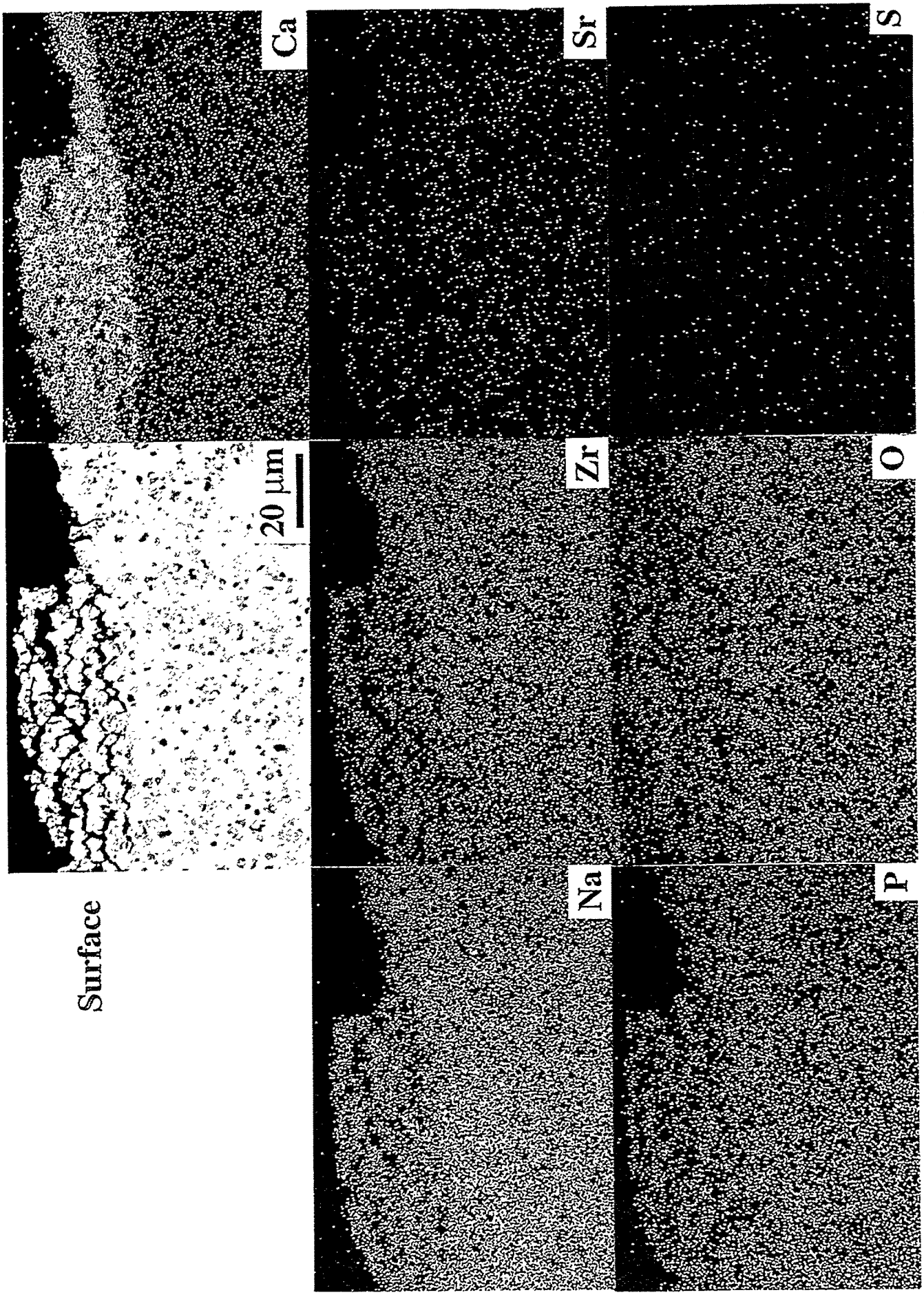

Figure 1. Backscattered image and x-ray elemental maps of CS50 after reaction with Na_2SO_4 at 1000°C for 100 h in pure O_2.

than that of BS25 (1559.94 $Å^3$ [11]). Therefore, the formation of the $NaZr_2P_3O_{12}$ phase appears to be responsible for the observed cracking and delamination of the reacted BS25 samples.

The stability of CM40 with respect to Na_2SO_4 could not be assessed from this study, because the starting material contained a significant amount of $MgZr_4P_6O_{24}$ as an impurity phase. Nevertheless, the observed cracking and delamination of these specimens after reaction with Na_2SO_4 could be explained by the relatively large volume change anticipated from the transition of $MgZr_4P_6O_{24}$ to $NaZr_2P_3O_{12}$ and/or $CaZr_4P_6O_{24}$. The unit-cell volume of monoclinic $MgZr_4P_6O_{24}$ (977.52 $Å^3$) is considerably smaller than that of rhomobehedral $NaZr_2P_3O_{12}$ and $CaZr_4P_6O_{24}$ (1527.83 and 1516.01 $Å^3$, respectively). Because of the $MgZr_4P_6O_{24}$ impurity phase, the results from this study could not directly be compared to those reported by Li et al. [9]. As mentioned earlier, Si_3N_4 substrates coated with a sol-gel CM40 coating did not show any strength degradation after exposure to several corrosive environments containing Na_2CO_3 at 1000°C for 50h. In future work, pure CM40 specimens are needed to determine their intrinsic stability in the corrosive environments.

In terms of visual appearance and weight loss, the CS50 samples appreared to have remained relatively intact after reaction with Na_2SO_4. However, at a microscopic level, the EMPA results clearly indicated that the ion exchange between the Na^+ and Ca^{+2} ions was sufficiently rapid for the Na^+ ions to penetrate the entire CS50 specimens during the 100h exposure. The presence of sulfur was not detected at least within the sensitivity of the EMPA technique. Therefore, it seems that the CS50 material promotes the dissociation of Na_2SO_4 while releasing SO_3 and/or SO_2 as gaseous byproducts. The significance of these observations relative to the potential of the CS50 material as a corrosion resistant coating for Si-based ceramics is not yet clear. A further study is needed to assess the effects of Na penetration through a CS50 coating structure in protecting Si-based substrates. Also, the thermochemical compatibility between the CS50 and Si-based ceramics must be addressed.

ACKNOWLEDGMENTS

The authors acknowledge their gratitude to Santosh Limaye for providing the BS25 and CS50 samples, Tom Geer for metallography, and Y. W. Bae for x-ray diffraction.

REFERENCES

1. C.-Y. Huang, D.K. Agrawal, H.A. McKinstry, and S.Y. Limaye, "Synthesis and Thermal Expansion Behavior of $Ba_{1+x}Zr_4P_{6-2x}Si_{2x}O_{24}$ and $Sr_{1+x}Zr_4P_{6-2x}Si_{2x}O_{24}$ Systems," J. Mater. Res., 9, 2005 (1994).

2. D.A. Hirschfeld, S.M. VanAken, T.K. Li, Y.P. Yang, and J.J. Brown, "Development of Ultra-Low-Expansion Ceramics: Synthesis, Thermal Expansion, and Thermal Conductivity of $(Ca_{1-x},Mg_x)Zr_4(PO_4)_6$," pp. 239-244 in the Proceedings of the Annual Automotive Technology Development Contractors' Meeting, Dearbon, MI, October 22-25, 1990. Published by the Society of Automotive Engineers, Inc., Warrendale, PA, 1991.

3. S.Y. Limaye and R. Nageswaran, "Development of NZP Ceramic Based "Cast-In-Place" Diesel Engine Port Liners," Final Report, LoTEC, Inc., West Valley City, UT, November 1994.

4. T.B. Jackson, S.Y. Limaye, and W.D. Porter, "The Effects of Thermal Cycling on the Physical and Mechanical Properties of [NZP] Ceramics," pp. 63-80 in Ceramics Transactions Vol. 52; Low-Expansion Materials. Edited by D.P. Stinton and S.Y. Limaye, The American Ceramic Society, Westerville, OH, 1995.

5. N.S. Jacobson, "Corrosion of Silicon-Based Ceramics in Combustion Environments," J. Am. Ceram. Soc., 76, 3 (1993).

6. Components to Erosion and Hot Corrosion/Oxidation Attack," p. 36-1 in Proceedings of Advisory Group for Aerospace and Research & Development Symposium on Erosion, Corrosion, and Foreign Object Damage Effects in Gas Turbines, Printed by Canada Communication Group, Qu bec, Canada, November 1994.

7. K.N. Lee, N.S. Jacobson, and R.A. Miller, "Refractory Oxide Coatings on SiC Ceramics," MRS Bulletin, 35, (October 1994).

8. W.Y. Lee, Y.W. Bae, and D.P. Stinton, "Na_2SO_4 Induced Corrosion of Si_3N_4 Coated with Chemically Vapor Deposited Ta_2SO_5," J. Am. Ceram. Soc., 78, 1927 (1995).

9. T.K. Li, D.A. Hirschfeld, and J.J. Brown, "Thin Film Coatings of $(CA_{1-x},Mg_x)Zr_4(PO_4)_6$ on Si_3N_4 and SiC," J. Mater. Res., 9, 2014 (1994).

10. N.S. Jacobson and D.S. Fox, "Molten-Salt Corrosion of Silicon Nitride: II, Sodium Sulfate," J. Am. Ceram. Soc., 71, 139 (1988).

11. S. Shanmugham, D.P. Stinton, O.B. Calvin, C.R. Hubbard, and S.Y. Limaye, "Synthesis and Cell Refinement of $Ba_{0.5+x/2}Zr_2P_{3-x}Si_xO_{12}$ with x=0.25 and x=0.375," J. Mater. Sci. Lett., 13, 1326 (1994).

SYNTHESIS OF MULLITE COATINGS BY CHEMICAL VAPOR DEPOSITION

Rao P. Mulpuri, Michael Auger, Vinod K. Sarin

Boston University
Department of Manufacturing Engineering
Boston, MA 02215

ABSTRACT

Formation of mullite on ceramic substrates via chemical vapor deposition was investigated. Mullite is a solid solution of Al_2O_3 and SiO_2 with a composition of $3Al_2O_3 \cdot 2SiO_2$. Thermodynamic calculations performed on the $AlCl_3$-$SiCl_4$-CO_2-H_2 system were used to construct equilibrium CVD phase diagrams. With the aid of these diagrams and consideration of kinetic rate limiting factors, initial process parameters were determined. Through process optimization, crystalline CVD mullite coatings have been successfully grown on SiC and Si_3N_4 substrates. Results from the thermodynamic analysis, process optimization, and effect of various process parameters on deposition rate and coating morphology are discussed.

INTRODUCTION

Silicon-based ceramics such as Si_3N_4 and SiC are currently the leading candidate materials for high temperature applications due to their unique combination of high strength and thermal conductivity, low thermal expansion, good high temperature stability and oxidation resistance. However, their susceptibility to high temperature corrosion and damage due to contact stress considerably limit their utilization. For example, corrosion can occur at elevated temperatures as a result of the combined effect of the oxygen plus gaseous, condensed, or particulate impurities induced via the gas stream in a turbine engine. [1] In addition, contact stress damage at ceramic/ceramic

interfaces has been projected as a major failure mode for ceramic components in advanced heat engines. [2] It has been established that the application of a coating on silicon based substrates is an effective technique to minimize or overcome these problems. [3,4] Several coating systems have been developed, but none to date have been able to meet all the requirements due to the severity of these applications. [5,6] Mullite ($3Al_2O_3 \cdot 2SiO_2$) due to its unique properties such as thermal expansion match with Si_3N_4 and SiC, stability, and significantly superior corrosion resistance at high temperatures, [7,8] is considered a prime candidate coating material.

Mullite is a solid solution of Al_2O_3 and SiO_2 and is the only stable crystalline compound in the Al_2O_3-SiO_2 system. Although it is popularly quoted with an Al_2O_3:SiO_2 ratio of 3:2, mullite is known to have a range of solid solubilities. After several years of research, there are still controversies regarding the melting behavior and the solid-solution range of mullite. However, it has been observed that the solid solubility is dependent on the method of synthesis. Attempts to grow mullite coatings by various processing techniques have met with limited success. [4] Deposition of plasma sprayed mullite coatings was reported, [9] however the coatings exhibited problems such as non-uniformity and microcracks which are characteristic of the plasma spray process. To overcome these deficiencies, formation of mullite via CVD has been investigated. The CVD process generally results in dense coatings that can be synthesized well below the melting or sintering temperatures of the material, with the possibility of microstructural and morphological optimization through variation in process parameters. Although the deposition of CVD Al_2O_3 and SiO_2 is now well established, [10-14] to our knowledge mullite coatings have never before been grown from the vapor phase.

THERMODYNAMIC ANALYSIS

Equilibrium thermodynamic analysis was performed on the $AlCl_3$-$SiCl_4$-CO_2-H_2 system in order to establish equilibrium reaction products at various operating conditions. It has been common practice to use thermodynamic analysis to predict the possible outcome of a CVD reaction. [15-22] A computer program [23] utilizing minimization of Gibbs free energy was used to perform the thermodynamic analysis. This was based on

earlier work to calculate the composition and heat condition of an equilibrium mixture. [24] The results of several calculations at each set of process conditions were presented in the form of binary and ternary CVD phase diagrams. Chemical equilibrium is rarely achieved under most CVD flow conditions. [25] Therefore, results from these diagrams can only be used to establish guidelines in the form of trends rather than to predict the exact phases that would be actually present. Most importantly, thermodynamic analysis did not include the rate-controlling factors in the CVD process such as reaction kinetics, mass transport of the gaseous species, and depletion of the reactant gases. Thus, an actual CVD experiment does not necessarily conform with predictions of the thermodynamic analysis. However, such phase diagrams can be used to project the influence of process variables such as temperature, pressure, and inlet gas concentrations on the phase assemblage stoichiometry of the deposit, the equilibrium deposition efficiency, and the concentration of the molecular species in the exhaust gas. The thermodynamic equilibrium state of the CVD system can be calculated for (i) partial pressures of all the gaseous species, (ii) the identification of the condensed phase, (iii) equilibrium deposition rates possible and (iv) their theoretical efficiencies. Such calculations provide limiting criteria and aid in establishing rate-limiting gaseous species. The reliability of these calculations is, of course, dependent on the availability and accuracy of thermochemical data as well as identification of all the critical vapor and condensed phases. Information from such phase diagrams can be used to help determine the range of input conditions which would produce mullite and other compounds at equilibrium.

The reaction yielding mullite from $AlCl_3$ and $SiCl_4$ is hypothesized to be as follows:

$$6AlCl_3 + 2SiCl_4 + 13CO_2 + 13H_2 \longrightarrow 3Al_2O_3{\bullet}2SiO_2 + 13CO + 26HCl \quad \text{--- (1)}$$

For the purpose of the equilibrium calculations, it was assumed that mullite is a line compound, and of $3Al_2O_3{:}2SiO_2$ composition. The calculations were based on thermodynamic data obtained from Ref [26]. Several calculations were performed on the $AlCl_3$-$SiCl_4$-CO_2-H_2 system at different process parameters at each set of deposition conditions. Figure 1 shows a sample ternary CVD phase diagram of $AlCl_3$-$SiCl_4$-CO_2-H_2 system at 1000 °C and 75 torr. This diagram represents, for a set of reaction conditions and input reactant concentrations, all the possible phases that would be present during equilibrium conditions equilibrium.

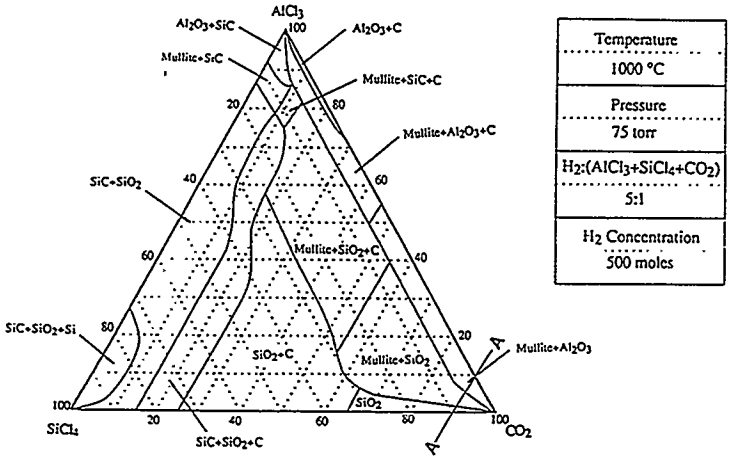

Figure 1: CVD phase diagram of $AlCl_3$-$SiCl_4$-CO_2-H_2 system at 1000°C and 75torr

Details of an extensive thermodynamic analysis were discussed in an earlier publication. [27] It was concluded that low concentrations of the chlorides need to be used in order to obtain high deposition efficiency, and carbon-free deposits. It was also found that there were no underlying benefits to using bromides and fluorides as alternative halide sources.

KINETIC CONSIDERATIONS

As mentioned earlier, an understanding of thermodynamics alone is not sufficient to establish the CVD process parameters. Reaction kinetic limitations to a great extent have a major effect on the deposition characteristics. The relative importance of thermodynamic and kinetic considerations depends on the particular system of interest and the specific process conditions. Since no data was available to predict the mechanism of formation of mullite from $AlCl_3$ and $SiCl_4$, it was assumed that the CVD formation of mullite follows the same reaction path associated with the formation of Al_2O_3 from $AlCl_3$. It is well established that the formation of Al_2O_3 necessitates the formation of H_2O through the water-gas-shift reaction, thus making it the rate-limiting step. It is also important to note that the formation of SiO_2 from $SiCl_4$ does not require an intermediate reaction such as H_2O formation to occur. Keeping this in mind, the

assumed reaction steps during the formation of mullite can be expressed using the following set of intermediate reactions:

$$2Al + 3Cl_2 \longrightarrow 2AlCl_3 \quad \text{-------- (2)}$$

$$CO_2 + H_2 \longrightarrow H_2O + CO \quad \text{-------- (3)}$$

$$6AlCl_3 + 2SiCl_4 + 13H_2O \longrightarrow 3Al_2O_3{\bullet}2SiO_2 + 26HCl \quad \text{-------- (4)}$$

Initial process parameters were chosen based on the information obtained through equilibrium thermodynamic analysis, and consideration of kinetic factors such as the influence on the water-gas-shift reaction. At this stage, it was unclear how the water-gas-shift reaction influenced the formation of CVD mullite.

EXPERIMENTAL METHODS

A CVD unit consisting of a vertical hot wall reactor with a resistively heated furnace was used for the experiments. Polished bars of 3x4x20 mm size of monolithic SiC and Si_3N_4 were used as substrates. In general, low chloride concentrations were chosen for experimentation. $AlCl_3$ was formed in-situ by flowing Cl_2 with Ar carrier gas through densely packed Al wire cuttings maintained at a constant temperature. $SiCl_4$ was evaporated from liquid stage at room temperature. $AlCl_3$ and $SiCl_4$ were mixed in appropriate ratios prior to entering the CVD reactor. H_2 and CO_2 were used via the water-gas-shift reaction in order to form H_2O in-situ in the CVD reactor. There was always excess hydrogen present in the system to ensure all the chlorides were properly reduced to HCl before leaving the reactor.

RESULTS AND DISCUSSION

A unique CVD process was developed for deposition of crystalline mullite coatings on silicon based substrates. [28] Figure 2 shows the surface morphology and cross-section of a typical mullite coating deposited on Si_3N_4 at 950 °C and 75 torr for 2

hours. As is evident, the coating was dense, uniform in thickness (approximately 6 μm), and had a fine grained (around 2 μm) equiaxed structure. X-ray and electron diffraction analyses confirmed that the only crystalline phase present in the coating was mullite. To further characterize the coating structure on a microscopic level, TEM was performed. A more detailed microstructural analysis clearly shows that the coating starts with very fine grains and grows into larger grains as the growth process continues. Further characterization through energy dispersive spectroscopy shows that the Al/Si ratio gradually increased as the coating grew. Figure 3 shows a transmission electron micrograph and a typical change in the Al/Si ratio of the coating on SiC.

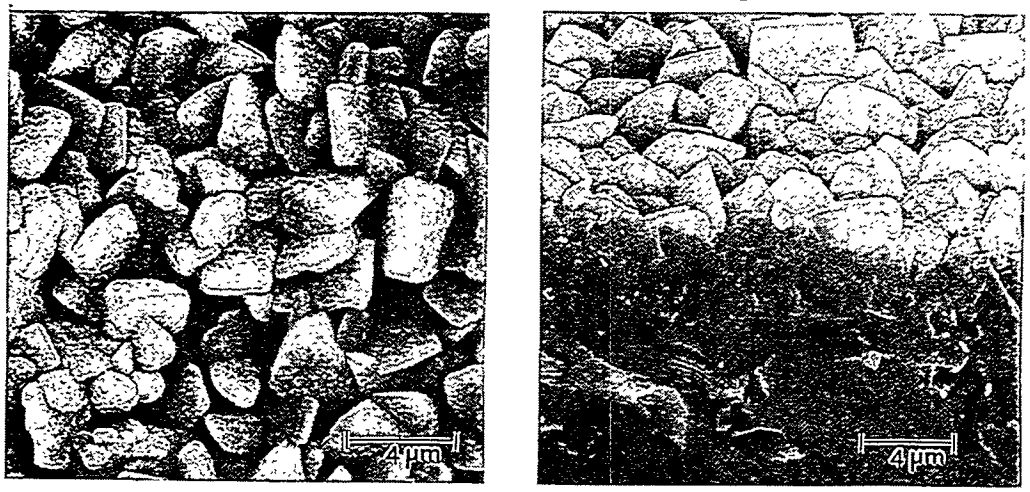

Figure 2: Scanning Micrograph of mullite coating on SiC a) surface, b) cross-section

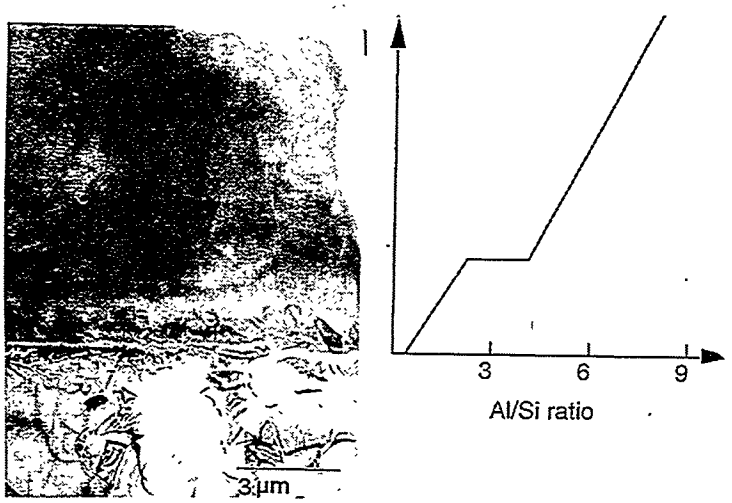

Figure 3: Transmission Electron Micrograph of mullite on SiC, b) change in Al/Si ratio throughout the coating

Effect of Temperature

The effect of temperature on the deposition rate is shown in Figure 4. The mullite deposition rate decreased from 800 °C to 850 °C and then increased beyond that. Figure 5 shows the Arrhenius plot corresponding to an activation energy of 7.4 kcal/mol. Although this activation energy is characteristic of a mass-transport limited process, the result should be interpreted with caution since a variation in Al/Si ratio was observed in the coating. In addition, the extent of crystallinity was also a variable, making it even more complicated. Figure 6 shows the coating surface morphology at various process temperatures. At 800 °C, the coating has a globular morphology and is amorphous according to X-ray analysis. This is in agreement with the thermodynamic analysis that mullite is not predicted to form at 800 °C. At 850 °C, the coating remained globular with small crystallite formation. X-ray diffraction also shows a small amount of mullite detected. As the temperature was increased beyond 1000 °C, large clusters of crystals were formed resulting in cracking of the coating.

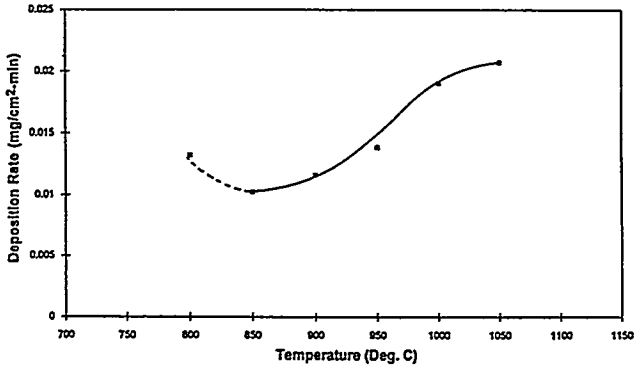

Figure 4: Effect of Temperature on Deposition Rate

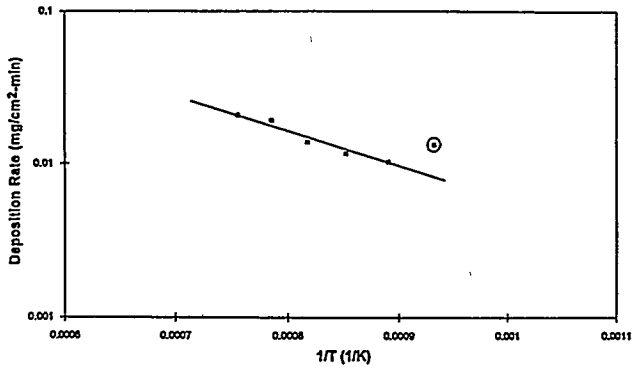

Figure 5: Arrhenius plot of mullite deposition at 75torr

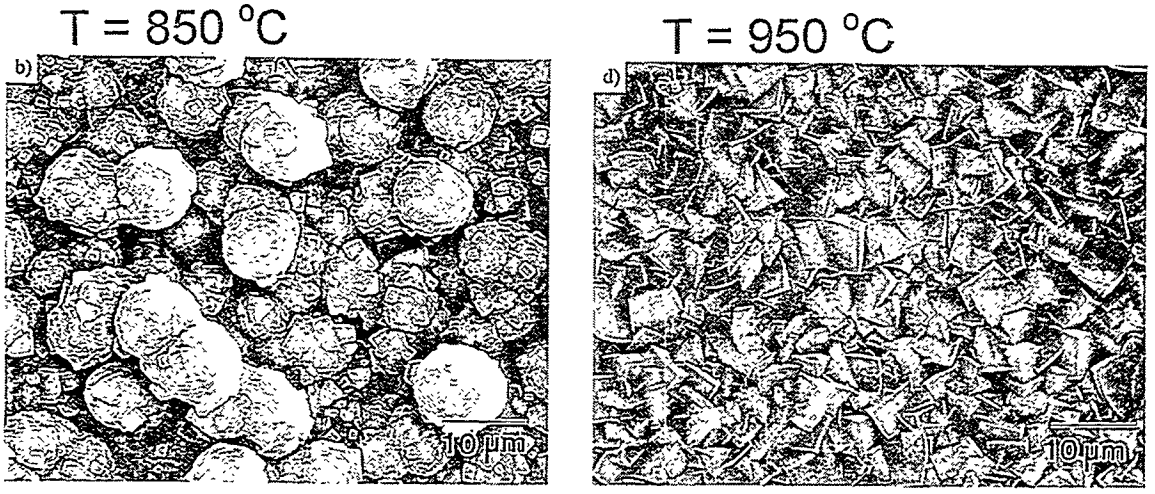

Figure 6: Surface morphology of mullite grown at various temperatures

Effect of Total System Pressure

The effect of total system pressure on deposition rate is shown in Figure 7. The deposition rate increased almost linearly at low system pressures; however, with a further increase in the system pressure, the rate of increase was reduced, with a subsequent reduction in the deposition rate. This effect can be attributed to the depletion of reactants with increase in pressure due to the hot wall configuration of the system. Figure 8 shows the variation in coating surface morphology with total system pressure. The grain size increased with an increase in the pressure to a certain extent. The grain size at the 200 torr condition was actually smaller than that at the 150 torr condition. In addition, it was observed that the coating was porous at higher pressures. This variation is again, believed to be a result of the depletion of reactants.

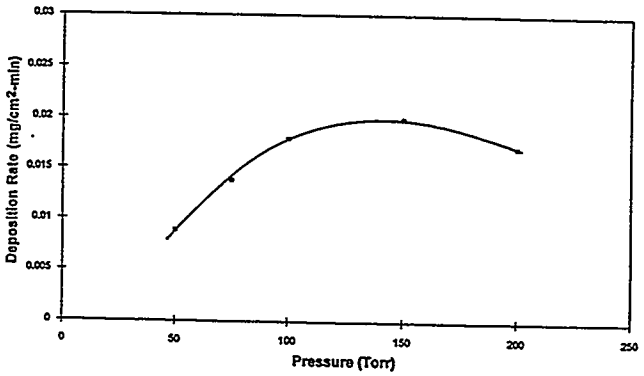

Figure 7: Effect of total system pressure on mullite deposition rate at 950°C

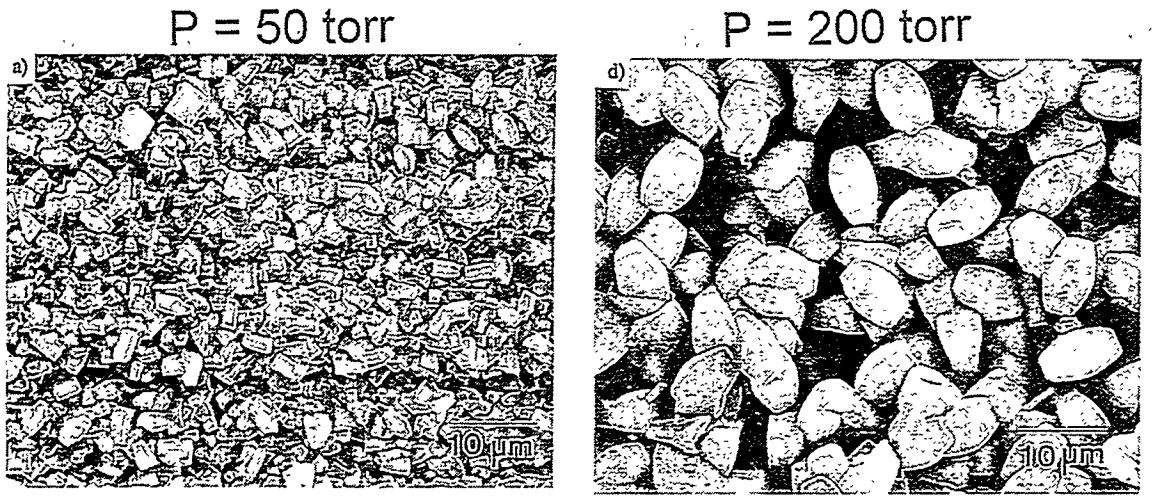

Figure 8: Surface morphology variation of mullite with change in total system pressure

Effect of Input Gas Stoichiometry

The effect of the input gas stoichiometry in the form of Al/Si ratio was investigated. The Al/Si ratio was varied from 0 to 4. Figure 9 shows the variation in deposition rate with respect to Al/Si ratio in the input gas composition. At Al/Si ratio of zero (pure SiO_2 deposit), a high growth rate was observed. As the Al/Si ratio was increased, the deposition rate decreased rapidly to a certain level and then increased. This implies that the addition of a small amount of Al species to $SiCl_4$ in the formation of mullite reduces the deposition rate considerably. This also points to a possible shift in the deposition mechanism with the addition of Al species. There is insufficient data available at this stage to understand this phenomenon completely. Figure 10 shows the variation in coating surface morphology with the Al/Si ratio. The size of the mullite crystals increased with an increase in the Al/Si ratio in the input gas composition. This variation corresponds to the finding that the grain size increased with the coating growth along with an increase in Al/Si ratio in the coating.

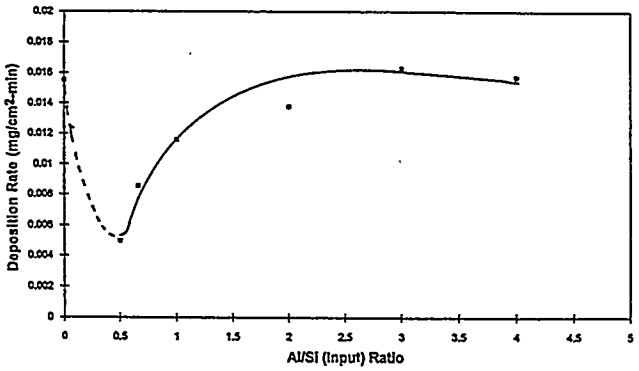

Figure 9: Variation in deposition rate with respect to input Al/Si ratio at 950°C, 75torr

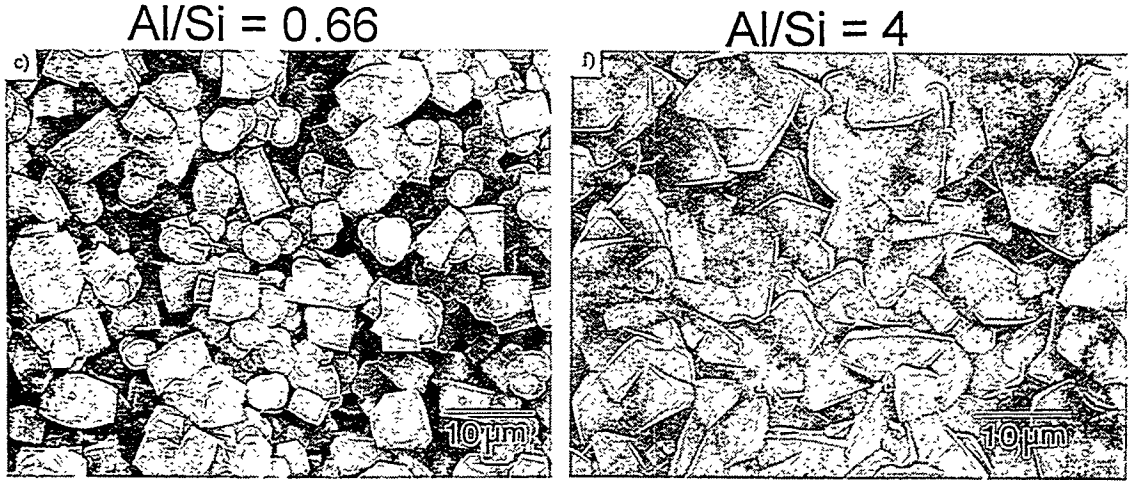

Figure 10: Surface morphology variation with respect to Al/Si input ratio

Comparison of the growth rates at various levels in the reactor and the reactant depletion effects suggest that the formation of mullite does not require the formation of H_2O through the water-gas-shift reaction. Instead, oxygen from CO_2 is utilized for the formation of the oxide(s). Reactant depletion effects in the hot wall system make it difficult to separate the effect of parameters such as temperature and pressure independently. Further experimentation is necessary in order to understand the exact mechanisms involved.

Results from the initial corrosion resistance evaluations at Oak Ridge National Laboratory look very promising. Mullite coated Si_3N_4 samples loaded with Na_2SO_4 were heated to temperatures over 1000 °C in an oxygen environment. Electron microprobe analysis of the treated samples as well as x-ray diffraction analysis before and after the corrosion testing show that there were no reactions and formation of corrosion products between mullite and Na_2SO_4.

CONCLUSIONS

Equilibrium thermodynamic analysis was performed on the $AlCl_3$-$SiCl_4$-CO_2-H_2 system which pointed out that low concentrations of the chlorides were necessary in order to obtain high deposition efficiency, and carbon-free deposits. Information from the phase diagrams and kinetic rate-limiting considerations was effectively used to identify the initial process parameters for the growth of mullite. Based on these results, a new process for depositing crystalline mullite coatings on Si_3N_4 and SiC based substrates was developed. The coatings were dense, and increased in Al content from the substrate to the surface of the coating. Preliminary testing projects mullite as a promising coating material for corrosion protection of SiC and Si_3N_4.

ACKNOWLEDGMENT

The authors wish to acknowledge Mr. D.P. Stinton of Oak Ridge National Laboratory (ORNL) for his helpful insights throughout this research. The authors also wish to acknowledge the help from Mr. D. Doppalapudi, and Dr. S.N. Basu with the TEM analysis, and Dr. W.Y. Lee of ORNL with the corrosion resistance evaluation. Research sponsored by the U.S. Department of Energy, Assistant Secretary for Energy Efficiency and Renewable Energy, Office of Transportation Technologies, as part of the Ceramic Technology Project of the Propulsion System Materials Program, and Fossil Energy AR&TD Materials Program under contract numbers DE-AC05-84OR21400 and SC-19X-SS110C with Martin Marietta Energy Systems, Inc.

REFERENCES

1. N.S. Jacobson, J. Am. Ceram. Soc., 76 [1] 3-28 (1993)

2. D.W. Richerson, W.D. Carruthers, and L.J. Lindberg, Materials Science Research, Vol. 14, pp 661-676, J.A. Pask, and A. Evans, Eds. Plenum Press, NY (1981)

3. K.N. Lee, R.A. Miller, and N.S. Jacobson, Ceramic Transactions, Vol. 38, pp 565-575, N.P. Bansal, Ed. The American Ceramic Society, Westerville, OH (1993)

4. J. Schienle, and J. Smyth, Final Report, ORNL/Sub/84-47992/1 (1987).

5. W.J. Lackey, D.P. Stinton, G.A. Cerny, L.L. Fehrenbacher, and A.C. Schaffhauser, ORNL/TM-8959 (1984).

6. W.J. Lackey, D.P. Stinton, G.A. Cerny, L.L. Fehrenbacher, and A.C. Schaffhauser, Adanced Ceramic Materials, Vol. 2, No. 1 (1987).

7. J.I. Federer, Adv. Ceram. Mater., **3** [1] 56 (1988).

8. I.A. Aksay, and J.A. Pask, J. Am. Ceram. Soc., 58 [11-12] 507 (1975).

9. K.N. Lee, N.S. Jacobson, and R.A. Miller, MRS Bulletin, Vol. 19, No. 10, pp 35-38, (1994)

10. R. Colmet, and R. Naslain, Wear, 80, pp 221-231 (1982)

11. C.S. Park, J.G. Kim, and J.S. Chun, J. Vac. Sci. Technol. A 1 (4) pp 1820-1824 (1983)

12. J. Oroshnik, J. Kraitchman, J. Electrochem. Soc., Vol. 155, No. 6, pp 649-652 (1968)

13. W. Hanni, H.E. Hintermann, D. Morel, and A. Simmen, Surface and Coatings Technology, Vol. 36 pp 463-470 (1988)

14. A.C. Adams, and C.D. Capio, J. Electrochem. Soc., Vol. 126, No. 6, pp 1042-1046 (1979)

15. K.E. Spear, Proceedings of the 7th International Conference on CVD, T.O. Sedgwick, and H. Lydtin, eds. Electrochemical Society, Pennington, NJ, pp 1-16 (1979)

16. T.M. Besmann, Proceedings of the First International Conference on Surface Modification Technology, pp 311-325, 17th TMS Annual Meeting, T.S. Sudarshan, and D.G. Bhat, eds., Phoenix, AZ January 25-28, (1988)

17. A.I. Kingon, and R.F. Davis, pp. 317-328, in Conference on Emergent Process Methods for High-Technology Ceramics, R.F. Davis, H. Palmour III, and R.L. Porter, eds., Raleigh, NC (1982)

18. L. Vandenbulcke, J. Electrochem. Soc. Vol. 128, No. 7, pp 1584-1587 (1981)

19. T.S. Moss, J.A. Hanigofsky, and W.J. Lackey, J. Mater. Res., Vol. 7, No. 3 pp 754-764 (1992).

20. F. Teyssandier, M. Ducarrior, and C. Bernard, Journal of the Less-Common Metals, 78 pp 269-274 (1981)

21. C. Bernard, Proceedings of the 8th International Conference on CVD, Gouvieux, France, The Electrochemical Society, Pennington, NJ, pp 3-16 (1981)

22. H.E. Rebenne, and V.K. Sarin, Proceedings of the 25th Automotive Technology Development Contract Coordinators Meeting, SAE, pp 199-206 (1987)

23. T.M. Besmann, ORNL/TM-5775, Oak Ridge National Laboratory, Oak Ridge, TN(1989).

24. G. Eriksson, Acta Chem. Scand. 25, No. 7, pp 2651-2658 (1971)

25. K.F. Jensen, Microelectronics Processing: Chemical Engineering Aspects, D.W. Hess and K.F. Jensen, eds., American Chemical Society, Washington, DC, p. 199 (1989)

26. D.R. Stull, and H. Prophet, JANAF Thermochemical Tables, Third Edition, Parts I and II, American Institute of Physics, U.S. Government Printing Office, Washington, DC (1986)

27. R. Mulpuri, and V.K. Sarin, 19th Annual Cocoa Beach Conference and Exposition on Engineering Ceramics, Cocoa Beach, FL, The American Ceramic Society, Westerville, OH, January 1995

28. R. Mulpuri, and V.K. Sarin, US Patent Application Filed, Serial Number 08/368,814, January 1995.

PLASMA DEPOSITION OF HIGH TEMPERATURE PROTECTIVE COATINGS

O.R. Monteiro[1], Z. Wang[1], K.-M. Yu[1], P.Y. Hou[1], I.G. Brown[1], B.H. Rabin[2] and G.F. Kessinger[2]

[1]Lawrence Berkeley National Laboratory, University of California, Berkeley, CA 94708
[2]Idaho National Engineering Laboratory, P.O. Box 1625, Idaho Falls, ID 83415-2218

ABSTRACT

Oxide ceramic films can be made using a vacuum arc based technique in which a metal plasma is formed in an oxygen background, with ion energy controlled by the application of a repetitive pulse bias to the substrate throughout the deposition. High ion energy early in the process produces atomic mixing at the film-substrate interface while lower but optimized ion energy later in the deposition can control the structure and morphology, and films that are adherent and dense can be formed in this way. We have investigated the formation of films of aluminum-silicon oxide on silicon carbide substrates by mixed aluminum and silicon plasmas produced from separate plasma sources. The Al to Si ratio was controlled by the plasma gun parameters and the guns were pulsed simultaneously so as to mix the plasma streams before deposition; a magnetic plasma homogenizer device was used to further blend the two plasmas. Films with Al:Si ratios from 2:1 to 8:1 were produced (Al:Si is 3:1 for mullite), and the oxygen content in the films was controlled by varying the oxygen partial pressure during deposition. We have also compared some of the characteristics of alumina films plasma deposited on iron aluminide substrates with films produced by e-beam evaporation of Al_2O_3 using oxygen ion beam assisted deposition onto unheated or heated substrates. Here we outline the film synthesis techniques and describe the characterization results obtained to-date.

INTRODUCTION

The formation of thin films by plasma deposition is a versatile technique with a wide range of different embodiments. The version that we've developed and used has the important feature that the ion energy can be controlled widely. Highly adherent, dense films of metals, alloys (including non-equilibrium alloys) and other conducting materials, and their oxides and nitrides, can be formed. In the early stages of the process the ion energy is held in the keV range so as to produce atomic mixing at the film-substrate interface, and in the latter stages of deposition the energy is reduced so as to optimize the film structure and morphology.

In this method, which we call Mepiiid (*Me*tal *p*lasma *i*mmersion *i*on *i*mplantation and *d*eposition), the object to be implanted is immersed in a plasma of the desired species and repetitively pulse-biased to a negative voltage[1-6]. A high voltage sheath rapidly forms at the substrate-plasma boundary, and plasma ions are accelerated through the sheath and into the substrate, thereby accomplishing implantation into the substrate of plasma ions at an energy determined by the bias voltage. Because of the surface retention of condensed metal plasma, the plasma immersion process in a metal plasma is quite different from in a gaseous plasma. Ions that are accelerated from the plasma into the substrate during the high voltage bias pulse suffer collisions with previously-deposited neutral metal atoms on the substrate surface and thus also produce recoil implantation. By varying the proportions of the direct and recoil implantation parts of the

cycle (ie, the duty cycle of the pulse biasing) one can tailor the shape of the profile, and the range can be tailored by the amplitude of the applied pulse voltage. The whole operation can be time-varied throughout the processing duration, starting for example with a high energy phase so as to create a deep buried layer of the implanted species and slowly changing to a low energy phase whereby a surface film is built up by plasma deposition. By controlling the plasma ion energy we acquire control over two very important features to the deposition process: the interface width can be tailored, and the film morphology and structure can be controlled. In this way one can synthesize a surface metallic film of precisely controllable thickness having a well-determined and controllable atomically mixed interface with the substrate, and the parameters of the film and the interface can be tailored over a wide range. For purely metallic films, the process is carried out at a vacuum in the 10^{-6} Torr range; oxides and nitrides can be formed by doing the deposition at the appropriate background pressure of oxygen or nitrogen, typically a few tens of microns. The technique has been developed by us and others, and put to a range of laboratory applications.

In prior work we have shown that highly adherent films can be formed in this way. We have produced near-stoichiometric alumina films of thickness ~0.5 μ on substrates of FeAl (containing ~0.1% Zr); the films were amorphous prior to heat treatment and showed an α-alumina phase after heat treating at 1000°C for up to 16 hours[7,8]. The film substrate adhesion was typically greater than ~70 MPa prior to heating, and the adhesion was maintained after repetitive cycling in temperature between ambient and 1000°C.

We report here on the extension of this work in two directions. We have explored the plasma synthesis of aluminum-silicon oxide films on silicon carbide substrates by mixing together separately produced plasmas of aluminum and silicon. The Al to Si ratio was controlled by the plasma gun parameters and the plasmas blended together in a magnetic multipole plasma homogenizer device. Deposition was done onto appropriately positioned SiC substrates. Separately, we have compared the characteristics of alumina films plasma deposited on iron aluminide substrates with films produced by e-beam evaporation of Al_2O_3 using oxygen ion beam assisted deposition onto unheated or heated substrates. We outline here the film synthesis techniques and describe the results obtained to-date.

PLASMA PROCESSING

The vacuum arc is a high current discharge between two electrodes in vacuum in which metal plasma is produced in abundance[9-12]. We have made a number of different embodiments of vacuum arc plasma guns. For the work described here we used a small, repetitively pulsed version operated at a pulse length of 5 ms and repetition rate about 1 Hz, and arc current in the range 100 – 300 A. Along with the metal plasma that is generated, a flux of macroscopic droplets of size in the broad range 0.1 - 10 microns is also produced[9-14]. In general it is desirable to remove the solid particulate contamination and this can be done using a curved 'magnetic duct' which stops line-of-sight transmission of macroparticles while allowing the transmission of plasma[15,16]. The overall plasma deposition system thus consists of the repetitively pulsed plasma gun in conjunction with the 90° bent magnetic filter. Plasma exits the filter and deposits on the substrate.

Metal oxides can be formed by carrying out the deposition not in a high vacuum environment but in a somewhat higher pressure ambient of oxygen gas; we have found empirically that a pressure in the range 1 - 100 mTorr is suitable for most purposes. In the present work the oxygen background pressure was 5 to 25 mTorr. The oxygen is both entrained in the plasma stream, ionized, and deposited in the plasma state, as well as reacting at the freshly-deposited metallic surface to form aluminum oxide or silicon dioxide. In either case, for the optimal oxygen pressure a near-stoichiometric film of the metal oxide is formed.

Ion energy of the depositing plasma flux is controlled by repetitively pulse biasing the substrate. Typically the pulse duration might be ~10 μs and the duty cycle ~10 - 50%. Pulsing of the bias voltage is necessary (for all but the lowest bias voltages) because a high-voltage dc bias would cause an electrical discharge between the substrate and the vessel or the plasma gun; the plasma would be grossly perturbed (because the plasma sheath would expand from the substrate to large distances). The solution is to switch off the bias before a discharge can occur (to limit the sheath expansion to modest distances), let the plasma recover, and then repeat the process; ie, to do the biasing in a repetitively pulsed mode. For the early stages of the deposition process the pulse bias is held at a relatively high voltage of 2.2 kV. The mean aluminum ion energy is then 3.75 keV, because the mean ion charge state of the aluminum plasma is 1.7 and $E_i = QV$; for silicon the mean charge state is 1.4 and the mean ion energy 3.1 keV; (the charge state spectra of vacuum arc produced plasmas have been discussed in detail in refs. 17,18). At this energy ions are implanted into the substrate to a depth of up to ~100 Å. The film thus grows on the SiC substrate from a highly mixed interface. When a film thickness of just a few tens of angstroms has accumulated, the pulse bias voltage is reduced, since intermixing with the substrate is no longer a factor and the higher ion energy would sputter away the already-deposited film. Moreover, it is known from a large body of work on ion assisted deposition that a modest ion energy can be highly advantageous for controlling such characteristics as the density, morphology and structure of the film. For the bulk of the plasma deposition process the pulse amplitude is kept at 200 volts.

For synthesis of the mixed aluminum-silicon oxide films we firstly tried a plasma gun cathode that was formed of mixed Al-Si in 3:1 atomic ratio – mullite has composition $3Al_2O_3.2SiO_2$ for an Al:Si atomic ratio of 3:1 – but we found that the deposited film composition ratio did not reflect the cathode composition ratio closely enough. Thus we went to an alternative approach making use of an additional plasma gun/filter for forming a Si plasma that was added to the original Al:Si plasma stream. The two streams are then fed through a special 'plasma homogeneizer', which further mixes and spreads out the plasma stream. The plasma homogenizer is a magnetic multipole plasma confinement geometry, well known in the plasma community and made here using a number of high-field-strength rare-earth permanent magnets. The utility of this kind of arrangement, in particular the novel use of the homogenizer as a tool for blending the two vacuum arc plasmas, has been explored in prior work in our laboratory[19,20]. The precise Al:Si atomic mix can then be tuned via the plasma guns (pulse width or arc current). Films with Al:Si ratios varying from 1:1 to 8:1 were formed. A simplified schematic of the overall system is shown in Figure 1.

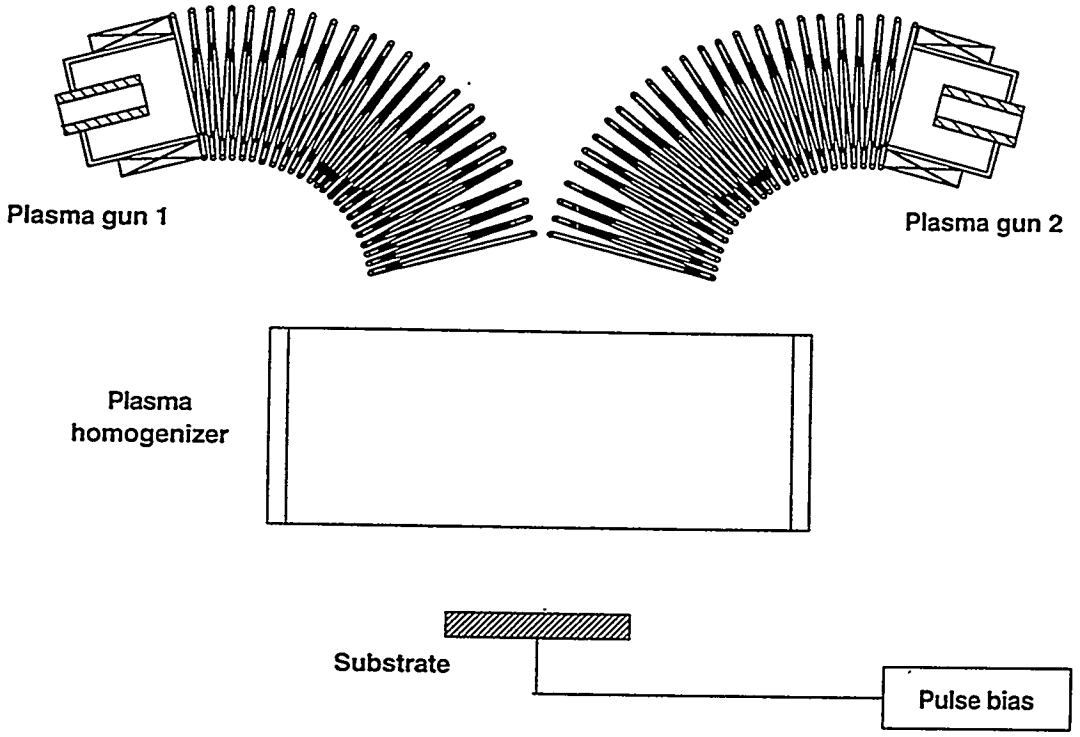

Fig. 1. Schematic of the overall dual-gun deposition system

EXPERIMENTAL RESULTS

Aluminum-Silicon Oxides (Mullite)

Two types of SiC substrate material were used; one was sintered at LBNL from commercially available SiC powders, and the other was a commercial SiC (Hexalloy 5) from Carborundum Industries. The material produced at LBNL contained 94.4% SiC, 3% Al, 2% C, and 0.6% B. The surface was ground and polished to a mirror finish prior to the deposition. Scanning electron microscopy of the polished surface of an uncoated piece of LBNL silicon carbide showed the presence of a second phase, appearing as dark grains that are Al-rich particles.

Control of the stoichiometry of the silicon-aluminum oxide films was achieved by varying the duration of the plasma pulses and the oxygen partial pressure during deposition. The deposition rate of each individual source was determined for all oxygen partial pressures used by measuring the thickness of the deposited films after one thousand pulses of 5 ms duration each. These individual deposition rates were then used to deposit films with desired Al:Si ratios.

An advantage of the Mepiiid process is the high degree of atomic mixing achieved; thus here the duration of the pulses used was always below the time required for the formation of monolayers of silica or alumina, and both sources were triggered simultaneously so as to prevent stratification of alumina or silica. A previous attempt to synthesize mullite coatings by depositing alternate layers of silica and alumina by CVD and subsequent annealing failed due to brittleness resulting from the transformation of silica into crystoballite that takes place during the high temperature annealing required to homogenize the multilayer film[21]. Here we wanted to ensure that complete mixing happened during the deposition.

Table 1 shows the composition of several aluminum-silicon oxides films deposited on SiC under various experimental conditions. The content of each element in the films was determined by Rutherford Backscattering Spectroscopy (RBS) and normalized to the Si content. The accuracy of these measurements is ±15%. Elemental composition of mullite is also included in the table for comparison.

Table 1. Composition of as-deposited films.

Deposition	Al-Si pulse (ms)	Si pulse (ms)	Pressure (mTorr)	Al content	Si content	O content	Thickness (nm)
#1	5	5	25	4.4	1	10.4	240
#2	5	2.5	25	6.7	1	16	230
#3	5	10	25	1.2	1	5.3	240
#4	5	0	25	8	1	19.5	220
#5	5	0	5	7.4	1	13	240
#6	5	5	25	4.2	1	10.4	1250
Mullite				3	1	6.5	

X-ray diffraction indicates that the deposited films were amorphous. No evidence of crystalline structure or phase separation was observed. A feature in the films produced was the high oxygen content when deposition was carried out at 25 mTorr. An analysis of the compositions shown in Table 1 indicates that films produced at this pressure consist of mixtures of Al_2O_{3+x} and SiO_{2+y} with a good match being achieved for $x = 2$ and $y = 0$. Al_2O_5 is not a stable oxide for our deposition conditions, and therefore this composition must be a consequence of oxygen ion bombardment. Such high oxygen content has been found previously in pure alumina films produced by MePiiid at 26 mT [7]. At lower pressures, oxygen implantation appears to decrease in importance and the films are basically mixtures of Al_2O_3 and SiO_2.

Annealing of the films at 1100°C in air for 2 hours resulted primarily in the formation of crystalline mullite. The alumina-silica binary phase diagram indicates that the only stable phases in the silica-alumina system at the pressures used in this investigation are silica, alumina and mullite. To achieve the mullite stoichiometry, excess oxygen present in the as-deposited films had to be lost to the environment or react with the SiC substrate to form silicon oxide and/or carbon dioxide. X-ray diffraction indicates mullite as

the main crystalline phase after annealing (Fig. 2). The low intensity of the diffraction peaks is mostly due to the small film thickness. Another silicon-aluminum oxide known as sillimanite ($Al_6Si_3O_{15}$) can also be fitted to the peaks in the diffractogram but was discarded because the ratio of intensities of the diffraction peaks was closer to that expected from mullite. Little difference was observed in the diffraction patterns of the samples #1 through #5, indicating that after annealing at 1100°C, in all cases the main crystalline phase formed was mullite. In the films with very low Al:Si ratio we were expecting that silicon dioxide would be present as well, and in the films with very high Al:Si ratio, peaks from crystalline alumina were expected. However, neither of these phases, silica or alumina, could be identified from the diffraction patterns of samples #1 through #5. Further sample preparation and characterization is in progress.

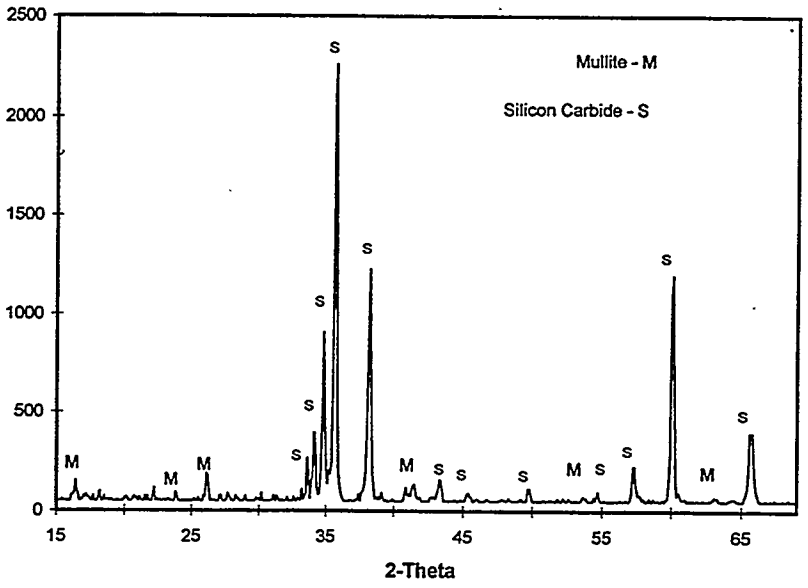

Fig. 2. X-ray diffraction pattern of coated SiC (#1) annealed at 1100°C for 2h in air.

Table 2. Adhesion of as-deposited and annealed films:

Deposition	Adhesion as-deposited (MPa)	Adhesion annealed (MPa)	Al content (pre-anneal)	Si content (pre-anneal)	O content (pre-anneal)	Thickness (nm)
#1	9	70	4.4	1	10.4	240
#2	38	57	6.7	1	16	230
#3	31	63	1.2	1	5.3	240
#4	31	57	8	1	19.5	220
#5	9	65	7.4	1	13	240

Adhesion test results for the as-deposited and the annealed films are shown in Table 2. The instrumental limit of our pull-tester before epoxy failure occurs is ~70 MPa, and all of the post-annealing samples show an adhesion strength that is within experimental uncertainty of this instrumental limit.

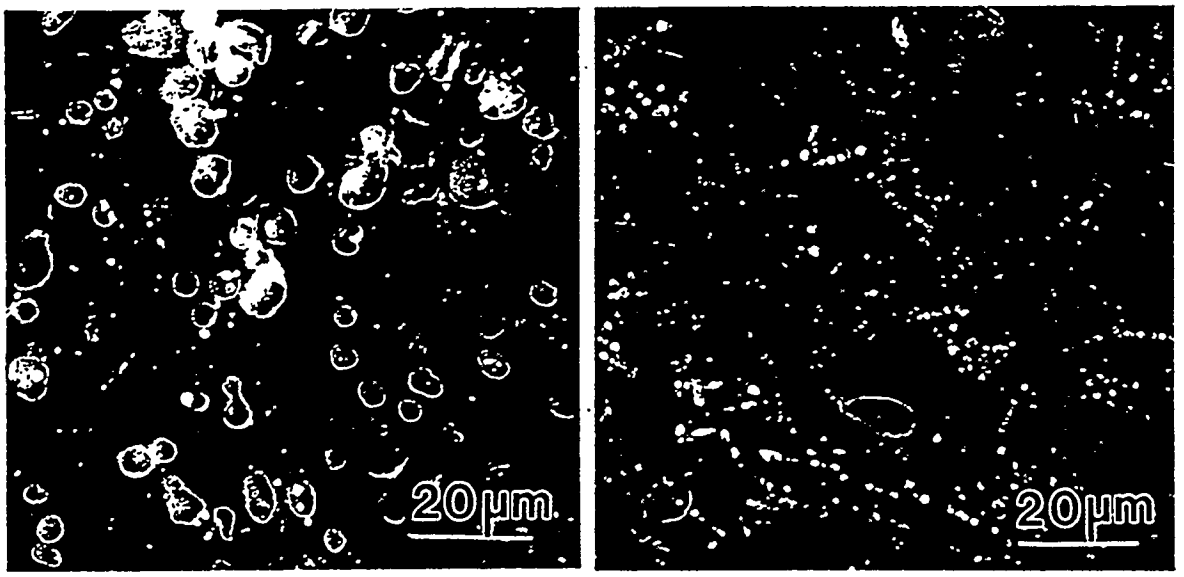

Fig. 3 SEM of a SiC sample with an aluminum-silicon oxide coating after being tested for adhesion. (a) area which had the film removed; (b) area from where the film was still present.

When the aluminum content of the coating was too high, e.g. samples #2, #4 and #5, both the as-deposited and the annealed films had a high concentration of microstructural features that looked like micro-bubbles. The mechanism of formation of these bubbles is not clear to us yet, but their concentration seems to be directly related to the deviation of the Al content from the ideal mullite stoichiometric ratio (i.e. the higher the Al content, the higher the density of voids). These bubbles are clearly seen in the micrographs shown in Fig. 3. Figs 3(a) and 3(b) are SEM images from sample #4 after annealing and after the adhesion test; Fig 3(a) is from an area from which the film has been removed by the adhesion pull-test measurement, and Fig 3(b) is from an area which still has the film intact. The delamination left the voids exposed, suggesting that these voids were either at the SiC/oxide interface or in the SiC but near to the interface. Upon annealing, very few of these bubbles appear to have broken through the coating, but in the regions where the film delaminates due to the pull-test, these voids have been exposed. Subsurface bubbles (voids) have been observed to form in the silicon carbide used here when subjected to high temperature oxidation.

It is clear from the results presented here that annealing of the deposited aluminum-silicon oxides helps greatly to improve the adhesion of the film. Stoichiometry seems to play a role in the adhesion of the as-deposited (pre-annealing) film. An extensive analysis of microstructure of the coatings is under way, and the role of the Al-Si stoichiomety and of oxygen content on the as-deposited adhesion strength should become clear.

Aluminum Oxides

In this section we describe the initial results of the characterization of the properties of aluminum oxide films deposited on iron aluminides (Zr-containing) by two different ion beam assisted techniques.

The first technique, Mepiiid, is as described above except that instead of two plasma sources only an aluminum source was used, in oxygen. All depositions were done at room temperature. The as-deposited alumina films were amorphous, and with an oxygen content that depended on the oxygen partial pressure. At a pressure of 12 mTorr the film composition was $Al_2O_{3.3}$, whereas at 25 mTorr the composition was Al_2O_5. Such a high oxidation state of aluminum has been observed previously in MePiiid produced films[7]. The Al_2O_5 produced here is believed to be a direct result of the simultaneous implantation that our plasma method provides. Annealing of the amorphous Al_2O_5 and $Al_2O_{3.3}$ films at 1100°C in air for two hours led to their crystallization into α-Al_2O_3. Adhesion of these films has been reported previously to exceed 70 MPa in the as-deposited amorphous condition as well as after annealing[7].

The second set of aluminum oxide films was prepared using ion-beam assisted (IBAD) deposition according to the following procedure. The substrate was initially ion-milled with 1 kV Ar^+ ions at an ion current of 0.15 mA. Then Al_2O_3 was deposited at a rate of 0.5 nm/s to a total thickness of 500 nm. During the initial 10 - 15 nm, a 1 kV oxygen ion beam (0.25 mA) simultaneously bombard the substrate, and for the remainder of the deposition the energy of the incident oxygen ions was reduced to 0.4 kV. Depositions were done at two different temperatures, 825 K and 605 K. Cooling of the substrate to room temperature after deposition was done in vacuum.

The films have been characterized by X-ray diffraction, and the results are presented in Figure 4. Post-deposition heat treatments are presently under way. The e-beam + IBAD films produced at low temperature were predominantly amorphous, while the film deposited at 825K contain microcrystalline aluminum oxides, as evidenced in the X-ray diffractogram. The specific alumina phase present could not be uniquely determined and a mixture of several phases is likely. In addition some amorphous materials may also be present since the deposition temperature was still much lower than the recrystallization temperature, and the diffraction peaks are somewhat diffuse. The film deposited at 825K had a grainy appearance whereas the films produced at 600K looked more homogeneous, similar to the ones deposited by Mepiiid.

The ion energies used in the IBAD and the Mepiiid process are similar. In the early stages of the IBAD process, oxygen ions are accelerated through 1kV, and for the remainder of the deposition the accelerating voltage is reduced to 0.4 kV. In Mepiiid, aluminum ions are responsible for the plasma formation and subsequent ionization of the oxygen. The accelerating voltages used for Mepiiid are 2kV during the first tens of nanometer and 0.2kV for the remainder of the deposition. Characterization for their adhesion and corrosion resistance properties and comparison of films prepared in the two different but related ways described above is continuing, and we will report on this work as the results become available.

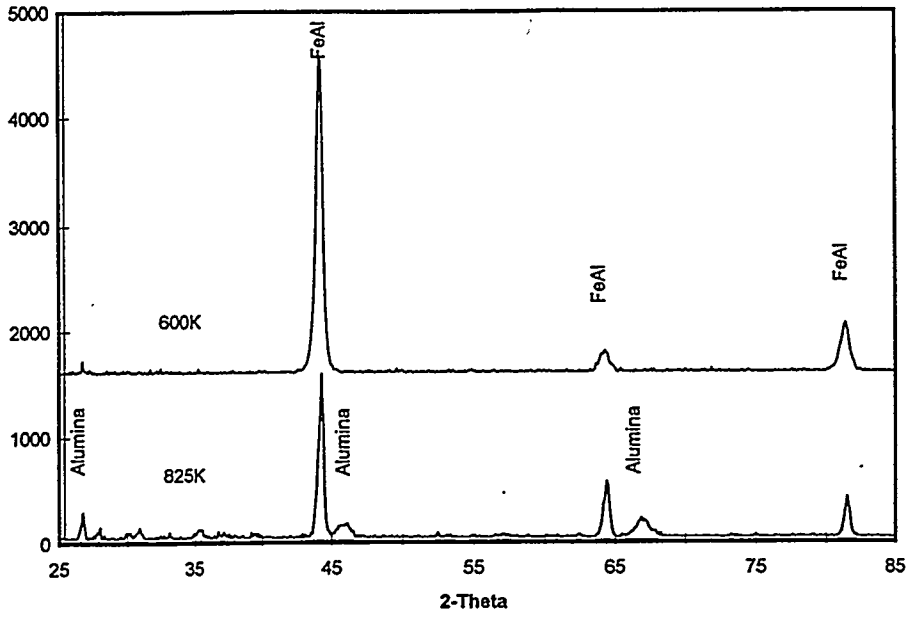

Fig. 4 Diffraction pattern of the as-deposited alumina films produced by e-beam evaporation + ion-beam assisted deposition. The deposition temperatures are indicated.

CONCLUSION

A novel technique for the plasma synthesis of high temperature protective coatings for metallic and ceramic structural materials (*Me*tal *p*lasma *i*mmersion *i*on *i*mplantation and *d*epostion, *Mepiiid*) has been applied to deposit aluminum-silicon oxides on silicon carbide, and aluminum oxide on iron aluminides. Post-annealing adhesion of the aluminum-silicon oxide films was good. When the Al:Si ratio increases, adhesion between the oxide and the SiC is weakened because of the presence of voids at or immediately below the interface. Our plasma method allows convenient and simple control of the "quasi-mullite" film stoichiometry.

Aluminum oxides on iron aluminides were also produced by Mepiiid and by e-beam evaporation + IBAD. Depositions below 300°C resulted in films which are amorphous by both techniques. Deposition at higher temperatures with e-beam + IBAD led to the formation of a mixture of micro-crystalline aluminum oxides. Annealing at 1000°C for 16h in air of the Mepiiid film resulted in a coating that is predominantly α-Al_2O_3. Further work is underway to continue the comparison between the films produced by these two techniques.

ACKNOWLEDGMENTS

We are indebted to Bob MacGill and Mike Dickinson for their support of the LBNL experimental equipment. This work was supported by the U.S. DOE, Office of Advanced Research, Fossil Energy, under Contract Number DE-AC03-76SF00098.

REFERENCES

1. I.G. Brown. X. Godechot and K.M. Yu, Appl. Phys. Lett. 58, 1392 (1991).
2. I.G. Brown, A. Anders, S. Anders, M.R. Dickinson, I.C. Ivanov, M.A. MacGill, X. Yao and K.M. Yu, Nucl. Instrum. Meth. Phys. Res. B80/81, 1281 (1993).
3. Ian Brown, in *Plasma Synthesis and Processing of Materials*, edited by K. Upadhya (pub. TMS, Warrendale, PA, 1993).
4. A. Anders, S. Anders, I.G. Brown and I.C. Ivanov, Mat. Res. Soc. Symp. Proc. 316, 833 (1994).
5. A. Anders, S. Anders, I.G. Brown, M.R. Dickinson and R.A. MacGill, J. Vac. Sci. Tech. B12, 815 (1994).
6. See the proceedings of the First International Workshop on Plasma-Based Ion Implantation, J. Vac. Sci. Tech. B12, 815-998 (1994).
7. Ian Brown and Zhi Wang, "Plasma Synthesis of Alumina Films on Metal and Ceramic Substrates", 9th Annual Conference on Fossil Energy Materials, Oak Ridge, TN, May 16-18, 1995, Proceedings of conference (U.S. Dept. of Energy, Conf-9505204, ORNL/FMP-95/1), p. 239.
8. P.Y. Hou, K.B. Alexander, Z. Wang and I.G. Brown, "The Effect of Plasma Synthesized Alumina Coatings on the Oxidation Behavior of Iron Aluminides", TMS Annual Meeting, Symposium on High Temperature Coatings, Anaheim, CA, Feb 4 - 8, 1996.
9. J.M. Lafferty (ed.), *Vacuum Arcs - Theory and Application*, Wiley, New York, 1980.
10. R.L. Boxman, P. Martin and D. Sanders (eds), *Vacuum Arc Science and Technology*, Noyes, New York, 1995.
11. For a most impressive and comprehensive bibliography of the vacuum arc literature see H.C. Miller, *A Bibliography and Author Index for Electrical Discharges in Vacuum (1897 - 1986)*, pub. by the General Electric Co., document No. GEPP-TIS-366e (UC-13), March 1988; also published in part in IEEE Trans. Elec. Insul. 25(5),765 (1990) and 26(5), 949 (1991).
12. See the Special Issues on Vacuum Discharge Plasmas in IEEE Trans. Plasma Sci. These issues contain selected papers from the biennial International Symposium on Discharges and Electrical Insulation in Vacuum, (usually in the October issues in odd-numbered years).
13. D.T. Tuma, C.L. Chen and D.K. Davies, J. Appl. Phys. 49, 3821 (1978).
14. J.E. Daalder, Physica 104C, 91 (1981).
15. I.I. Aksenov, A.N. Belokhvostikov, V.G. Padalka, N.S. Repalov and V.M. Khoroshikh, Plasma Physics and Controlled Fusion 28, 761 (1986).
16. A. Anders, S. Anders and I.G. Brown, Plasma Sources Sci. & Technol. 4, 1 (1995).
17. I.G. Brown and X. Godechot, IEEE Trans. Plasma Sci. PS-19, 713 (1991).
18. I.G. Brown, Rev. Sci. Instrum. 10, 3061 (1994).
19. S. Anders, S. Raoux, K. Krishnan, R.A. MacGill and I.G. Brown, "Application of a Magnetic Multicusp to a Cathodic Arc Deposition System", J. Appl. Phys. (1996), to be published.
20. S. Anders, R.A. MacGill, S. Raoux and I.G. Brown, "Modification of Cathodic Arc Deposition Profiles by Magnetic Multicusps", to be presented at the XVIIth Int. Symp. on Discharges and Electrical Insulation in Vacuum, Berkeley, CA, July 21-26, 1996.
21. D. Doppalapudi, R. Mulpuri, S.N. Basu and V.K. Sarin, "Phase Transformations in Multilayered CVD Mullite Coatings", Mat. Res. Soc. Symp. Proc. 363, 95 (1995).